

# UC Santa Barbara

## UC Santa Barbara Electronic Theses and Dissertations

### Title

Insights into the Sea-Level History of the South Shetland Islands from Ground Penetrating Radar on Livingston Island, Antarctica

### Permalink

<https://escholarship.org/uc/item/2df4080c>

### Author

Gernant, Cameron Michael

### Publication Date

2021

Peer reviewed|Thesis/dissertation



UNIVERSITY OF CALIFORNIA

Santa Barbara

Insights into the Sea-Level History of the South Shetland Islands from Ground Penetrating  
Radar on Livingston Island, Antarctica

A thesis submitted in partial satisfaction of the  
requirements for the degree Master of Science  
in Earth Science

by

Cameron Michael Gernant

Committee in charge:

Professor Alexander R. Simms, Chair

Professor David Lea

Professor Vamsi Ganti

September 2021

The thesis of Cameron Gernant is approved.

---

David Lea

---

Vamsi Ganti

---

Alexander R. Simms, Committee Chair

September 2021

## ACKNOWLEDGMENTS

Throughout my contributions to Antarctic sedimentary geology, I have received a great deal of both professional and personal support.

First and foremost, I must thank my master's advisor Dr. Alexander Simms. Alex has sat through countless conversations about my research and given me equally as much feedback professionally as he has in my personal life. Without his guidance, patience, understanding, and subject expertise I would not have completed this thesis.

I am grateful to have been able to work internationally for my MS project, which was made possible by funding provided by the National Science Foundation. I want to extend my appreciation to The United States Antarctic Program and the crew of the RSV Lawrence M. Gould. The United States Antarctic Program also provided our research team with field guides Cara Ferrier and Robin Carroccia. Their camp maintenance, safety, meal prep and company made fieldwork enjoyable in otherwise austere conditions.

I want to thank Dr. Vamsi Ganti and Dr. David Lea for serving on my committee and for their feedback on where to steer my project and valuable insight into concepts I had not previously considered. Graduate school was made much more navigable by my fellow graduate students in Earth Science through constant discussion, scientific and otherwise. My lab mates Brittany Theilen and Julie Zurbuchen provided the bulk of this interaction through Julie's expertise in my specific field of study and Brittany through her comradery in the field and discussions about our study area.

Although not compiled in this work, I want to thank our fellow scientists Dr. Regina DeWitt and PhD student Christopher Garcia at East Carolina University for hosting me and teaching me about sample preparation for optically stimulated luminescence age dating. I felt very welcome in their lab and spent a summer preparing many OSL samples from Joinville and Livingston Islands.

My most sincere appreciation is extended to Marianne Okal from UNAVCO for finding missing GPS data on our field equipment and processing it in a creative way using data from regional GPS base stations and being thorough and prompt in all responses. I would also like to thank other members at UNAVCO Thomas Neilen and Spencer Niebuhr for assisting with GPS processing.

After my advisor, Dr. Simms, the first person I spoke to at UCSB was the Earth Science Graduate Program Coordinator, Yann Ricard. Yann has found numerous creative ways to get the job done with myself and all the other graduate students' best interests remaining his top priority. For this, and for all the conversations in between, I want to thank Yann for making me feel welcome when that was in doubt.

I would like to thank the UCSB Veteran Resource Center, specifically Colby Dillard, for making me feel at home at UCSB and for his hard work in bringing the center and the UCSB military community into focus on campus. His unwavering dedication to his mission and advocacy for our community has assisted me and so many other veterans in our education, and in life.

Lastly, I would like to thank my family and friends for their, at times blind, belief in my abilities when I lacked the same confidence. Your support pushed me to the finish line.

## ABSTRACT

### Insights into the Sea-Level History of the South Shetland Islands from Ground Penetrating Radar on Livingston Island, Antarctica

by

Cameron Michael Gernant

Raised beach ridges in polar environments are recorders of relative sea-level (RSL) change. The South Shetland Islands (SSI) contain large areas of ice-free raised beaches used to resolve paleo-sea-level change. The largest of these ice-free areas is Byers Peninsula (60 km<sup>2</sup>) on Livingston Island, SSI. This peninsula and other ice-free coasts within the SSI contain series of raised beach ridges correlated by age and elevation. The internal architecture of these beach ridges is critical to understanding paleo-RSL. The non-destructive method of ground penetrating radar (GPR) was used to investigate the internal architecture of the South Beaches of Livingston Island where a flight of nine beach ridges (five of which were the focus of in this study) have been glacio-isostatically raised since the last glacial maximum (LGM). Recalibrated radiocarbon ages collected from these and other beach ridges in previous studies are used to relate beach morphology and stratigraphy to the glacial history of the region. Over 10 km of 200 MHz GPR transects and synchronous GPS were collected over a two-week period in the spring of 2019. Sediment pits <1 m in depth were dug to search for dateable material and described for ground truthing of GPR reflections. Six key

radar facies and three radar surfaces were identified: a seaward dipping progradational facies, a landward dipping overwash facies, a flat and concave down aggradational facies, a discontinuous hyperbola rich cobble facies, a flat lying lagoon facies, and a channelized fluvial facies. Erosional and toplapping surfaces were identified in addition to the top of the bedrock. Within this flight of raised beach ridges evidence was found of transgressive depositional patterns marked by progradational seaward dipping facies deposited during periods of RSL fall followed by erosion and overlying deposition of landward dipping overwash and aggrading beds. This succession is routinely located over a notch in the bedrock interpreted to represent a wave-cut feature. An apparent correlation between the ages of beach ridges and wave-cut notches with known neoglacial advances at ~5.5 ka, ~3-1 ka, and ~0.4 ka suggests that the influence of glacial-isostatic adjustment (GIA) on RSL is responsible for the origin of the beach ridges and the underlying wave-cut scarps. This GIA hypothesis further supports recent assertions of a much more dynamic RSL history for Antarctic coastlines, which may “contaminate” the LGM RSL signal across Antarctica.

## TABLE OF CONTENTS

- 1. Introduction**
- 2. Background**
  - 2.1. Geologic Setting**
  - 2.2. Glacial History**
  - 2.3. Glacio-Isostatic Adjustment (GIA) and Sea Level**
  - 2.4. Raised Beaches**
  - 2.5. Livingston Island Field Site**
    - 2.5.1. Location and Beach Characteristics**
    - 2.5.2. Climatic Setting**
- 3. Methods**
  - 3.1. GPS**
  - 3.2. Ground Penetrating Radar**
  - 3.3. Tide Gauge**
  - 3.4. Radiocarbon Age Corrections**
  - 3.5. Bedrock Erosion**
  - 3.6. Sediment Trenching**
- 4. Results**
  - 4.1. Elevations**
  - 4.2. Radar Facies**
  - 4.3. Radar Surfaces**
  - 4.4. Beach Ridge Architecture**
  - 4.5. Radiocarbon Ages**
  - 4.6. Bedrock Erosion Rates**
  - 4.7. Sediment Trenches**
- 5. Discussion**
  - 5.1. Interpretation of Ground Penetrating Radar**
    - 5.1.1. Radar Facies**
    - 5.1.2. Radar Surfaces**
  - 5.2. Controls on Beach Ridge Architecture**
    - 5.2.1. Tectonics (Earthquakes)**
    - 5.2.2. Tsunami**
    - 5.2.3. Wave Energy**
    - 5.2.4. Glacial-Isostatic Adjustment**
    - 5.2.5. Timing of Scarps: Relationship to Known Ice Advances**
    - 5.2.6. Marine Platform Erosion Rates**
    - 5.2.7. Relating Fluctuations in RSL with Granulometry**
    - 5.2.8. Other Geomorphic Evidence Supporting the Model**
  - 5.3. Implications for the RSL of the SSI**
- 6. Conclusion**
- References**
- Appendix A. Supplementary Files**

## LIST OF FIGURES

- Figure 1: Hemispheric, Regional, Island, and Peninsula Map Set**
- Figure 2: Byers Peninsula Map**
- Figure 3: Tectonic Regime**
- Figure 4: Isobar Map of the Highest Beaches Across South Shetland Islands**
- Figure 5: Beaches Highlighted**
- Figure 6: Overview Photo of the South Beaches Field Site with Beach Locations  
Approximated**
- Figure 7: Pictures of the Field Site, Viewing Normal and Parallel to Beach 4**
- Figure 8: Pictures of the Modern Beach, and a Lagoon Landward of the Modern Beach**
- Figure 9: Locations of GPR Transects**
- Figure 10: Pictures of a Stream, Beach 2, and a Gully Dissecting the Seaward Edge of  
the 28-50 m Marine Platform**
- Figure 11: Bedrock Scarp Erosion Estimation Schematic**
- Figure 12: Locations of OSL Sediment Pits and Nearest Shore-Normal GPR Line**
- Figure 13: GPS Transects Along Strike of Beach Ridges on the South Beaches**
- Figure 14: Picture of Tidal Inlet Connection to Lagoon and Outcropping Bedrock**
- Figure 15: GPR Line 23, Westernmost Line Presented**
- Figure 16: GPR Line 21**
- Figure 17: GPR Line 21 Beach Ridge 2**
- Figure 18: GPR Line 19**
- Figure 19: GPR Line 17**
- Figure 20: GPR Line 25**
- Figure 21: GPR Line 25, Beach Ridges 4 & 5**
- Figure 22: GPR Line 14**
- Figure 23: GPR Line 12**
- Figure 24: GPR Line 34**
- Figure 25: GPR Line 34 Beach Ridge 9, Easternmost Line Presented**
- Figure 26: GPR Line 36**
- Figure 27: GPR Line 40, Shore Normal Line**
- Figure 28: Sediment Textures on South Beaches**
- Figure 29: Picture of Rotch Dome Proglacial Environment**
- Figure 30: Byers Peninsula RSL Curve**
- Figure 31: Model of Stranded Beach Ridge Formation**

## LIST OF TABLES

- Table 1: Livingston Island Beach Elevations**
- Table 2: Compilation of Radiocarbon Ages from Raised Beaches on Byers Peninsula**
- Table 3: Compilation of Radiocarbon Ages from Raised Beaches from Other Locations**
- Table 4: Average Recalibrated Radiocarbon Ages Assigned to South Beaches**
- Table 5: Beach Progradation Rates**
- Table 6: Livingston Island Estimated Beach Ridge Ages**
- Table 7A: Radar Facies**
- Table 7B: Radar Surfaces**
- Table 8: Livingston Island Estimated Platform Erosion Rates**
- Table 9: Livingston Island Beach-Surface Grain Size Data**



## 1. Introduction

The Antarctic Peninsula (AP) (Fig. 1) contains enough meltwater equivalent ice to raise global sea-levels by 2.4 m (Pritchard and Vaughan, 2007). The AP is also one of the fastest warming regions in the world, having seen a temperature rise of 3.4°C per century compared to continental Antarctica warming of 0.49°C per century through the 20<sup>th</sup> century (Vaughan et al., 2003). Understanding how ice along the AP will contribute to future sea-level rise is important for coastal hazard mitigation (IPCC, 2019). A better understanding of how this region's ice volume will behave in the future relies on understanding how it responded to past warming trends. Documenting its past behavior requires not only an understanding of the ice sheets past extent, but its volume too. Determining past ice volume is more difficult than determining ice extent, which is recorded in geomorphic features left on the landscape such as moraines, drumlins, and rock striations (Kelsey, 2015). One method of determining past volume changes is comparing records of past sea-level changes with glacial-isostatic adjustment (GIA) models. Geographically widespread and numerous relative sea-level (RSL) curves are essential for input into these GIA models (Bentley et al., 2005b), but relatively few RSL records exist across Antarctica.

Raised beach ridge elevations provide critical data for the reconstruction of relative sea-level curves across Antarctica (Hall 2010; Bentley et al., 2005). Not only do they preserve a record of past sea-level elevations, but also environmental conditions. This record of past environmental conditions is often recorded in the stratigraphic architecture of the beach ridges. On mixed sand-gravel beaches ground penetrating radar (GPR) provides an excellent

method for documenting that stratigraphic architecture (Lindhorst and Schutter, 2014; Nielsen et al., 2017).

The purpose of this study is to characterize the stratigraphic architecture of the South Beaches on Livingston Island of the South Shetland Islands (SSI) (Fig. 2). I use radar facies and surfaces in GPR transects to investigate past changes in sea-levels and other environmental conditions. My central hypothesis is that the South Shetland Islands experienced minor transgressions during the overall relative sea-level fall across the region. Previous studies have hypothesized such minor transgressions (John and Sugden, 1971; Curl, 1980; Bentley et al., 2005b; Hall, 2010), but evidence for those minor transgressions is currently lacking (Bentley et al., 2005b; Hall, 2009; Watcham et al., 2011). Such documentation may be observed within the subsurface stratigraphic architecture of the raised beaches of the South Shetland Islands.

## **2. Background**

### **2.1. Geologic Setting**

The South Shetland Island chain is a roughly 500 km long island arc situated in maritime sub-Antarctica. Together the two largest Islands, Livingston Island and King George Island (KGI), are spread over an area 230 km long but only 35 km wide (Fig. 1) (Adie, 1964; Smellie, 1984). They separate the Bransfield Basin to the south from the Drake Passage to the north (Gracia et al., 1997). The islands are surrounded by a shallow submarine platform extending 40 to 60 km north from the islands (Fretwell et al., 2010). To the south the

continental shelf is narrower with widths less than 5 km in some locations (Lawver et al., 1996; Simms et al., 2011).

The SSI rest on the Shetland Plate (Fig. 3), which is situated on the northern flank of the active Bransfield Strait rift basin, which reaches a maximum depth of 1950 m. The Bransfield Basin is currently spreading at a rate of 7 mm/a (Dietrich et al., 2004). The island's crustal thickness is 32 km with a lithospheric thickness estimated to be between 20 to 45 km (Haase et al., 2012; Ivins and James, 2005). Greenwich Island, KGI, and Livingston Island are moving north-northwest and away from the AP at a rate of 7-9 mm/a while Smith and Low Islands are moving in the same direction but at a rate of 2.2-3.0 mm/a suggesting they may rest on a different microplate. Differential northwest plate motion of the northeastern SSI near Elephant Island at a rate of 7 mm/a suggests they are coupled with the Scotia Plate as they are not moving transverse to the axis of rifting within the Bransfield Basin (Taylor et al., 2008).

The South Shetland Trench north and seaward of the SSI is the last remnant of a subduction zone that ran the length of the Western Antarctic Peninsula (WAP) (Maurice et al., 2003). Here, the former Phoenix Plate to the north subducted under the Shetland Plate driven by the spreading of the Antarctic-Phoenix ridge east of the Hero fracture zone (Larter and Barker, 1991; Taylor et al., 2008). Spreading at this ridge initiated ~50 Ma and terminated ~4 Ma when the remainder of the Phoenix Plate was amalgamated to the Antarctic Plate at the Shetland Trench (Larter and Barker, 1991) at which point back-arc rifting began south of the SSI forming the Bransfield Basin within the Antarctic continental

crust (Barker and Dalziel, 1983). There have been many earthquakes related to volcanism and rifting within the Bransfield Strait, which has been suggested as evidence for a transition into a spreading regime (Barker and Austin, 1994). Maurice et al. (2003) identified clusters of 150 earthquakes at a maximum depth of 65 km with most occurring <30 km deep indicating slow ongoing subduction at a rate of  $\sim 10$  mm/a. These earthquakes may represent thrust faulting, which is common in shallow dipping thrust interfaces of subduction zones. This is consistent with other young oceanic crust subducting at slow rates such as in Cascadia, the Austral Andes, and Nankai (Maurice et al., 2003). For comparison, the Tonga Arc is subducting at rates between 46 mm/a to 83 mm/a (Luo et al., 2018).

The northern AP south of the SSI is a passive margin and thus experiences less seismic activity than the SSI (Barker and Austin, 1998; Barker et al., 1991). The long-term tectonic uplift rates for the SSI have been estimated at between 0.39-0.48 m/ka using undated but assumed MIS 5e, 7, and 9 marine platforms as proxies for uplift (Pallas et al., 1997; Jouez et al., 2007; Watcham et al., 2011). Another estimate of long-term tectonic uplift was calculated by summing the depth of the Bransfield Basin (1950 m), with hundreds of meters of basal sediment, and the elevations of the SSI, whereby the maximum vertical throw would be roughly 3 km. Assuming an equal split between island uplift and basin subsidence over the period since the Antarctic-Phoenix ridge spreading stopped ( $\sim 4$  ma), the uplift rate would be approximately 0.45 m/ka. If the currently accepted Bransfield Basin spreading rate of 7 mm/a is used then the deep basin (50 km wide) (Gracia et al., 1997) would have taken 7 Ma to open, but it began  $\sim 4$  Ma suggesting either rifting started earlier, rifting rates were initially higher, or subsidence contributed to the depth of the basin. If opening of the Bransfield Basin

started earlier than 4 Ma, a long-term tectonic uplift rate of 0.22 m/ka might be more appropriate. These estimates lead to a range in values of between 0.22-0.48 m/ka. If uplift were constant through the Holocene, the range in long-term tectonic uplift rates between 0.22-0.48 m/ka yields 1.4-2.9 m of the 15.5 m of total uplift over the last ~8 ka on Fildes Peninsula, Maxwell Bay, KGI suggesting GIA dominates the RSL curve (Pallas et al., 1997; Watcham et al., 2011).

## **2.2. Glacial History**

The South Shetland Islands have been subjected to four phases of glaciation. During phase one the island chain was covered in an ice cap that connected the islands and extended ~50 km onto the northern shelf where it was grounded (Simms et al., 2011). This first phase of glaciation was followed by ice recession. During the second phase of glaciation ice caps were centered on individual islands with ice grounding on or near shore. The third and fourth phases of glacial advance are located on individual islands separated by a period of ice-recession.

The age of these phases remains uncertain. The timing of the local LGM in the SSI may be offset from the 20 ka B.P. global LGM timing (Seong et al., 2009). Few scientists from the 1960s and 1970s had considered oscillations of the ice front during the retreat from the LGM (Hobbs, 1968; John and Sugden, 1971; Hansom, 1979; Curl, 1980). Sugden and John (1973) originally correlated phase one to a glaciation prior to the northern-hemisphere LGM (~20 ka), potentially the North American Illinoian Glaciation (mid-Pleistocene 191-130 ka B.P.). However, Simms et al. (2010) suggests timing more consistent with the local AP LGM ~14-18 ka B.P. by interpreting seismic and cores collected on the SSI shelf. At this time the

ice sheet extended over the entire island chain encompassing an area 240 x 60 km with an ice shelf extending across the Bransfield Strait connecting the SSI to the AP (Simms et al., 2011; John and Sugden, 1971). Ice thickness is estimated to have been 570 m and grounded in water depths up to 400 m (Simms et al., 2011).

The interglacial between phases one and two was initially correlated to the Sangamon Interglacial (Sugden and John, 1973). More recent work suggests that this corresponds to the initial deglaciation from the local LGM ~14-15 ka B.P. (Seong et al., 2009; Simms et al., 2010). The second phase of glaciation was originally correlated to the Weichselian (Wisconsin) glaciation (75-11 ka B.P.) with a centering of ice caps on individual islands. This readvance is now suggested to postdate 7400 cal yr B.P. based on <sup>10</sup>Be exposure dating of erratics within moraines on Livingston Island (Hall, 2009). The ice advances during Phases 3 and 4 occurred at ~4 and ~<1 ka B.P. on Byers Peninsula (Palacios et al., 2020). The phase 4 ice advance may coincide with the northern-hemisphere Little Ice Age (LIA) (John and Sugden, 1971; Curl, 1980; Hall and Perry, 2004; Hall, 2007; Hall, 2010; Simms et al., 2012; Guglielmin et al., 2016; Yu et al., 2016; Chu et al., 2017).

Bentley et al. (2009) grouped Holocene climate within the AP region into 4 time periods. The Early Holocene Climatic Optimum (11-9.5 cal ka B.P.) is marked by a period of warmth as shown in stable isotope records from ice cores around Antarctica (Bentley et al., 2009). Marine Sediments in Maxwell Bay and cosmogenic ray exposure (CRE) dating on Barton Peninsula confirmed deglaciation began as early as 14 cal ka B.P. (Seong et al., 2009). Complete or partial readvance between 9595-7945 cal yr B.P. (calibrated years before

present; present is defined as 1950 C.E.) precedes the post Early Holocene Climatic Optimum (EHCO) period from 9.5-4.5 cal ka B.P. (Bentley et al., 2005b; Smith et al., 2007; Roberts et al., 2008). However, deglaciation did not occur synchronously across the SSI. For example, ice free beaches and lake basin sediments accumulated from 9.5-9.0 cal ka B.P. on KGI (Mäusbacher et al., 1989; Bentley et al., 2005a). Deglaciation of Byers Peninsula progressed from west to east initiating at 8.3 cal ka B.P with the central plateau ice free by 8.3-5.9 cal ka B.P. (Toro et al., 2013; Oliva et al., 2016; Ruiz-Fernandez and Oliva, 2016; Oliva et al., 2016). This deglaciation is consistent with significant glacier thinning and ice margin retreat on the WAP that continued until 8 to 7 cal ka B.P. (Bentley et al., 2006). By 6 ka B.P. glaciers on the AP across the Bransfield Basin were similar to, or smaller than present-day ice extent (Palacios et al., 2020).

The Mid-Holocene warm period (4.5-2.8 cal ka B.P.) also referred to as the Mid-Holocene Hypsithermal (MHH) or Mid-Holocene Climatic Optimum is characterized by rapid sedimentation, increased organic productivity, and increased biodiversity in lake sediments (Björck et al., 1996a). Reduced periods of sea-ice coverage and increased meltwater sedimentation are also noted for the period (Shevenall et al., 1996). Locally on Byers Peninsula, lake sediments contain evidence of a warm period between 3.2-2.7 cal ka B.P. (Björck et al., 1993). The Neoglacial Interval commenced after the MHH from about 2.5-1.2 ka B.P. and consisted of a shift to a colder climate and glacial advances (Bentley et al., 2009). A neoglacial advance into Maxwell Bay on KGI ended approximately 1.7 cal ka B.P. (Simms et al., 2011). Domo Lake located 360 m from the current glacier front on Byers Peninsula was deglaciated ~1.8 cal ka B.P. (Oliva et al., 2016). This timing is consistent with

Toro et al. (2013) suggesting deglaciation of easternmost Byers Peninsula was complete by 1.8 cal ka B.P. Cosmogenic ray exposure (CRE) dating of moraines and bedrock surfaces on Livingston Island confirmed a glacial advance of no more than 200m from the current glacier front on Byers Peninsula ~4 cal ka B.P. and 1 cal ka B.P. (Palacios et al., 2020) suggesting the central plateau was ice-free earlier than previously thought.

The Medieval Warm Period (MWP) is a period of increasing temperature and glacial retreat observed across the globe between 1000-800 yr B.P. (Luning et al., 2019). In the AP, evidence for it from 1.2-0.6 cal ka B.P. (Bentley et al., 2009) is primarily recorded in marine cores from the AP (Khim et al., 2002; Domack et al., 2003b). However, terrestrial evidence for a MWP across the AP include expanded ice-free areas on Anvers Island (Hall, 2009; Hall et al., 2010a; Yu et al., 2016) and accounts looking at mosses within Marguerite Bay, WAP (Guglielmin et al., 2016) suggest an age of 700-970 cal yr B.P. with glacial retreat rates of 1.6 m/yr during this time period.

The Little Ice Age (LIA) is a cold climate interval in the northern hemisphere whose coldest conditions occurred between 1400-1700 AD (Mann et al., 2009). It is marked by a period of cooler and less arid conditions across the North America Prairie (Miao et al., 2007) and cooler conditions across European lowlands (Johnston et al., 2010). In the southern hemisphere the LIA is observed from 700-150 cal yr B.P. as a period of increased sea-ice cover and colder sea-surface temperatures identified in the Palmer Deep sediment core (Shevenell et al., 2011). Glaciers have also been shown to have advanced across the AP during the LIA (Björck et al., 1996a; Domack et al., 1995; Shevenall et al., 1996; Hall, 2007;



Simms et al., 2012; Guglielmin et al., 2016; Simms et al., accepted). Hall (2007) and Simms et al. (accepted) both documented a glacial advance within the SSI during the LIA over the last 600 years. Recent Rapid Regional (RRR) warming from 150 cal yr B.P. to present (Bentley et al., 2009) is recorded in both sediment and ice cores and historical temperature records on the Eastern Antarctic Peninsula (EAP) and WAP where the warming is more pronounced in the WAP (Domack et al., 2003b; Bentley et al., 2009).

### **2.3. Glacio-Isostatic Adjustment (GIA) and Sea Level**

The solid Earth behaves in both a viscous and elastic manner in response to mass loading from ice, sediment, and water. The elastic response results from crustal rebound. The viscous response of the Earth to mass loading is a function of the viscosity of the mantle as it flows from ice-deflected bulges back to the center of ice loading (Carlson and Clark, 2012; Conrad, 2013). In more volcanically active regions, the viscous response is more rapid than in regions with cooler, more viscous mantle material (Larsen et al., 2005). When the solid Earth responds to ice-mass loading this is referred to as Glacio-Isostatic adjustment (GIA) (Whitehouse, 2018). GIA produces several typical signatures of relative sea-level change following the LGM that range from RSL rise in far-field regions such as Barbados to RSL fall in cratonic near field regions such as Hudson Bay, Canada (Peltier, 1999).

Earth rheology is a critical factor in determining how the crust will respond to mass loading. Regions with thicker lithospheres and more viscous upper mantles such as those within cratons behave more rigidly than regions with a thinner lithosphere and less viscous mantle such as those near regions with significant tectonic and/or volcanic activity. In general, the solid Earth response of the Earth's crust is to depress with an increase in ice-

mass and rebound with a decrease in ice-mass (Whitehouse, 2018). During the Holocene, despite rising eustatic sea levels RSL fell in near-field regions, which experienced ice-mass loss (Bentley et al., 2005; Palacios et al., 2020). Fretwell et al. (2010) mapped isobars of equi-elevation beach ridges throughout the SSI that were interpreted to represent differential isostatic uplift experienced throughout the island chain (Fig. 4). This map supports prior assertions of the ice cap being centered along the axis of the SSI chain (John and Sugden, 1971; Curl, 1980) during the local LGM (Simms et al., 2011).

Proximity to the ice margin determines whether a region or location is referred to as far-field or near-field in sea-level reconstructions. Sea level in far-field locations is controlled mainly by changes in ice volume through time while near-field locations are controlled more by the underlying rheology and local ice thickness (Lambeck et al., 2014). The rates of near-field GIA induced uplift vary due to underlying rheological properties. Differences in solid Earth response to ice loading between the SSI and the AP, let alone mainland Antarctica, vary greatly (Watcham et al., 2011; Whitehouse et al., 2012b; Nield et al., 2014). After the Larsen-B ice sheet breakup, which buttressed valley glaciers from unimpeded flow into the ocean, GPS recorded uplift rates at Palmer Station increased from  $0.08 \pm 1.87$  mm/a to  $8.75 \pm 0.64$  mm/a (Thomas et al., 2011). This natural experiment suggests the Earth beneath the AP may be more sensitive to recent ice-mass fluctuations than post-LGM ice-mass loss (Nield et al., 2014; Simms et al., 2018). The center of ice loading in the SSI is located between Livingston and KGI; isobars of the highest Holocene beaches in the SSI are centered on this region (Fig. 4) (Fretwell et al., 2010). Beaches closest to this loading center have experienced the greatest amount of uplift (Fretwell et al., 2010).

## 2.4. Raised Beaches

Otvos (2000) loosely defines a beach ridge as a relict strand plain ridge morphologically higher in elevation than the surrounding prograding strand plain and formed by wave and wind processes that record water levels up to several meters above high tide. Beach ridges also reflect periods of beach progradation (Taylor and Stone, 1996). The internal architecture of beach ridges often consists of a series of landward and seaward dipping strata (Lindhorst and Schutter, 2014).

Beach ridges form from the reworking of sediment by waves. Aggradation is achieved by wave overtopping and overwash (Lindhorst and Schutter, 2014). Beach-ridge elevation is a function of not only mean sea level, but also wave energy, storm energy, tidal range, grain size and shape, and sediment availability (Lindhorst and Schutter, 2014; Scheffers et al., 2012) as well as bathymetric profile, and underlying onshore bedrock topography. Sufficient wave energy is needed to move sediment against gravity to form ridges above high tide level. Abandonment of beach ridges promoting their preservation is often due to a fall in RSL caused by GIA or tectonics, which raises these beaches out of the littoral zone (Scheffers et al., 2011).

Strand plains are regions of little topographic relief between beach ridges that consist of seaward dipping strata (Lindhorst and Schutter, 2014). Sediment supply and storm recurrence interval control strand-plain formation (Lindhorst and Schutter, 2014). They form during relatively quiescent periods of decreased storminess and low wave energy under a continuous supply of sediment. They reflect periods of beach progradation formed by swash

sedimentation. Formation of the strand plain is halted when sediment supply is decreased or cut off or when storm waves cannibalize the beach material into beach ridges or transport it offshore.

Raised beaches are the most widely used method of resolving paleo-sea-level in polar environments (Hall and Perry, 2004; Hall, 2007; Hall, 2010; Simms et al., 2011; Tamura et al., 2012; Zurbuchen and Simms, 2019). Sea-level index points from beach ridge crests in this environment are used with the assumption that beach ridges form at a known elevation above sea level during periods of increased storminess. Many authors assume they form at an elevation of +2 m (Otvos, 2000; Hall, 2010; Lindhorst and Schutter, 2014). RSL curves derived from these features in Antarctica primarily record sea-level fall caused from glacio-isostatic uplift and this is likely the case in the SSI (John and Sugden, 1971; Bentley et al., 2005; Watcham et al., 2011; Zurbuchen and Simms, 2019). Recently studies have focused on using the internal stratigraphy and the geometry of raised beaches to refine their use in sea-level reconstructions (Lindhorst and Schutter, 2014; Costas et al., 2016). Other studies have focused on specific stratigraphic contacts, such as the angle where the beach face downlaps onto the underlying shoreface, which is thought to represent the low-tide level, as markers for paleo-sea-level reconstructions (Clemmensen and Nielsen, 2009; Nielsen et al., 2017). Lindhorst and Schutter (2014) identified two general reflections in ground penetrating radar (GPR) profiles of polar gravel beach-ridge plains, the prograding strandplain and the aggrading beach ridge, that can be used in paleo-sea-level reconstructions. However, both can be influenced by varying climatic and sediment supply conditions.

Raised beaches and isolation basins in Antarctica have been dated with radiocarbon ( $^{14}\text{C}$ ) (Hall and Perry, 2004; Watcham et al., 2011; Zurbuchen and Simms, 2019) and optically stimulated luminescence (OSL) (Simms et al., 2011; Simkins et al., 2013; Hong et al., 2021). However, using  $^{14}\text{C}$  in Antarctica is difficult due to uncertainties in the  $^{14}\text{C}$  reservoir and the dearth of organic material to date. Suggested  $^{14}\text{C}$  reservoir corrections range from 500 to 1400 years (Berkman and Forman, 1996; Bentley et al., 2005b; Hall, 2010). In addition to the uncertainties of the  $^{14}\text{C}$  reservoir, the sparse organic material found in Antarctica results in the use of reworked bones and organic material on the beach surface, typically yielding only minimum or maximum ages for the beaches (Hansom, 1979; Bentley et al., 2005; Hall, 2010).

The SSI arguably have the highest concentration of RSL studies in Antarctica in part due to the large expanses of ice-free beaches. However, existing ages of raised beaches in the SSI are concentrated on the lower elevation beach ridges and not the interconnecting strand plains. Thus, the resulting clusters of sea-level indices require extrapolation between them. Obtaining accurate ages on beach ridges as well as strand plains is critical for understanding GIA processes and constructing accurate sea-level curves. To date, stratigraphic relationships have been noted but not used to provide insights into the RSL history of the SSI.

## **2.5. Livingston Island Field Site**

### **2.5.1 Location and Beach Characteristics**

Livingston Island is located approximately 160 km north of the AP in the northeast-southwest trending Sub-Antarctic SSI. With a total area of 798 km<sup>2</sup> the island is the second largest in the SSI after KGI (1,150 km<sup>2</sup>) located ~80 km to the northeast (Fig. 1). Byers

Peninsula (62°34'35"-62°40'35"S, 60°54'14"-61°13'07"W) on the western end of Livingston Island is the largest ice-free region in the SSI (60 km<sup>2</sup>) (Figs. 2 & 6), followed by Fildes Peninsula on KGI (29 km<sup>2</sup>). Rotch Dome Glacier covers the eastern end of Byers Peninsula as well as the majority of the island and reaches a maximum elevation of 360 m (Palacios et al., 2020).

The bedrock on Byers Peninsula is mainly composed of weak bands of marine shales and sandstone of the Carboniferous Miers Bluff Series interbedded with friable basaltic, dyke-intruded basaltic agglomerates and augite-andesites of the Miocene Younger Volcanic Group (Adie, 1964; Barton, 1965; Hobbs, 1968). The oldest rocks on Livingston Island are the False Bay Schists, which are Precambrian or early Paleozoic in age (Hobbs, 1968).

The geomorphology of Byers Peninsula is comprised of a set of terraces suggested to be of marine origin because of the similarity in shape to the modern shoreline, the near uniform elevations, and the flat gently seaward dipping orientations (John and Sugden, 1971; Curl, 1980). The central platform at 85-100 m gently slopes from the center outward in all directions towards the sea. The 28-50 m platform on the periphery of the central platform parallels the modern coastline more closely than the central platform. This platform is less dissected by meltwater channels than the central platform and retains several remnant stacks. It dips gently seaward at 0.5-1° ending in a steep slope with gradients up to 30° above the 11-17 m platform. All major platforms above the 11-17 m platform are believed to have formed prior to the most recent phase of glaciation (local LGM). The 11-17 m platform is less altered than the two higher platforms and retains paleo sea stacks 2-4 m high. The 11-17 m platform

is thought to have formed after the LGM based on its degree of erosion and its dissection of the meltwater channels on the seaward edge of the higher elevation platform (Hansom, 1983). It dips seaward around 1-2° and is dissected by even fewer gullies than the 28-50 m marine platform. The gullies that do dissect the 11-17 m platform are linked to streams that dissect the overlying raised beaches (Fig. 4, 5, & 7) and source sediment to alluvial fans onshore and the modern beach when they reach the shoreline. The formation age of the ~3-8 m platform underlying the beaches is less clear because these platforms commonly rest within glacial troughs suggesting they formed after earlier glaciations. Striations on the 3-8 m platform are interpreted as glacial striations suggesting they predate the local LGM glaciation (John and Sugden, 1971) or as abrasions from debris-rich ice (Hansom, 1983) suggesting they may post-date the local LGM or one of the later phases of Holocene glacial advance. The lowest platform lies near modern sea level and is more dissected with gullies than the 11-17 m platform. Rotch Dome cuts across each of these features, which is why John and Sugden (1971) and others suggest they predate the most recent ice advance.

The series of Holocene raised beach ridges noted across the SSI cluster into three groups: 4-6 m, 8-12 m, and 15-20 m in elevation (John and Sugden, 1973; Barsch and Mäusbacher, 1986). The same groups are found on Byers Peninsula but at lower elevations than similar aged beaches located closer to the center of ice loading (Fig. 4) (Fretwell et al., 2010). Previous work on Livingston Island was only successful in compiling radiocarbon ages clustered on raised beach ridges ~11 m and lower. The 4-6 m elevation beach ridges of the South Beaches date to 400-700 cal yr B.P. (Curl, 1980; Hall, 2010; Hall, 2003; Hall and Perry, 2004), the 8-12 m beach ridges date to 1800-2600 cal yr B.P. (Hall and Perry, 2004;

Hansom, 1979; Hall, 2010), and the 15-20 m beach ridges date to 6000-7000 cal yr B.P. within the SSI (Hall, 2010). Hall (2010) extrapolates the RSL curve to the marine limit of 18-21 m on Byers Peninsula, which yields an age of 7500 cal yr B.P. but notes that this more than likely relates to a transgression. There is regional evidence (Sugden and John, 1973; Mäusbacher et al., 1989; Toro et al., 2013; Oliva et al., 2016) that ice recession began earlier between ~9500 to ~8300 cal yr B.P.

My study area is located on the South Beaches of Byers Peninsula (Fig. 2). The beaches I studied range in width from 500-1100 m and extend for a length of 9.7 km from Clark Nunatak in the east to Vietor Rock in the west with a tombolo just west of Cerro Negro (Figs. 2, 5, & 6) near the center (Hobbs, 1968) (Fig. 4). A similar set of beaches, Robbery Beaches, lie on the north side of Byers Peninsula but are thinner with a maximum width of 100 m (Fig. 2). This difference is likely due to differences between the submarine profile of the northern and southern sides of Byers Peninsula. The northern Byers Peninsula shelf has a slope of 124 m/1.6 km (slope=0.077) while the southern Byers Peninsula shelf has a slope of 18 m/1.6 km (slope=0.0112) (Curl, 1980). This submarine profile further serves to partially protect the south facing beaches from storm waves as they break farther offshore thus limiting erosion. The mixed sand-gravel and pebble clasts forming the beaches (Figs. 7 & 8) are derived from the Younger Volcanic group (Hobbs, 1968). They unconformably lie on the lower marine terraces with bedrock supported beach deposit depths up to 2 m where measured (John and Sugden, 1971) in the surveyed area. Tonalite cobbles are found on beach ridge crests and are thought to have traveled via longshore currents from Barnard Point, Livingston Island (Hobbs, 1968). Non-local ice-rafted debris (IRD) from the AP is also found on several of the



beach ridges on the South Beaches, which Hall and Perry (2004) interpret their higher density on the same beach ridges 2 and 4 from this study to represent cooler periods when debris-laden ice would travel farther distances.

### **2.5.2. Climatic Setting**

At 80 m elevation the average annual temperature on Livingston Island is  $-2.8\text{ }^{\circ}\text{C}$  and the average annual precipitation is 650 mm (John and Sugden, 1971; Bañón et al., 2013; De Pablo et al., 2014). At an elevation of 70 m on Byers Peninsula winds are predominantly from the west to northeast passing through north, with an average speed of 26 km/hr. Frequent storms with wind gusts exceeding 100 km/hr (max speed 139 km/hr) were recorded between 2001 and 2003 C.E. Calm periods represent just 1.4 % of the record (Bañón et al., 2013). On nearby Whalers Bay, Deception Island and Admiralty Bay, KGI, between 1944 and 1961 C.E. gale force winds were recorded 72 and 95 days of the year, respectively (Lindsay, 1971). The incident wind direction aids in creating larger storm waves on the western and northerly coasts where fetch is effectively limitless across the South Pacific Ocean (Hobbs, 1968; John and Sugden, 1971; Palacios et al., 2020). The southern coast is sheltered from these wind and storm waves to a higher degree and fetch is limited to around 160 km – the width of the Bransfield Strait. Summer waves in the Bransfield Strait have wind wave periods of 1.2 s with a mean height of 0.5 m. The wind waves in the nearby Scotia Sea have a mean period of 3-5 s and a mean height of 2 m. The swell waves in the Bransfield Strait have a mean period of 3 s and a mean height of 1 m while in the Scotia Sea they are 7-8 s and 3 m, respectively (Hansom, 1983). Sea ice rarely extends to the northwest of the SSI but where encountered persists for up to 200 days per year in the southeastern and

southern coasts and embayments of the SSI. These locations are also protected by fast ice for 6-8 months per year (Curl, 1980).

### **3. Methods**

#### **3.1. GPS**

Global positioning system (GPS) surveys were conducted using a Trimble NetR9 with a Trimble Zephyr Geodetic 2 RoHS antenna as a base station and Trimble TSC2 R7 with a Trimble Zephyr Geodetic antenna attached to a 2 m surveying pole for a Rover GPS unit. Roving Post Processing Kinematic (PPK) data was processed using Trimble Business Center (TBC). Coordinates are based on Datum Transformation ITRF2014, projection UTM Zone 20 South, and GEOID Model EGM96. Local base station data was incomplete resulting in too large of horizontal and vertical (3-5 cm) errors. This was due to the void of satellite tracking within the southern quadrant of the sky caused by either an 'overly aggressive' 30° elevation mask applied in the base station configuration file or a damaged antenna unable to view these quadrants. Upon failure of our base station (G412) to collect adequate data during portions of the field campaign, GPS was processed using a continuous base station set up ~35 km away on Livingston Island (BEJ2 -62° 39' 46.88939", -60° 23' 9.42703") operated by researchers from the University of Cádiz, Spain. The Spanish, BEJ2 survey utilized a Trimble R7 GNSS Base Station with a Trimble Zephyr Geodetic 2 Dome. This base station was chosen to be the initial adjustment base over three others on nearby Deception Island because it contained the shortest baselines, and was located on the same land mass, while the other stations were located on a volcanically active island. The base stations from Deception Island ~40-45 km away used unknown antenna and receivers (FUMA -62° 57' 41.00975", -60° 42' 59.33035"; BEGC -62° 58' 43.64928", -60° 40' 27.51466"; and PEND -62° 56'

9.83782", -60° 35' 34.32658"). The Canadian Geodetic Survey (CGS) Precise Point Positioning (PPP) tool was used to process the base station coordinates. Horizontal and vertical precision averaged  $1.5 \pm 1.4$  cm and  $2.3 \pm 1.9$  cm across all data points and days surveyed.

### **3.2. Ground Penetrating Radar**

GPR is a non-invasive subsurface imaging method that uses electromagnetic waves and their attenuation through different materials to document the internal structure of sedimentary deposits (Lindhorst and Schutter, 2014; Neal, 2004). GPR surveys were conducted using a Sensors and Software Inc. pulseEKKO PRO system with 200 MHz antennas and a step size of 0.5 m. Profiles were taken normal to and along shore in order to reconstruct the architecture of the raised beaches (Fig. 9). The setup allowed a vertical resolution of 0.10 m. Surveys were processed using EkkoView Deluxe software from Sensors and Software Inc. The data processing included standard dewow processing, a bandpass filter, and automatic gain control (AGC). The data was migrated by converting two-way travel time (TWT) to depth using the average radar velocity (0.101 m/ns) derived from a common midpoint (CMP) survey collected in the field. Finally, the radar profiles were topographically corrected to show true geometric relationships in the subsurface using post-processed synchronously collected GPS data. Radar reflection geometry was traced and examined to differentiate and classify radar facies and surfaces. Radar facies and surfaces were identified with criteria outlined by Neal (2004). Radar facies were identified by shape, dip, reflection configuration, and continuity (Table 7a). Radar surfaces were classified by their upper and lower boundaries as observed from reflection terminations in profile (Table 7b).

### **3.3 Tide Gauge**

A Valeport 740 Portable Water Level Recorder was deployed over the first three days of the field campaign at 62° 39'45.7759" S, 61°0'42.8248" W. The tide gauge was calibrated to the salinity and temperature during deployment in the field on February 24<sup>th</sup>, 2019. The instrument records pressure measurements every five minutes. Pressure values collected in the field were converted to depth using the Valeport Terminal X2 software (Theilen, 2020).

Mean tide level (MTL) was measured by averaging the mean high water and mean low water marks from the three days of data collected. Ideally this MTL would approximate local mean sea level (MSL). However, the pressure sensor was removed via kelp rafting after wrapping itself around the wiring between the transducer and the recording box during a high tide limiting our tide survey length to three days. Our new Livingston tide data was extended using the estimated 20-year National Tidal Datum Epoch (NTDE) for nearby Palmer Station following the NOAA Computational Techniques for Tidal Datums Handbook standard method for mixed tides (Evans et al., 2003). The corrected MTL for Livingston Island is +0.790 m relative to the tide gauge pressure transducer sensor (Theilen, 2020). This elevation offset was used to adjust the Trimble GPS elevations to local MSL (Theilen, 2020).

### **3.4. Radiocarbon Age Corrections**

Previously collected radiocarbon ages on Livingston Island were used to assign the ages of beach ridges 2 and 4 (Table 2). Samples collected on Livingston Island are from the South, Robbery, and President's Beaches on Byers Peninsula (Fig. 2). Nineteen out of the 33 <sup>14</sup>C ages available for Byers Peninsula that date beach formation were recalibrated and averaged for assigning ages to beach ridges. The remaining measurements were not used because they only gave maximum or minimum ages of beach ridge formation or returned post-modern

ages. Beach ridge 2 has been dated by Hall and Perry (2004), and Hall (2010). Beach ridge 4 has been dated by Hansom (1979), Hall and Perry (2004), and Hall (2010). One age from Curl (1980) was not used in the calculation because its age ( $1292 \pm 235$  cal yr B.P.) and elevation did not correspond to the observed beach architecture as well as the lack of reported sample coordinates. The 10 samples from Hall (2010) were collected approximately 1 km west of the portion of the South Beaches surveyed as part of this study (Fig. A1).

Beach ridges above beach ridge 5 are undated on Livingston Island. Therefore, we correlate beach ridges from nearby Greenwich Island and KGI to Livingston Island using the isobars of Fretwell et al. (2010). Twenty-one  $^{14}\text{C}$  ages from these nearby islands were recalibrated and averaged to assign ages to the upper beach ridges of the South Beaches. Beach ridge 5 was dated by Hall (2010) on Ash Point, Greenwich Island. Beach ridge 9 was dated by Del Valle et al. (2002) and Lindhorst and Schutter (2014) on Potter Peninsula, Maxwell Bay, KGI, and by Barsch and Mäusbacher (1986) from beach ridges on Fildes Peninsula, Maxwell Bay, KGI. An additional 14 ages from Potter Peninsula were used to help assign ages to beach ridges 2 and 4.

The material dated in the region including whale and penguin bones, mollusks, and seaweed, do not necessarily date beach formation, but rather are interpreted in some cases by some authors as a limiting date of beach formation (Hall and Denton, 1999; Hall and Perry, 2004; Hall, 2010b). A bone resting on a beach ridge is interpreted as a minimum age for the formation while a bone incorporated within a beach ridge likely dates the age of beach formation if time from death to deposition is swift otherwise it provides a maximum age of

beach formation (Hall, 2010). Samples would also be evaluated for degree of reworking to determine how the  $^{14}\text{C}$  age relates to what it is used to date.

CALIB 8.2 was used to correct for the  $^{14}\text{C}$  reservoir and calibrate radiocarbon ages to calendar years (Tables 2 & 3) (Stuiver et al., 2021). The Southern Ocean reservoir has the highest radiocarbon reservoir ages in the world's surface oceans (Hall et al., 2010b). Using U-Th coupling and  $^{14}\text{C}$  ages from a series of coral collected from moraines in the Ross Sea, Hall et al. (2010b) suggested the Southern Ocean radiocarbon reservoir effect has remained rather constant at  $1144 \pm 120$  years ( $2\sigma$ ) over the past 6000 years. This value was updated slightly given the recent update to calibrations in CALIB 8.2 (Stuiver et al., 2021). This calibration was conducted using the MARINE 20 dataset (Heaton et al., 2020) with a Holocene Southern Ocean  $^{14}\text{C}$  reservoir correction ( $\Delta R$  value) of  $635 \pm 42$  (Hall et al., 2010b). Strand plains have not been dated using radiocarbon but were sampled for future optically stimulated luminescence (OSL) age-dating.

Strandplain ages are estimated using the lateral distance between beach ridges utilizing equation 1 for progradation rate (below).

**Equation 1:**

$$(D_n - D_{n+1}) / (T_n - T_{n+1}) = \text{PROGRADATION RATE (M/YR)}$$

Where  $(D_n - D_{n+1})$  is the distance between the two beach ridges and  $(T_n - T_{n+1})$  represents the difference in ages between beach ridges  $n$  and  $n+1$  (Table 5). The progradation rate is extrapolated between assigned beach ridge ages to estimate the age of the undated strandplain (Table 6). This strandplain age estimation of beach progradation is an average

and does not consider stillstands, transgressions in RSL, or the beach and bathymetric profiles. Thus, it only provides an estimate within my study area.

### **3.5. Bedrock Erosion**

To evaluate whether the marine platforms were possibly formed or only trimmed during proposed transgressions a simple cliff erosion rate estimate was performed. I estimated three linear retreat rates of bedrock removed between scarps by measuring the distance between each successive bedrock scarp face under beach ridges 9, 4 & 5, 2, and the modern beach. I then divided these distances by the assigned ages of the beach ridges. Rates of bedrock erosion are estimated by measuring the lateral distance between GPR-interpreted wave-cut notches, also referred to as scarps, in bedrock within the overall seaward-dipping planar platform that extends seaward from the Holocene beach-backing cliffs (Fig. 10) utilizing equation 2 (below).

#### **Equation 2:**

$$(D_n - D_{n+1}) / (T_{n-1} - T_n) = \text{EROSION RATE (M/YR)}$$

Where subscripts reflect relative formation in a sequence of 3 eroded scarps formed landward to seaward in decreasing elevation along a marine platform (Fig. 11). The distance of each scarp face is measured from the modern beach and  $D_n - D_{n+1}$  is equal to the lateral distance of erosion between scarp  $n$  and the younger seaward scarp  $n+1$ .  $T_{n-1}$  and  $T_n$  represent the ages of the beach ridges overlying the older, landward scarp,  $n-1$ , and the next seaward scarp,  $n$ , respectively. The offset in age selection is because the erosion likely occurred after the higher elevation beach ridge ( $n-1$ ) formed and must have formed before or during the formation of the beach ridge above the scarp ( $n$ ) (Fig. 11, Table 8).

### **3.6. Sediment Trenching**

Pits no more than 1 m in each axis were dug to sample sediment within the beaches (Fig. 12). The original goal was to sample sediment for optically stimulated luminescence age dating while also providing ground truth of reflections observed in GPR. After sampling for OSL, material descriptions and photos were taken of 28 sediment pits (Figs. A2-A38. Tables A1-A28).

## **4. Results**

### **4.1. Elevations**

GPS surveys were collected along the crest of beach ridges 1, 2, 4, 5, and 9 (Fig. 13). Beach 1 is the modern beach where an 800 m survey along the crest has an average elevation of  $1.65 \pm 0.20$  m amsl (Fig. 13, Table 1). Above beach ridge 1 lies a series of elevated beach ridges. Some of these raised beach ridges stand anomalously high compared to the strandplains and other minor raised beaches. These are referred to here as stranded beach ridges. Beach ridge 2 is the first of 4 in the series of beach ridges identified on Byers Peninsula and has an average elevation of  $4.29 \pm 0.78$  m amsl along two ~470 m surveys along its crest (Fig. 13, Table 1). Beach ridge 2 is dissected by streams oriented normal to the coast that are fed by runoff from higher elevation platforms (Figs. 10 & 14). Beach ridge 2 is topographically isolated from the strandplain seaward and landward by 3 m and 1.6 m, respectively (Figs. 15-24). Beach 3 is located on the seaward flank of beach ridge 4 and its elevation was measured using 15 GPS points collected during sample collection. The elevation of beach ridge 3 is  $3.85 \pm 0.14$  m amsl. Beach ridge 4 is the second stranded beach ridge and has an average elevation of  $8.06 \pm 1.03$  m amsl (Fig. 13, Table 1) along a cumulative



930 m transect measured along its crest. The strandplain elevation seaward of the flanks of the stranded beach ridge 4 crest is -4.6 m and the strandplain elevation landward of the stranded beach ridge crests of 4 and 5 is -0.2 m relative to the crest of stranded beach ridge 4 (Figs. 15-24). Beach ridge 5 is the third stranded beach ridge and has an average elevation of  $9.54 \pm 0.70$  m amsl along a 1400 m GPS survey of its crest (Figs. 5 & 13, Table 1). Beach ridge 5 has a prominence of 5.9 m above the strandplain seaward of beach ridges 4 and 5 and 0.78 m above the landward strandplain (Figs. 16-24). Beach ridges 4 and 5 conjoin at several points along the South Beaches (Fig. 5). Beach ridges 6, 7, and 8 are weakly developed beach ridges within the strandplain only a few centimeters higher than the surrounding strand plain that have evaded fluvial reworking (Figs. 5 & 10). Beach ridge 6 has an average elevation of  $9.55 \pm 0.21$  m amsl along a 70 m survey of its crest (Figs. 5 & 13, Table 1). Beach ridge 7 has an average elevation of  $11.03 \pm 0.17$  m amsl along a 170 m survey of its crest (Figs. 5 & 13, Table 1). Beach ridge 8 has an average elevation of  $11.73 \pm 0.20$  m amsl along a 120 m survey of its crest (Figs. 5 & 13, Table 1). Beach ridge 9 is the fourth stranded beach ridge and is chiefly identified east of the prominent tombolo in the study area and south of Cerro Negro (Figs. 2 & 5). This is the only location I identified beach ridge 9 as a prominent stranded beach ridge not partially buried by scree from more landward platforms or covered by deep snow and ice. A 170 m survey along the crest of beach ridge 9 yielded an average elevation of  $13.59 \pm 0.19$  m amsl (Figs. 5 & 13, Table 1). At this location beach ridge 9 is better defined and lies 2.9 m above the seaward strandplain and 2.4 m higher than the landward strandplain between it and the cliffs backing the South Beaches (Figs. 24-26).

#### **4.2. Radar Facies**

Radar reflections were classified into six radar facies following the scheme proposed by Neal (2004) (Table 7A). Seaward dipping facies (rf-s) consist of moderately continuous, sinuous/wavy and subparallel to oblique/non-parallel, seaward dipping reflections with an apparent dip (AD) of 25-50° and a true dip (TD) of 6-15° (Fig.17, Table 7A). Landward dipping facies (rf-l) consist of moderately continuous subparallel, parallel/sinuuous, landward dipping reflections with an AD of 9-20 ° and a TD of 2-5 ° (Fig. 17, Table 7A). Discontinuous facies (rf-d) consist of discontinuous randomly dipping, semi-chaotic reflections (Fig. 23 at ~300 m, Table 7A). Aggradation facies (rf-ag) consist of continuous horizontal and concave-down reflections with low TDs of 1-2°. These facies are often observed draped over seaward topographic breaks in topography (Figs. 15-26, Table 7A). Flat-lying facies (rf-f) consist of continuous and strong planar horizontal reflections located between beach ridges in topographic lows on the beach surface. Reflections terminate in a planar fashion against bedding with little to no apparent erosion (Figs. 24 & 26, Table 7A). Channelized facies (rf-c) consist of chaotic, or lack of reflections overlain by discrete areas where surrounding reflections abruptly terminate and the space between the abrupt terminations is marked by flat lying and continuous reflections that terminate against the same surface. Elevation of surface s2-b within the region of reflection truncation that rf-c fills is often observed to be locally lower than the surrounding elevation of surface s2-b (Fig. 15 & 16, Table 7A).

### **4.3. Radar Surfaces**

Radar reflection terminations were used to identify and classify three surfaces following the scheme proposed by Neal (2004) (Table 7B). Radar surface s1-e is defined by the termination of reflections in a linear arrangement or with a linear reflection along the

terminus of a set of reflections (Fig. 18, Table 7B). This surface most often separates two packages of facies rf-s within the strandplain. Surface s2-b is marked by an increase in hyperbolas overlying ringing multiples and/or the regions absent of reflections (Fig. 25, Table 7B). This surface most often separates facies rf-s, and to a lesser extent facies rf-ag and rf-l, from interpreted bedrock. Surface s4-tl is marked by the upper boundary of reflections pinching out against a strong horizontal-planar overlying surface (Fig. 18 from 190-290 m, Table 7B). This surface most often separates facies rf-s from the rf-ag or rf-f facies.

#### **4.4. Beach Ridge Architecture**

GPR profiles across the stranded beach ridges 2, 4, and 5 (as well as one example from beach ridge 9) contain facies rf-s separated from the overlying facies rf-l and rf-ag by radar surface s1-e (Figs. 15-26). This succession is usually observed over a relatively large seaward step down in topography of surface s2-b. This succession is found beneath stranded beach ridges 2, 4, 5, and 9 (Figs. 15-26). The exception to this is beach ridge 3 (Figs. 23 & 24), where small-scale beach ridge internal geometries are found beneath a less pronounced ridge. Within beach ridge 3 a similar architecture is observed as that within the stranded beach ridges: an erosional truncation of radar facies rf-s overlain by facies rf-l and rf-ag (Figs. 23 & 24). However, this beach ridge lacks the bedrock support of a scarp and rests on the seaward flank of stranded beach ridge 4 and 5 deposits, which are underlain by a bedrock scarp. In stream cuts within beach ridges 2, 4 & 5, and 9 immediately along strike with this GPR reflection configuration, these seaward steps in elevation of radar surface s2-b appear to correlate with erosional scarps cut into the underlying bedrock platforms that are draped with beach deposits (Fig. 14). With one potential exception from beach ridge 4 (Fig. 24), radar facies rf-s is not observed continuously across the bedrock scarps. The predominant facies

observed within the strand plains between these stranded beach ridges is rf-s and to a lesser extent rf-ag. These facies are separated by seaward dipping erosional surfaces (s1-e) with a TD near that of the rf-s facies. There is one exception landward of beach ridge 9 where rf-s is observed with vertically aggrading bed geometry (Fig. 24). The flat-lying facies (rf-f) is located overlying the strandplain and seaward dipping reflections (rf-s), which they truncate in some areas (Figs. 19, 24, & 26). Facies rf-f are observed with possible interfingering of aggradational facies (rf-ag) in some locations (Fig. 19). The channelized facies (rf-c) are located within the strandplain region and appears to erode into both the seaward dipping facies (rf-s) as well as into the top bedrock surface s2-b. Unlike the flat-lying facies, no coherent radar facies are located beneath the channelized facies.

Beach ridge deposits are between 3-3.5 m thick while strand plain deposits are between 2-2.5m thick. Thickness varies little within each region on the beach.

#### **4.5. Radiocarbon Ages**

Radiocarbon ages from prior studies were recalibrated for use in this study (Tables 2 & 3, Fig. A1) (Hansom, 1979; Curl, 1980; Bentley et al., 2005; Hall, 2010; Hall and Perry 2004; Lindhorst and Schutter, 2014; Barión et al., 2019). Raised beaches increase in age with elevation and distance from the modern shore. Beach ridge 2 yielded an average age of  $370 \pm 160$  cal yr B.P. (Table 4). Beach ridge 4 yielded an average age of  $1790 \pm 189$  cal yr B.P. (Table 4). Beach ridge 5 yielded an average age of  $1940 \pm 201$  cal yr B.P. (Table 4). Beach ridge 9 yielded an average age of  $5460 \pm 214$  cal yr B.P. (Table 4).

Strandplain ages were estimated using the average progradation rates between ridges (Eq. 1) (Tables 5 & 6). Progradation rates of strandplains between beach ridges 1 and 2 average  $0.29 \pm 0.23$  m/yr (Table 5). Average progradation rates decreased to  $0.12 \pm 0.03$  m/yr between beach ridges 2 and 4 (Table 5). Average progradation rates between beaches 5 and 9 are  $0.11 \pm 0.01$  m/yr (Table 5). Beach ridges 3, 6, 7, and 8 are estimated to have formed 1620 cal years B.P., 2900 cal years B.P., 4142 cal years B.P., and 4762 cal years B.P., respectively (Table 6). However, the distances used in the progradation estimation varied between any two beach ridges due to variations in the orientation of the coast. Calculated average distances between successive beach ridges 1 & 2, 2 & 4, and 5 & 9 yield distances of 106 m, 176 m, and 397 m, respectively (Table 8). Review of satellite imaging confirms the averages presented are representative of the South Beaches. These distances are also used to estimate possible rates of horizontal bedrock erosion (Table 8).

#### **4.6. Bedrock Erosion Rates**

The rate of bedrock erosion forming the scarp observed in the GPR profile beneath stranded beach ridge 9 is 0.10 m/yr (Table 8). The scarp under stranded beach ridges 4 and 5 observed in GPR profiles and stream cut outcrops retreated at an estimated rate of 0.05 m/yr (Table 8). The scarp under stranded beach ridge 2 observed in a stream cut outcrop and in GPR profiles eroded at a rate of 0.07 m/yr (Table 8). The rate for the platform at sea level was not estimated because the modern beach at its seaward edge is still being formed. The age of 0 cal yr B.P. for the modern beach resting on the platform at sea-level reflects the present, not the limiting age of scarp abandonment used for estimating the remaining erosion rates.

#### **4.7. Sediment Trenches**

Sediment trenches provided control to the observations made using GPR. In total, 28 sediment trenches were dug to collect OSL samples (Fig. 9, Figs. A2-A38, Tables A1-A28). Within beach ridges sedimentary beds of coarse sand between 5-15 cm are common. These beds are routinely interrupted by gravel and pebble beds ~5cm thick. Strandplains contained more silt-sized particles and fewer pebble and cobble beds landward of beach ridge 5. However, beach ridge 8 contains 10-15 cm thick sandy gravel beds. Grains within sediment pits LV19-35 through LV19-39 are notably more angular than grains within the other sediment pits. Sediment pits from beaches 2, 4, 5, and 9 yielded more pebble-rich beds compared to the strandplains. Beach ridge 4, often identified by the coarseness of its surficial deposits, was coarser than the strandplain deposits, but notably finer internally than beach ridges 2, 4, and 9. All pits displayed a pebble veneer at the surface regardless of underlying coarseness. Bedrock was never reached on the Holocene beaches within these pits but was observed at depths of 2-3 m within stream cuts.

## **5. Discussion**

### **5.1. Interpretation of Ground Penetrating Radar**

#### **5.1.1. Radar Facies**

Radar facies were interpreted based on previous work on sandy and mixed sand and gravel beach ridges (Billy et al., 2014; Carter, 1986; Clemmensen and Nielsen, 2009; Engels and Roberts, 2005; Lindhorst and Schutter, 2014; Souza et al., 2018; Zurbuchen and Simms, 2019). Based on the seaward dip and continuous nature of radar facies, rf-s is interpreted to be sediments deposited by swash processes on the foreshore during periods of lower wave energy and abundant sediment supply (Table 7A). Based on the landward dip and location

landward of the scarp face, radar facies rf-l was interpreted as sediments deposited by overwash processes during periods of increased wave energy or a decrease in sediment supply resulting from strandplain cannibalization and reworking into a beach ridge (McKay and Terich, 1992; Lindhorst and Schutter, 2014) (Table 7A). The observation of this progradational facies with a vertically aggrading stacking pattern has implications for sediment supply and/or oscillations in RSL. Based on its horizontal and concave down orientation and location within topographic highs and composition of the upper beds of stranded beach ridges of radar facies, rf-ag was interpreted as sediments deposited during periods of wave runup and overtopping, which suggests increased wave energy, a decrease in sediment supply, or a rise in RSL (Lindhorst and Schutter, 2014; McKay and Terich, 1992). This aggradational radar facies rf-ag is found interfingering with flat lying deposits of rf-f. Erosional truncation is rare within this facies (Figs. 15, 16, 18, 19; Table 7A). Based on its chaotic reflections not typically observed in profiles from prograding beaches, radar facies rf-d is interpreted as a region of reworked sediment, or a cobble rich bed resting on bedrock attenuating the GPR signal (Table 7A). Based on its location in topographic lows, horizontal-planar nature, increase in silt content within sediment pit LV19-32 along GPR line 25, and observations of lagoons existing between beach ridges, radar facies rf-f is interpreted as lagoon deposits (Figs. 15 & 16, Table 7A). Overwash likely filled accommodation behind the beach ridges. Tidal sedimentation is possible if tidal inlets connected the lagoon with the open ocean when the region between stranded beach ridges was at or below sea level. Tidal inlets were observed on the South Beaches connecting the open ocean with lagoons between beach ridges 2 and 4 (Fig. 14). Fluvial processes are another likely sediment transport mechanism because I observed active streams crosscutting abandoned lagoon deposits to reach the

modern lagoon behind beach 1 (Fig. 14). The armoring of the beach surface observed in every sediment pit suggests fine grained sediments were winnowed by the wind. The strong wind field in the region makes aeolian sediment transport a likely mechanism of lagoon infilling. Based on observations of fluvial deposits during GPR collection, bedrock erosion and channelization in GPR profiles, landward and seaward dipping reflection orientations, and truncation of older seaward dipping reflections, radar facies rf-c is interpreted as fluvial deposits (Figs. 15, 16, 19, 20, & 23, Table 7A).

### **5.1.2. Radar Surfaces**

Radar surfaces are interpreted following the methods of Lindhorst and Schutter (2014) and Neal (2004) (Table 7B). Based on the seaward dipping truncation of reflections and location between beds of rf-s, radar surface s1-e is interpreted as an erosional surface. This interpretation suggests erosion was caused by a decrease in sediment supply or an increase in wave action each resulting in the erosion of beach material (Table 7B). Lindhorst and Schutter (2014) suggests the degree of shelter a coast receives controls the amount of erosional unconformities and therefore the quality of that beach as a recorder of sea level. The South Beaches are relatively sheltered due to their south facing direction compared to the Robbery Beaches on the north side of Byers Peninsula, but contain numerous erosional surfaces compared to beaches from similar studies in the AP region (Lindhorst and Schutter, 2014; Zurbuchen and Simms, 2019). Based on the abundance of refraction hyperbolas and/or absence of reflections, radar surface s2-b is interpreted as the top of the bedrock with a veneer of cobbles (Table 7B). This bedrock is observed within stream cuts immediately adjacent to beach ridges where bedrock scarps are interpreted in GPR profiles (Figs. 15-26). Based on the upper boundary of reflections obliquely pinching out against an overlying



surface or strong planar horizontal reflection, observations of a beach surface armored with a pebble veneer, and considering the wind regime of the SSI, radar surface s4-t1 is interpreted as a deflation pavement with minimal erosion or reworking by wave energy. Minor erosion accompanies this surface which is typically only truncated by seaward dipping erosive surfaces similar in geometry to prograding beach deposits (Table 7B).

## **5.2. Controls on Beach Ridge Architecture**

One of the most prominent features within the raised shorelines of the SSI are the prevalence of stranded raised beach ridges 3 to 6m above the seaward strandplain, separated by 70 m to 400 m of lower-lying strandplain. These levels appear to correlate across the SSI (Fig. 4) (Fretwell et al., 2010). Their formation may reflect a number of potential formative mechanisms including: (1) tectonics, (2) tsunamis, (3) changes in wave direction and energy, or (4) GIA.

### **5.2.1. Tectonics (Earthquakes)**

One possible mechanism for the formation of the stranded beaches is co-seismic uplift. Coseismic uplift is a common occurrence across subduction margins such as that found within the SSI. Tectonic uplift of the entire island chain as one block would be needed given the widespread correlation of the raised beaches (Sugden and John, 1971; Hansom, 1983; Fretwell et al., 2010). Whole island chain uplift is possible given observations of uplift from the 1964 M9.2 earthquake and tsunami off the coast of Alaska. Uplift zones of 15 m across an area of 965 km by 210 km were observed (Plafker, 1969) and is more than adequate to encompass the dimensions of the SSI. The megathrust tectonic regime is similar between the two regions making rapid uplift a plausible stranded beach ridge forming hypothesis (Plafker,

1969; Barsch and Masbaucher, 1986; Taylor et al., 2008; Dinther et al., 2019). Additionally, no Holocene fault scarps have been identified within the SSI as would be expected if fault rupture during earthquakes caused uplift of the beaches to form the isolated ridges across the island chain (Simms et al., 2012).

The architecture of the stranded beach ridges as recorded in GPR reflections also do not fit what might be expected if beach formation were a result of coseismic uplift. Beach material is observed to have draped across the seaward edge of scarps that underlie the beach ridges (Figs. 15-26). If the beaches were raised predominantly by coseismic uplift, one might expect to see two discrete and separate packages of sediment separated by the scarps. However, I observe parasitic beaches (e.g., beach 3) with small scale beach ridge internal geometries (Figs. 23 & 24) on the seaward flanks of the stranded beach ridges (e.g., beach ridge 4), which would not exist if coseismic uplift during the Holocene created these beach ridges during a singular event. Furthermore, I observe rf-s and rf-l truncated across most scarps while rf-ag is observed to drape the scarp. These three separate radar facies are all suggestive of different wave conditions making their deposition. Creating three distinct wave conditions during a singular coseismic event would be difficult.

However, long-term tectonic uplift has likely shaped the overall morphology of the SSI even though I argue against Holocene coseismic uplift as a method of stranded beach formation. Long-term tectonic uplift rates estimated at 0.4 to 0.48 mm/a (Pallas et al, 1997, Watcham et al., 2011) are several orders of magnitude lower than observed rates of RSL fall across the SSI. The marine terraces above the 11-17 m platform that uniformly cut across the

SSI likely reflect long-term uplift of the islands ‘as one block’. The 275 m beaches observed by John and Sugden (1971) attest to long-term tectonic uplift of the island chain. GIA is less likely to have caused this longer-term uplift as the Earth would have relaxed during interglacials. Additionally, these platforms appear to pre-date the LGM.

### **5.2.2. Tsunami**

Due to the active tectonic setting of the SSI, tsunamis are a likely occurrence on the region’s coastlines. However, a tsunami origin for the stranded beach ridges is unlikely due to their compound sedimentary architecture in that they are composed of several sedimentary packages separated by erosional surfaces (Figs. 17 & 21). These surfaces suggest multiple periods of ridge growth separated by erosive surfaces of varying ages. Like coseismic uplift, a tsunami is a one-time event usually creating a single, not compound feature (Costa and Andrade, 2020). Additionally, tsunamis would impact beaches along different facing coasts with different bathymetric profiles in a non-uniform manner due to their high spatial variability along even a single coastline (Koster et al., 2013). This is not observed in the SSI where beaches in every orientation share similar elevations regardless of orientation towards the Southern Ocean or the Bransfield Basin. The beaches on the northern and southern facing coasts of Byers Peninsula provide a good example of this (Fig. 2).

### **5.2.3. Wave Energy**

In the model of gravel beach-ridge plain evolution put forth by Lindhorst and Schutter (2014) strand plains and beach ridges differ architecturally. Their model of beach formation assumes a constant fall in sea level throughout the Holocene and proposes two modes of beach formation. Mode 1 is net strandplain progradation by swash sedimentation and

progradation with sufficient sediment supply at the beach face. The progradation and width of the strandplain is only influenced by sediment starvation or storm interval. Mode 2 is of berm ridge development with less sea-ice coverage and increasing storm interval, which acts destructively to cannibalize the strandplain and redeposit it during vertical and lateral beach ridge building. As beach ridges aggrade vertically, there is a critical elevation where sediment transport can no longer act constructively on the beach ridge. The architecture of the beach ridge is influenced by wave run-up height. The mechanism for vertical aggradation of beach ridges in this model is wave overtopping proceeding just over the ridge crest whereby rapid percolation through gravels leads to sediment accumulation at the swash limit (Orford and Carter, 1982; Lindhorst and Schutter, 2014). Exceptional storms or sediment starvation can cause erosional surfaces in the deposits. Between storms, swash sedimentation and progradation of the strandplain continues. The lateral distance of strandplain progradation serves to protect the beach ridge. Once progradation has progressed to a critical point, and the storm interval is unable to erode enough strand plain to act upon it, the beach ridge becomes stranded. This restarts the model where a new beach ridge forms seaward of the older beach ridge. The key factor is storm reoccurrence interval as most storms will not erode the entire strandplain. Many consecutive storms are needed to reactive an abandoned beach ridge. Lindhorst and Schutter (2014) tested their storm interval and wave energy formation model by comparing three field sites under different wave exposure. They concluded that the number of beach ridges preserved increased on more sheltered coasts and fewer but larger beach ridges with more erosional surfaces were found on more exposed coasts. Additionally, they concluded that the shift in beach ridge orientations could not be caused by an external trigger such as wave action alone because of the different facing coasts

but rather, internal factors such as wave refraction around variations in bedrock topography closer to sea level during constant RSL fall was the cause.

Similar to the case of the tsunami, wave action alone is not likely the cause of discrete elevated beach ridge formation because of the uniformity of beach elevations regardless of the degree of sheltering or varying incident wave directions the coast receives. As high energy waves produce fewer but larger beach ridges and lower wave energy produces multiple smaller beach ridges (Lindhorst and Schutter, 2014), if their formation was dependent on beach energy, their distribution and elevations should reflect local wave conditions, but they don't.

#### **5.2.4. Glacial-Isostatic Adjustment**

One of the most distinct features of the stranded beach ridges is their location above a bedrock scarp, and their hosting of progradational beach facies overlain by an erosional surface and overwash deposits. I interpret the order of deposition to reflect progradation concurrent with RSL fall deposited uniformly upon bedrock (Fig. 17). Where I diverge from the beach ridge formation model of Lindhorst and Schutter (2014) is my interpretation that the erosion and overwash deposits indicate a pause or reversal in sea-level fall with accompanying transgression that erodes into the prograded beach deposits of rf-s as well as into the underlying bedrock itself, cutting the scarp observed beneath the stranded beach ridges (Figs. 17 & 21). Observations in radar profiles of prograding rf-s directly overlying the bedrock scarp (s2-b) below the stranded beaches and seaward of the scarp is evidence of continued progradation after deactivation of the stranded beach ridge (Fig. 17). The stranded beach ridge elevation may be enhanced by the increased rates of RSL fall shortly following

RSL rise. Based on a simple GIA model with parameters appropriate for the SSI, Simms et al. (2012) suggested uplift rates as high as 12.5 mm/yr were possible during the last 300-500 years following the retreat of glaciers from the LIA. This rate of RSL fall would raise the stranded beach ridge above the active beach more so than a prograding strandplain would provide shelter from wave energy.

GIA-driven adjustment of the Earth's surface is another mechanism for producing climate-driven changes in shoreline elevation in a weak rheological region such as the SSI. A model for beach formation that calls on GIA is possible across a region the size of the SSI, especially given the sensitivity to ice-mass fluctuations (Simms et al., 2012; Simms et al., 2018; Zurbuchen et al., 2019). GIA-driven RSL rise on a regional scale can explain the existence of equivalent elevation beach ridges across shorelines irrespective of differences of both beach orientation and exposure to wave energy. Regardless of orientation, sea level is at the same elevation along every coast whether actively prograding, building, or eroding. Elevation variations of concurrently formed beaches only differ with varying rates of GIA recovery following ice-mass fluctuations in this model.

Lindhorst and Schutter (2014) claim strandplains form during periods of prevalent sea-ice cover and suggest this enhanced sea-ice should coincide with cooler periods and glacial advances but do not consider oscillations in RSL from GIA. They date the formation of beach ridges on Potter Peninsula to 4.3, ~3.1, 1.9, and after 0.65 cal ka B.P., interpreting this timing to coincide with increased storminess and decreased sea-ice cover and assume strandplain deposition occurred between these ages. While an increase in wave energy is

likely to have existed due to RSL rise and the resulting increase in offshore water depth during beach ridge deposition, the ice advance and climate assumptions are out of phase with known glacial advances and regional cooling (Sugden and John, 1973; Curl, 1980; Björck et al., 1996; Domack et al., 2002; Hall and Perry, 2004; Hall, 2007; Hall, 2009; Hall, 2010; Simms et al., 2012; Guglielmin et al., 2016; Yu et al., 2016; Bentley et al., 2009; Michalchuk et al., 2009; Shevenell et al., 2011; Chu et al., 2017). Strandplains formed during known warm periods marked by glacial retreat and perceived GIA uplift with accompanying RSL fall akin to a forced regression. The ages of formation for their beach ridges align more closely with cooler periods and glacial advance. Strand plain formation during periods with high storm recurrence interval and decrease in sea-ice cover further allies with a beach formation controlled by GIA. Additionally, variations in sea-ice cover cannot explain the correlative elevations of the beach ridges throughout the SSI.

So, what drives these RSL rises and falls? I suggest GIA. Ice advances may lead to minor transgressions while their retreat would lead to rejuvenated uplift. The homogeneity regardless of shore orientation, varying wave energy, lack of fault scarps, and presence of parasitic beaches on the seaward flank of stranded beach ridges does not align with stranded beach ridge formation by coseismic uplift, higher wave energy, or tsunamis. Therefore, I favor a stranded beach ridge formation theory predominantly controlled by GIA-related RSL fall with minor transgressions (Fig. 30). During the initial ice advance and RSL rise, the older beach deposits would be eroded, and the now exposed bedrock would also be eroded forming the bedrock scarps. Higher overwash may be aided by deeper water depths across the platform due to the RSL rise allowing waves to break closer to the shoreline and increasing

the efficiency of beach ridge building and clast rounding without the need for increased storminess. This period of bedrock scarp erosion and overwash and aggradational bed deposits building beach ridges associated with ice advance is followed by a period of ice-retreat and rejuvenated RSL fall, possibly initially at a higher rate, and continued progradation of beaches burying the bedrock scarp and abandoning the beach ridge. In the proposed model of raised beach formation, an ice advance before beach ridge formation and retreat after or during the time formation assigned to these stranded beaches would fit a scenario where beach ridge ages date the timing of continued ice retreat, GIA-induced Earth surface rebound, RSL fall, shoreline regression, and beach ridge abandonment stranding the raised beach ridges (Figs. 30 & 31).

#### **5.2.5. Timing of Scarps: Relationship to Known Ice Advances**

The formation of raised beach ridges of equivalent age and elevation controlled by GIA only works as an indicator of RSL in a region sensitive to surface loading events. The SSI provides this sensitivity allowing preservation of the RSL history that is resolvable from the noise of local influences. Previous work has identified evidence of Holocene glacial advances in the SSI (Sugden and John, 1973; Curl, 1980; Hall and Perry, 2004; Hall, 2007; Hall, 2009; Hall, 2010; Simms et al., 2012; Guglielmin et al., 2016; Yu et al., 2016, Chu et al., 2017). I find evidence for RSL oscillations during the formation of beach ridges 2, 4 and 5, and 9. The evidence for an advance during the time of beach ridge 2 formation ( $370 \pm 160$  cal yr B.P.) includes the work of Hall (2007) who used radiocarbon dating of mosses within moraines on Fildes Peninsula, KGI, to show that the most extensive advance of the Collins Ice Cap within the last  $\sim 3500$  cal years occurred after  $\sim 650$  cal yr B.P. Similarly, Yu et al. (2016) and Guglielmin et al (2016) both used moss adjacent to ice fronts near Palmer and



Rothera stations, respectively, and found evidence of ice advance 760 to 600 cal yr B.P. and between 671 to 317 cal yr B.P., respectively. Simms et al. (accepted) found evidence of an ice advance on Greenwich Island of the SSI within the last ~375 years. Simms et al. (2012) used OSL dating of cobbles from raised beaches and their stratigraphic relationship to moraines within Maxwell Bay, KGI, to date an ice advance between 450 and 250 cal yr B.P. Hall and Perry (2004) used the presence and concentration of ice rafted debris (IRD) and radiocarbon ages of stranded beach ridges 2 and 4 on the South Beaches, Byers Peninsula to infer cooler periods of glacial advance at 250 <sup>14</sup>C yr B.P. and 1750 <sup>14</sup>C yr B.P., respectively.

Evidence for an ice advance during the time of formation for beach ridges 4 and 5 (1790±189 cal yr B.P. and 1940±201 cal yr B.P.) from nearby Maxwell Bay, KGI is provided by Simms et al. (2011a) and Simms et al. (2011b). They used OSL dating of cobbles from raised beach ridges and ocean sediment cores to suggest ice retreat around 1.7 ka B.P. after an earlier advance. Locally, sediment cores from Domo Lake on Byers Peninsula were dated using <sup>14</sup>C, thermoluminescence, and tephrochronology. They determined the glacier front readvanced an unknown distance back over Domo Lake after 2.3±0.7 ka B.P. where it remained until at least 1.8 cal ka B.P. (Oliva et al., 2016). Chu et al. (2017) analyzed a 9.24 m sediment core from a fjord on Fildes Peninsula, KGI using <sup>14</sup>C, loss on ignition, grain size, magnetic susceptibility, and elements. Within this core evidence for a neoglacial advance is found between 2700 and 2000 cal yr B.P., at which point the core record ends. Hall and Perry (2004) used the increased IRD concentrations on beach ridges to suggest an ice advance and cooler conditions 1750 <sup>14</sup>C yr B.P. coincident with the timing of formation of stranded beach ridge 4 (1790±189 cal yr B.P.). Other proxy evidence from the AP supports widespread

cooling with glacial advances noted between 2.8 and 1.4 ka B.P. (Björck et al., 1996; Domack et al., 2002; Bentley et al., 2009; Michalchuk et al., 2009; Shevenell et al., 2011).

Hall (2009) cites ice advances on the AP and nearby islands that date to ~8.0-7.0 ka B.P. and ~5.5-4.5 ka B.P. using  $^{10}\text{Be}$  CRE dating of glacially polished bedrock. Palacios et al. (2020) uses  $^{36}\text{Cl}$  and  $^{10}\text{Be}$  CRE dating of erratic boulders ~150 m from the Rotch Dome ice front on beach ridges at a reported elevation of 10-12 m on Byers Peninsula, interpreting the ~4 ka B.P. age as the timing of a local ice advance. Hansom and Flint (1989) date marine shells of now locally extant species found within glacial till 0.4 m above the high-water mark and under a 10-15 m tall ice cliff on Brabant Island ~200 km SSW of Byers Peninsula. The reservoir-corrected ages suggest they were growing at ~5 ka B.P., which is interpreted to mean ice was at or near its present location before that time. The fresh nature of the shells suggests a neoglacial advance at ~5 ka B.P. In the same core from a fjord on Fildes Peninsula, KGI in which Chu et al. (2017) found evidence of a late neoglacial advance between 2700 and 2000 cal yr B.P., evidence for a period of minor cooling between 5800 and 4800 cal yr B.P. was found. If the beach ridge crest dates the timing of beach ridge abandonment before the last time of marine influence, then our calibrated and isobar correlated age assigned to beach 9 ( $5460 \pm 214$  cal yr B.P.) falls within the range of known ice advances ~5.8-4.0 cal ka B.P. The similarity in ages of beach ridges to the timing of known ice advances or cooler periods supports the GIA model response to ice loading. Glacial fluctuations are expected to impact the RSL of the SSI (Simms et al., 2012), which we observe in the stratigraphic succession of RSL fall and transgression associated facies.

#### **5.2.6. Marine Platform Erosion Rates**

I found cliff retreat rates of 5-10 cm/yr for Byers Peninsula bedrock scarps which are in the realm of cliff retreat rates from other studies. Rates as high as 2.5-5 cm/yr were reported in a similar environment to that of the SSI in Svalbard (Jahn, 1961). Mathews et al. (1986) measured cliff retreat in metamorphic rock in Sweden just south of the Arctic Circle yielding rates between 1.4 to 7.1 cm/yr. Moore and Griggs (2002) measured cliff erosion rates in the sedimentary beds comprising the sea cliffs in Monterey, CA to average 7-15 cm/yr with critical areas eroding at rates between 20-63 cm/yr with no influence from changes in lithology. Hansom (1983) found the terrestrial cliff retreat rates in the SSI from frost shattering alone to be 0.6-0.8 cm/yr using the volume of scree accumulation at the base of inland cliffs. These inland cliff retreat rates were calculated using the ages between beach ridges 1 and 2 on Byers Peninsula. However, there are shortcomings with application of the volume of scree as a measure of coastal cliff retreat in the study area. The erosion rates calculated by the volume of scree at a cliff base (Hansom, 1983) is inherently low due to the protection scree offers the cliff, coastal erosion reducing the volume of scree preserved, and marine retreat rates surpassing those of terrestrial cliff retreat rates (Strzelecki, 2011).

Estimated cliff retreat rates for the wave cut scarps beneath stranded beach ridges 9, 4 & 5, and 2 in my study area of 10 cm/yr, 5 cm/yr, and 7 cm/yr, respectively, (Table 8) are neither maximum nor minimum rates because of the uncertainty in how early retreat is initiated. The assumption was made that bedrock retreat and scarp formation initiates after ice advances and RSL fall slows (or begins to reverse). In my estimation this is immediately following deposition of the next highest elevation beach ridge on a bedrock scarp. However, the lower platform could undergo erosion by sea ice and icebergs (Nichols, 1961) during

erosion of the scarp immediately higher in elevation while still located below sea-level. This lowering could pre-date the age of the next highest scarp and beach-ridge succession, which would increase the maximum limiting age used in my estimation. Conversely, it is not known if scarp retreat initiates immediately after the abandonment of the beach deposited on the higher scarp. If not, initiation of bedrock scarp erosion could post-date the formation of the next highest stranded beach ridge. If erosion began after deposition of the next highest beach ridge a younger maximum limiting age for my estimation would be more appropriate. In either case the use of the age of the stranded beach ridge overlying the scarp as the lower limiting age is considered appropriate because of its stratigraphic position and the absence of evidence for reworking of the aggradational deposits. The distance between equivalent elevation stranded beach-ridges on beaches with initially steeper Early Holocene bedrock profiles may not require the estimated rates because the distances between bedrock scarps is smaller, thus requiring slower rates of retreat.

Marine cliff retreat rates vary across lithologies, energy of environment, temperatures, salt content, and ice processes. Cliffs from studies with low rates of cliff retreat in marine environments consist of more cohesive rock types than that of the marine shales, marine sandstone, and friable basaltic, dyke-intruded basaltic agglomerates and augite-andesites found on Byers Peninsula (Hobbs, 1968). Weatherability of coastal cliffs and marine platforms decreases with increasing distance from the shoreline in polar environments (Strzelecki, 2011). High degrees of fracturing further increase weatherability for the marine platform at the coastline (Fournier and Allard, 1992). Differential weathering causes variability in total weathering rates across the same lithologies (Chelli et al., 2010). Hansom

(1983) notes the erosive effectiveness of fast-ice free beaches in polar environments.

Processes such as freezing-on, quarrying by ice-impact, wetting and drying, and abrasion generate rapid erosion rates. Exposed coasts in the SSI experience fewer days/yr of fast ice and thus increased weathering of marine platforms compared to more sheltered coasts (Nichols, 1961).

### **5.2.7. Relating Fluctuations in RSL with Granulometry**

The availability of sediment in the proglacial environment is among the highest in the world (Ballantyne, 2002; Belknap, 2005). The role of ice and coarse sediment in marine platform abrasion is well documented in the region (Nichols, 1961; Hansom, 1983; Hansom and Flint, 1989). The model of beach ridge formation by Lindhorst and Schutter (2014) notes textural differences between strandplains and beach ridges. On Potter Peninsula, Maxwell Bay, the terrigenous source of sediment is cited as meltwater, tidewater glaciers, and ice rafted debris (IRD), but they offer no explanation for the mechanism causing textural variation between strandplains and beach ridges other than wave energy. Strandplains are finer grained and beach ridges contain coarser pebbles, cobbles, and boulders. I observed this textural trend within the sediment pits on the South Beaches (Figs, A2-A38 & Tables A1-A28) as did Theilen (2020) in her comparison of beach surface sediments on beach ridges 1 through 9 (Fig. 28).

Can the observed beach textures from granulometry studies (Theilen, 2020) and within sediment pits (this study) on the South Beaches aid in testing my model of GIA-induced RSL fluctuations? As glacial expansion occurs, the glacier front is closer in proximity to the modern beach (Palacios et al., 2020). This proximity allows glaciers to transport larger clasts

from inland marine platforms to the active beach where they are rounded and incorporated into beach ridges. Increasing wave energy is enabled due to the increased water depth afforded by RSL rise, which increases the efficiency of the beach system to round clasts and winnow fine sediment from the shoreface (Fig. 28). This might explain, the larger and better-rounded clasts observed within beach ridges compared to the more angular and finer sediments observed within strandplains on the South Beaches (Fig. A2-A38 and Fig. 28) and similar textural changes observed on Potter Peninsula (Lindhorst and Schutter, 2014). The sensitivity of the SSI to ice loading and observed sedimentary textures on the South Beaches suggests a unique selection for sediment delivery to the active beach whereby glacial advance causes GIA-induced land depression and subsequent RSL rise. The glacial coarse sediment source advances seaward and the active beach transgresses inland, closing the distance between source and sink. Glacial advance decreases the outwash ratio of fine to large sediment sizes. This observed increase in coarse sediment fraction accompanying glacial advances provides abrasive tools for bedrock erosion near the time the shoreline transgressed to the location of the now-preserved stranded beach ridges. As RSL rises and larger waves break on the active shoreline, sediment of the previously deposited prograding strandplain deposits are rounded and reworked into larger beach ridges. With glacial retreat there is associated GIA-induced land rebound and subsequent RSL fall. The glacial coarse sediment source retreats inland and the active shoreline regresses seaward, separating source from sink. However, as glaciers retreat, meltwater outwash will increase the proportion of fine sediment delivered to the active beach via fluvial channels, which were observed on the east end of the South Beaches near the terminus of Rotch Dome Glacier, which is actively retreating in response to RRR (Fig. 29). These fluvial channels are capable of transporting

fine-grained sediment across the beach and may even simultaneously increase the proportion of fine-grained material with glacial retreat and RSL fall as the coarse fraction delivered decreases (Fig. 10 - stream & Fig. 28 - glacial outwash). Concurrent with selection for finer sediment, during RSL fall depths offshore decrease which inhibit the efficiency of waves to break onshore. Less efficient wave energy at the coast following RSL fall results in a finer grained active shore face which is characteristic of the strandplain. The observed trend of changes in sedimentary texture on the South Beaches (Theilen, 2020) and known ages of neoglacial advances aligns with this model of sediment delivery.

#### **5.2.8. Other Geomorphic Evidence Supporting the Model**

Geomorphic evidence for scarp formation following the local LGM was originally misinterpreted to pre-date the LGM before oscillations in the ice front following the LGM were considered. Evidence includes the presence of the 3-8 m platform located within glacial troughs and the 11-17 m platform dissecting meltwater channels originating from the 28-50 m platform (John and Sugden, 1971). The absence of shore-normal striations within the 11-17 m platform and their high concentration on the offshore platforms below sea-level (John and Sugden, 1971; Curl, 1980) could be explained by our scarp model. Scarp retreat through the 11-17 m platform during early Holocene RSL rise leading to scarp formation beneath stranded beach ridge 9 could have removed glacial striations or sea-ice abrasion giving it a fresh surface. Subsequent preservation of the surface was provided by RSL fall raising the beach from marine influence and protecting it with beach deposits. Striations within the marine platforms below sea level likely formed during the LGM and have yet to be erased by scarp retreat as they now lie below the elevation of scarp formation. Hansom and Kirk (1989) noted the fresh nature of the scarps and how they were ‘well suited to their morphogenic

environment' likely caused by frost weathering and ice push. Rotch Dome Glacier overrides all platforms and scarps above sea-level and below the 28-50 m platform on Livingston Island. Considering oscillations of the icefront, this superposition could alternatively be explained by the ice front terminating landward of its present terminus far enough for scarp erosion during warm periods in the Holocene and afterwards readvancing during Holocene glacial advances, as is shown to have happened on nearby Maxwell Bay, KGI (Simms et al., 2012). The congruence in shape of the Holocene beaches with the modern shoreline provides further support that wave action is eroding and trimming the bedrock front of the scarps. It is unlikely that the younger beach ridges, which are independently dated to coincide with neoglacial advances, form at the same elevations as previously cut scarps unless they share a common genetic relationship.

The transgression that may have initially removed any remnant glacial or IRD scouring of the 11-17 m marine platform may be recorded in the sediment architecture landward of beach ridge 9. Little variation in the thickness of beach deposits was observed across the South Beaches, with beach surface topography closely matching that of the underlying bedrock. Progradation of the beach is observed across all regions of the strandplain with the beach ridges being the only preserved transgressive features. The lack of vertical aggradation in progradational beach deposits on a coastline with perceived adequate sediment supply suggests a forced regression of the shoreline as the driver of progradation, as would be expected during continued fall in RSL. With sediment supply held constant, vertical aggradation of a prograding deposit would only occur with rising sea level or with a sea-level standstill. Vertical aggradation of prograding beach deposits is only observed at one location



on the South Beaches. This vertical aggradation was observed within GPR profile 34 landward of beach ridge 9 (Figs. 24 and 25). Landward of beach 9 multiple packages of stacked rf-s are observed prograding seaward up a bedrock ramp that dips landward. This architecture is interpreted as a normal regression as sea-level rise has not outpaced sediment supply. The location of this succession landward of stranded beach ridge 9 is suggestive of possible deposition during rising sea-levels during the Early Holocene when global eustatic sea-level rise outpaced GIA-induced uplift or during local RSL rise induced by an early neoglacial advance between ~8.0 and 7.0 ka B.P (Palacios et al., 2020). Vertical aggradation of post beach-formation infilling of accommodation on the South Beaches within the lagoonal and fluvial sediments does occur but is not indicative of wave action.

I argue that bedrock retreat is temporally related with deposition of the Holocene beaches and provides a mechanism for preservation of stranded beach ridge architecture. In similar studies of raised beaches on Potter Peninsula, Maxwell Bay, KGI, bedrock support under prominent stranded beach ridges is not discussed despite every published line showing bedrock scarp support (Lindhorst and Schutter, 2014; Barión et al., 2019). Lindhorst and Schutter (2014) measured three beaches with varying beach orientation and exposure to storm wave impact. Stranding of beach ridges and their subsequent preservation above a scarp is observed across all three areas of the study. They do not consider the underlying onshore bedrock topography as a control on stranded beach preservation and prominence. It would be unlikely that equi-elevation beach ridges formed with varying wave exposure and days of fast ice across an entire island chain without some preservational control. The lack of prominent, but still elevation correlative, stranded beach ridges on more sheltered coasts may

be due to the absence of adequate wave energy and/or coarse sediment sufficient to erode bedrock due to persistence of fast ice (Nichols, 1961). The slope of the marine platform or bedrock underlying beach deposits controls strandplain progradation rates. The faster a strandplain progrades, the higher the storm recurrence interval needed to erode into the strandplain sheltering the landward beach ridge from wave energy. For a given unit of RSL fall, a beach with a flatter underlying profile will prograde a greater lateral distance compared to that of a beach with a steeper underlying profile. It follows that lower profile marine platforms hosting beaches would better preserve these beach ridges than steeper marine platforms with falling sea-level and sediment supply held constant across both beaches.

### **5.3. Implications for the RSL of the SSI**

Weak Earth structure within the SSI has previously been attributed to the tectonic and volcanic setting of the islands (Taylor et al., 2008; Watcham, 2011; Simms et al., 2012; Nield et al., 2014). This weak structure results in heightened sensitivity to surface loading compared to more tectonically stable or cratonic areas. The RSL response to local ice-mass loading suggested in this study supports this notion of sensitivity to Holocene advances. RSL reconstructions in this region assume that the recent uplift reflects GIA from the LGM (Bentley et al., 2005; Roberts et al., 2011). Our study supports assertions that Holocene ice-mass loading may be masking LGM rebound (Simms et al., 2012; Simms et al., 2018; Zurbuchen and Simms, 2019). Thus, any conclusions on the volume of ice over the SSI and AP during the LGM based on RSL may be biased if not corrected for these late-Holocene glacial oscillations.

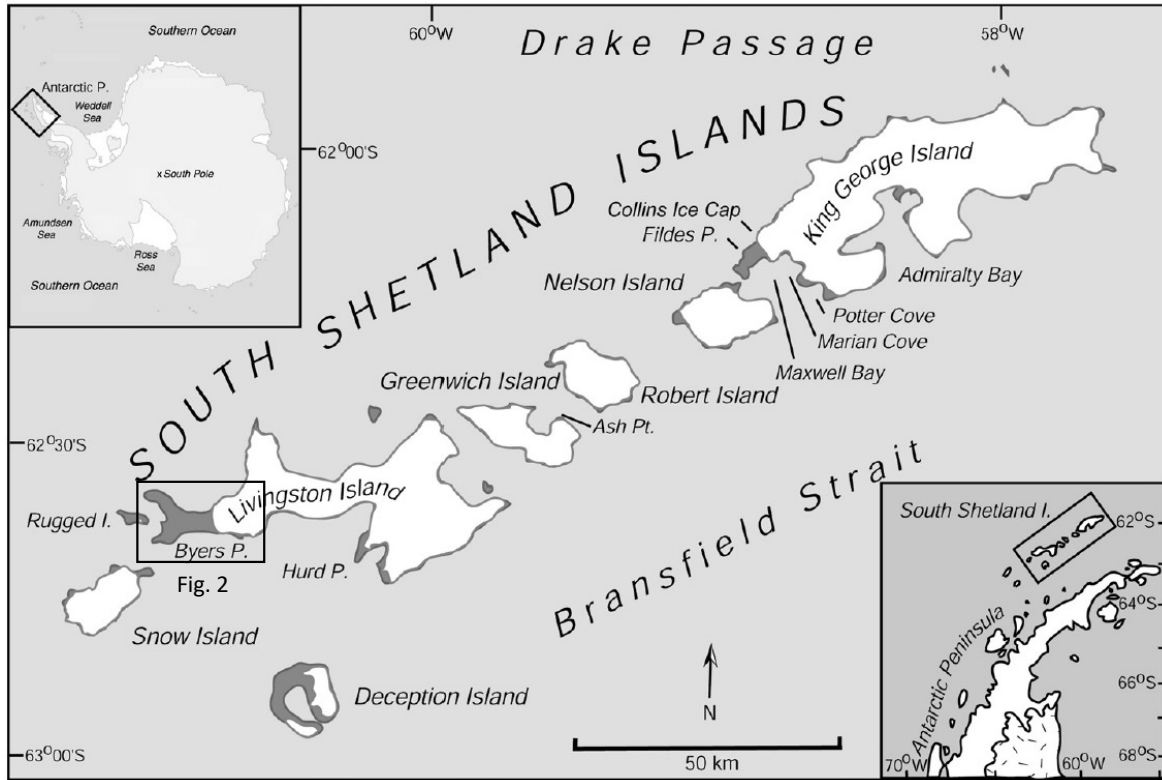
## **6. Conclusion**

To examine the RSL history contained within raised beach deposits of the South Shetland Islands, I collected over 10 km of GPR profiles on the South Beaches of Byers Peninsula, Livingston Island. I analyzed profiles and identified six key radar facies and three surfaces. Radar facies were identified as seaward dipping progradational deposits (rf-s), landward dipping overwash deposits (rf-l), and flat and concave-down aggradational wave overtopping deposits (rf-ag). Additional radar facies are interpreted as a discontinuous reflection configuration of a cobble dense layer, often lying on bedrock (rf-d), lagoon facies deposited behind the active beach and connected to the ocean via tidal inlets (rf-f), and fluvial deposits observed on the Holocene beaches and linked to gullies incising the seaward edge of the 28-50 m platform (rf-c). Radar surfaces identified include an erosional truncation surface (s1-e), the top of the bedrock, which lacked reflections below and was often covered in cobbles, likely causing ringing hyperbola reflections (s2-b), and a deflation pavement surface (s4-tl) located primarily above rf-s. A repeated succession of facies and surfaces was observed beneath stranded beach ridges. This succession of reflections consisted of a seaward step down in the bedrock overlain by progradational beach deposits (rf-s), in turn overlain by overwash and aggradational beds (rf-l and rf-ag). This succession was observed across scarps beneath stranded beach ridges 9, 4 & 5, and 2. Coincidentally, each of the assigned ages of these beach ridges corresponds to a known glacial advance in the SSI.

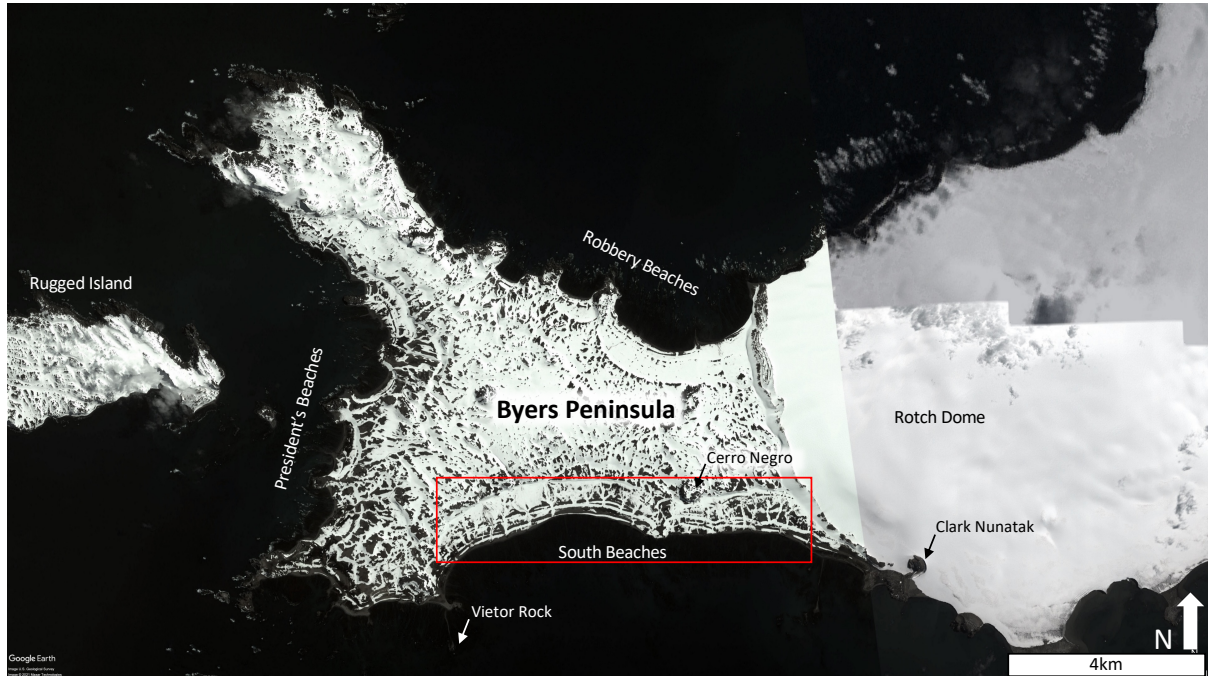
I interpret the succession of surfaces and deposits beneath the stranded beach ridges as representing high-frequency oscillations in RSL driven by the GIA response to local ice advances and retreats during the Holocene. Beaches prograded during RSL fall. Subsequent glacial readvances caused GIA depression of the Earth's surface causing RSL rise and the

erosion of the shoreline producing the scarps. This RSL rise also increased the ability of waves to build and break closer to the shore, resulting in overwash deposition. The beaches are preserved on the related eroded scarps. Coarse clastic beach sediments aided this bedrock erosion and are preserved within the stranded beach ridges formed during this transgression in sea level. This process repeats itself at each ice advance that causes a decrease in the rate of RSL fall or causes RSL rise, producing the flight of raised and stranded beaches observed throughout the SSI.

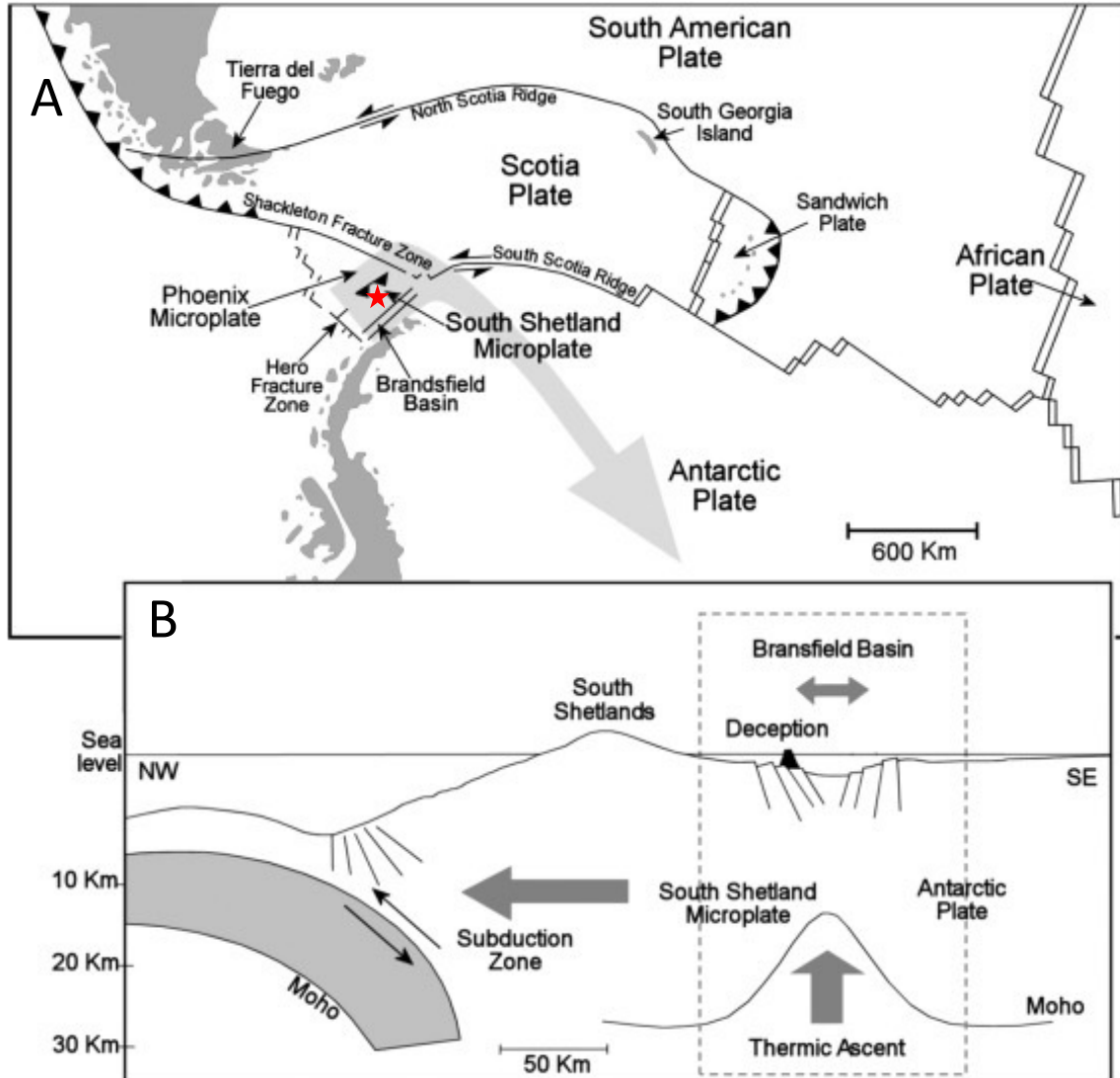
This study further supports assertions of GIA-induced Holocene transgressions within the SSI during a period of overall RSL fall. The sensitivity to local or regional ice-mass fluctuations recorded in the beach stratigraphy indicates that RSL curves from this region should be applied with caution to larger scale GIA models and predictions of ice-mass loss following the LGM.



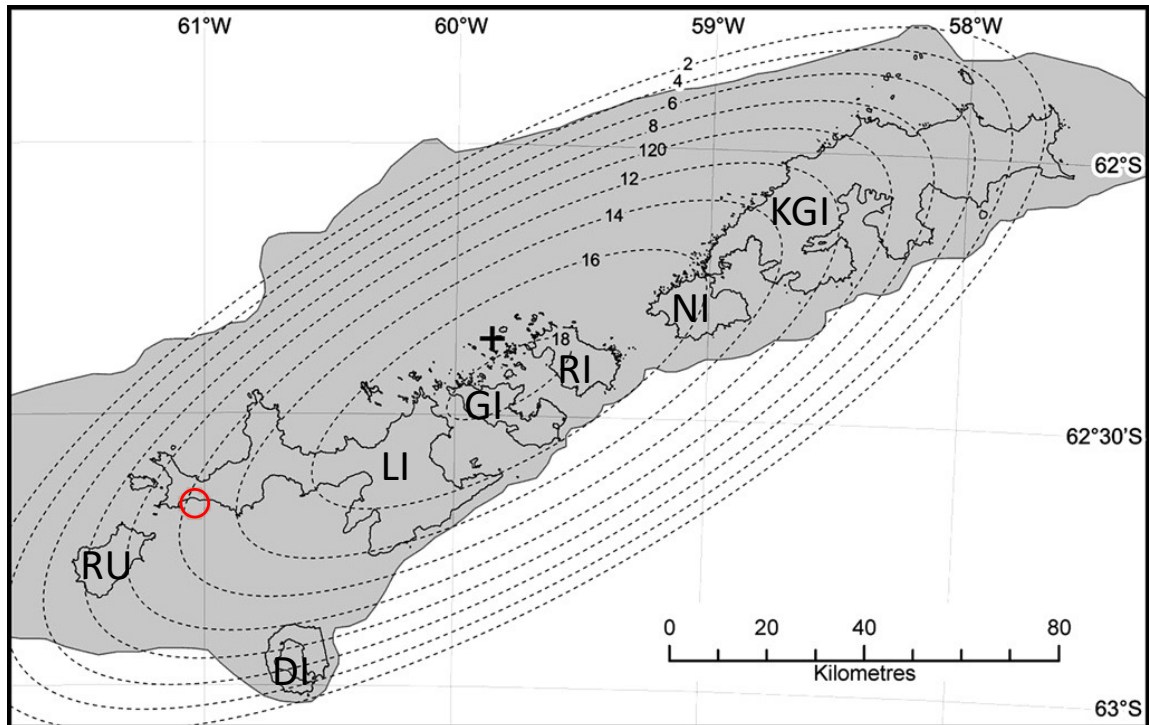
**Figure 1:** Map illustrating the geographic location of the study area northwest of the Antarctic Peninsula. Inset for Figure 2 shows the study area of Byers Peninsula, Livingston Island. (Hall, 2010)



**Figure 2:** Aerial photograph of Byers Peninsula, Livingston Island. The South Beaches study area is boxed in red. Other features noted in text labeled for geographic reference. See Fig. 1 for general location (Google Earth Imagery)

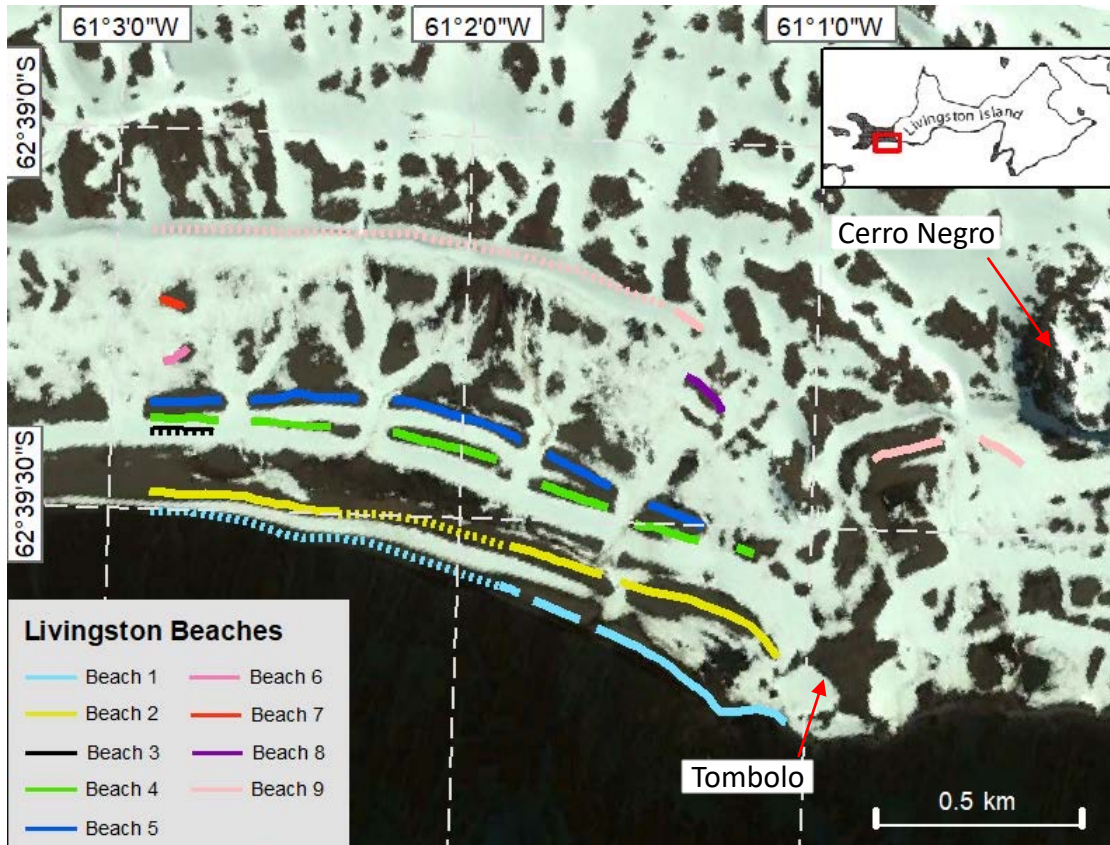


**Figure 3: Panel A.** plate tectonic map and relative plate motions. The approximate study area location is identified with a red star. **Panel B.** Cross-section of the Phoenix Plate subducting under the South Shetland Microplate illustrating the back-arc opening of the Bransfield Basin located between the SSI and the AP. (Berrocoso et al., 2016)



**Figure 4:** Isobar modeled map of the elevation of the highest raised beaches suggesting the center of ice loading was on or near Greenwich Island. Study area identified with open red circle. Elevations are measured in meters above present-day beach. Area shaded in grey is the proposed ice extent at the Last Glacial Maximum (by John and Sugden, 1971). LI=Livingston Island, GI=Greenwich Island, KGI=King George Island, Di=Deception Island, RU=Rugged Island, RI=Robert Island, NI=Nelson Island (map modified from Fretwell et al., 2010).



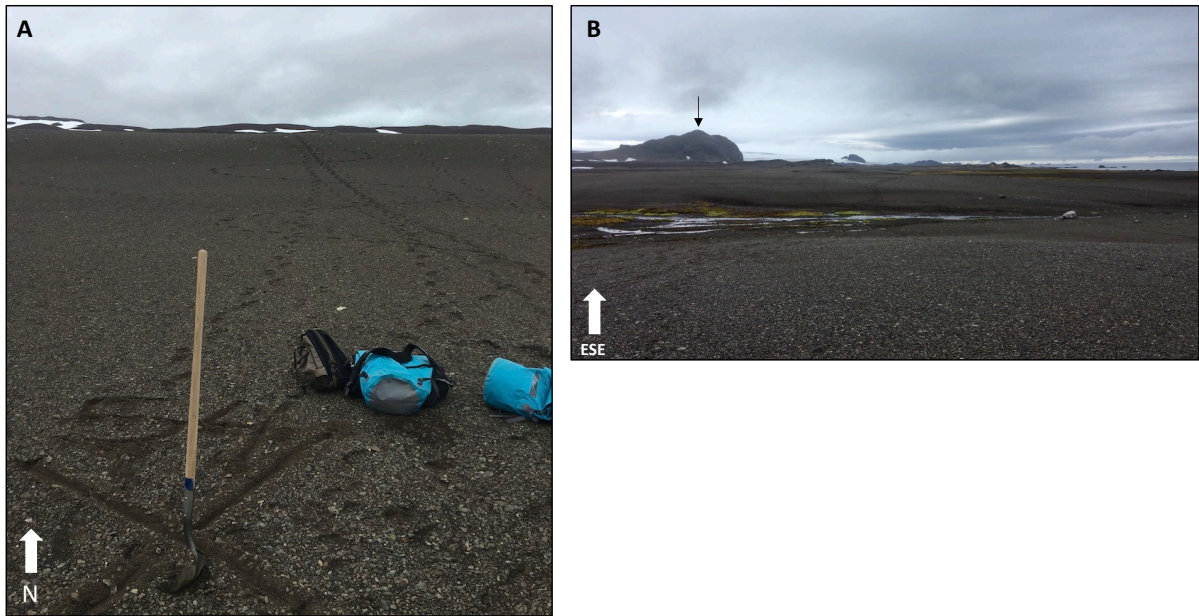


**Figure 5:** Map of Livingston Island beaches. Solid lines indicate GPS surveyed beaches and dotted lines indicate projected beach locations. The Holocene marine limit and seaward edge of the 28-50 m platform is north of beach ridge 9 (Theilen et al., 2020).

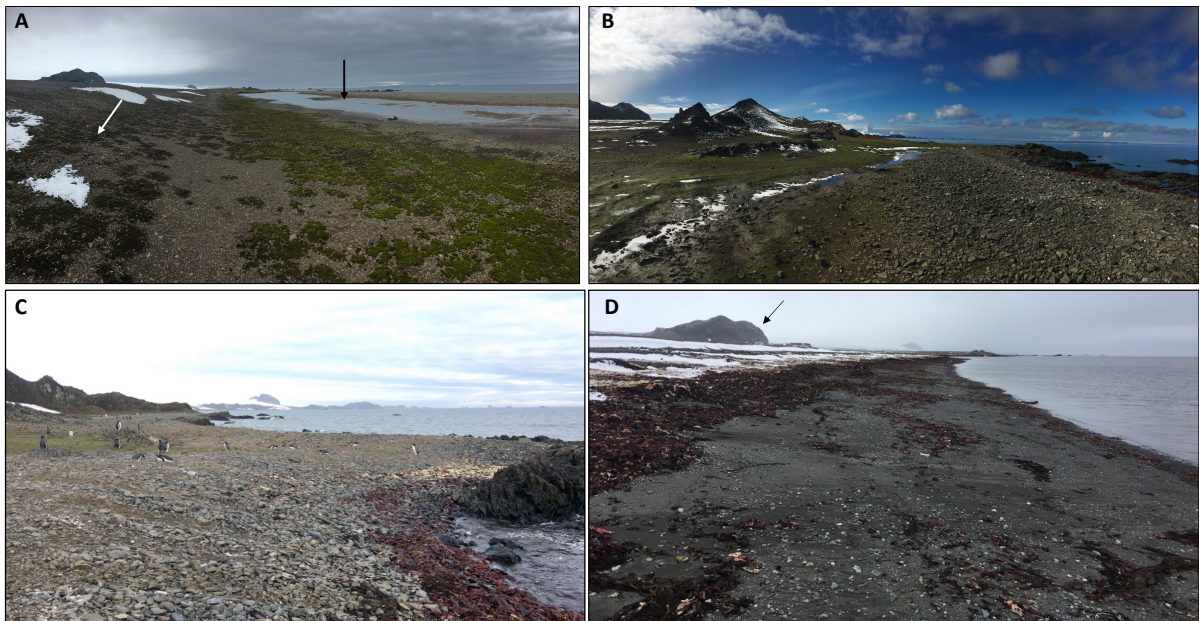


**Figure 6:** Photograph looking towards the west of the South Beaches, Byers Peninsula, Livingston Island, South Shetland Islands from ~500 m west of Cerro Negro. Approximate locations of beaches identified with green lines. Beach ridges 1, 2, 4, 5, and 9 in solid lines. Beach ridges 3, 6, 7, and 8 are dashed lines. Black arrow identifies Viotor Rock on the west end of the South Beaches.

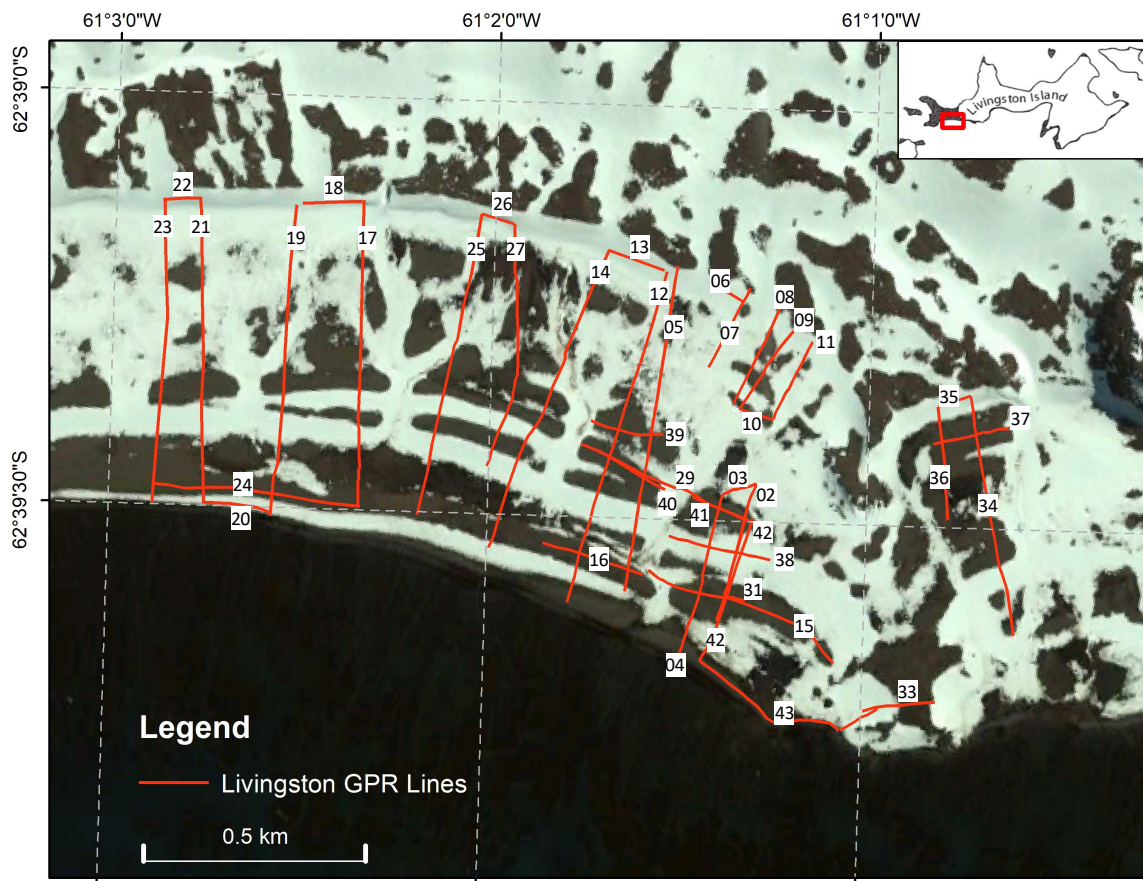




**Figure 7:** **A.** Photograph looking inland and to the north up the seaward slope of beach ridge 4. **B.** Photograph looking to the east across study area along the crest of beach ridge 4. Note the channel incision through the beach in the foreground. Cerro Negro is in the background indicated with a black arrow.

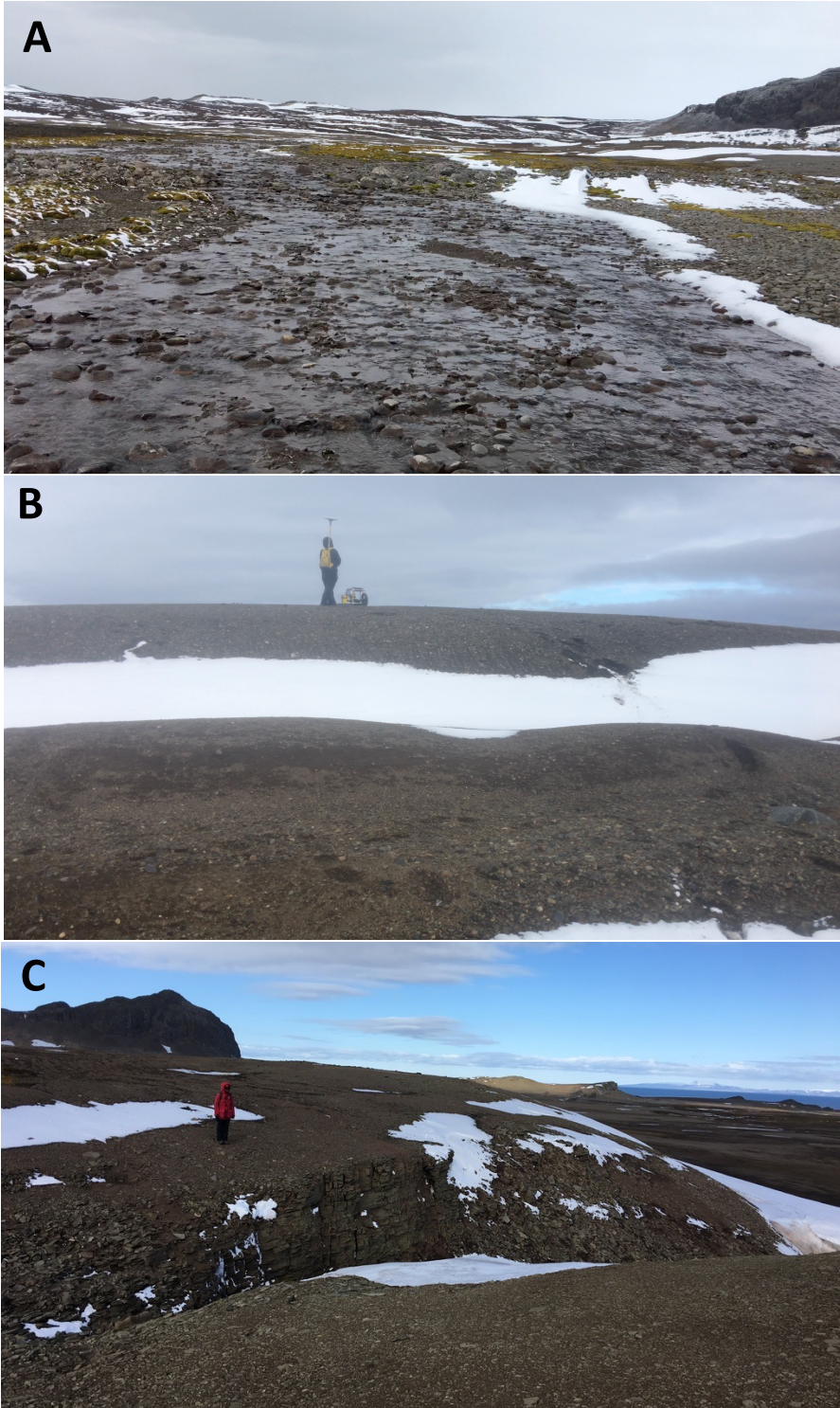


**Figure 8:** **A.** Photograph of the modern beach from the bottom of the seaward slope of beach ridge 2 on left side of image (indicated with white arrow) looking east across the South beaches. Black arrow indicates lagoon behind beach ridge 1. **B.** eastward view along modern beach 1. Marine platform at sea level exposed to right of the image. Paleo sea-stacks and tombolo to the left of the image in the background. **C. and D.** show variations in coarseness of the modern beach ridge 1 looking east along strike. Black arrow in panel D indicates Cerro Negro. Gentoo penguins for scale in panel C. (~40 cm).

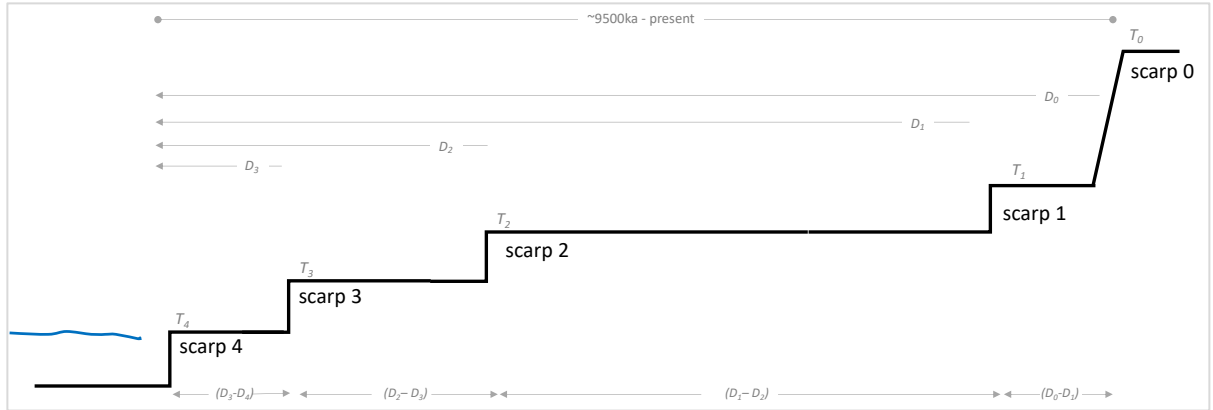


**Figure 9:** Map of GPR transects collected on the South Beaches, Byers Peninsula. (Modified from Theilen et al., 2020)

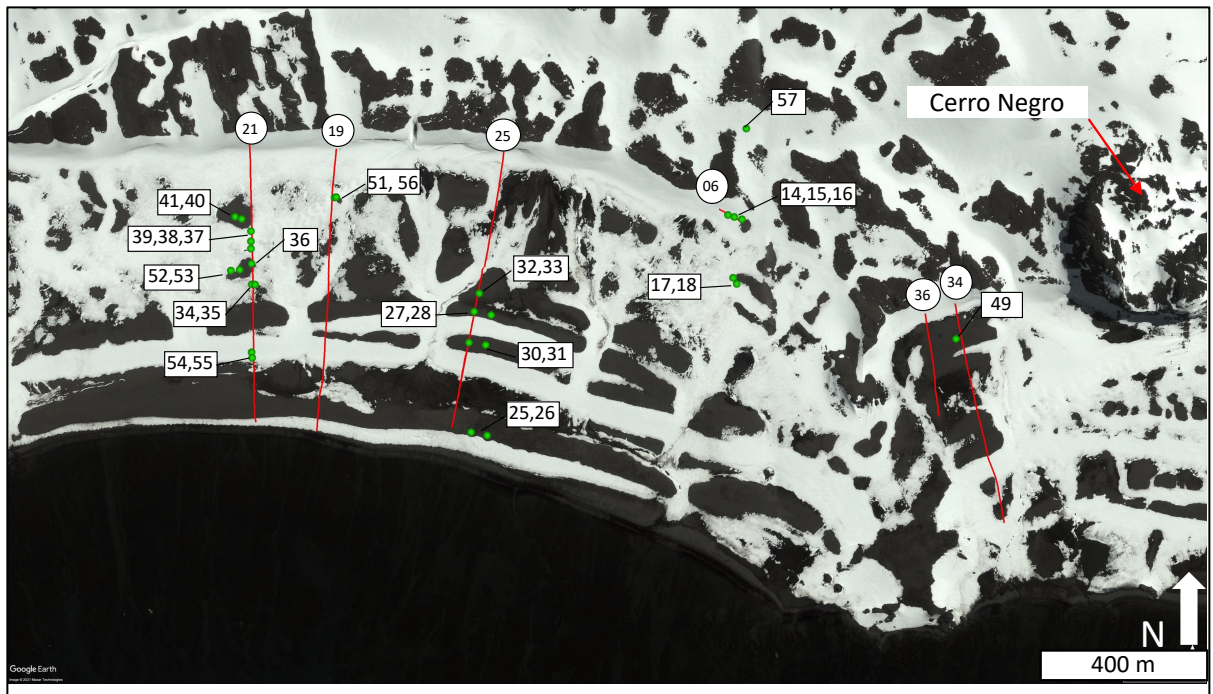




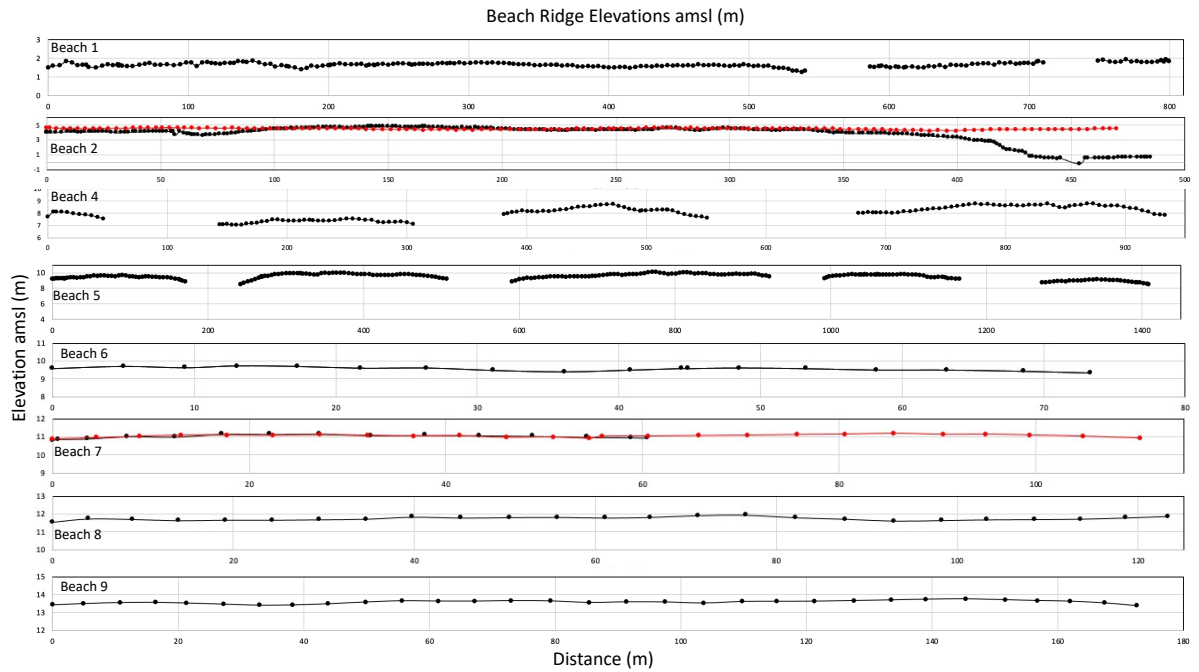
**Figure 10:** **A.** Photograph looking north from ~beach ridge 4 along a coarse stream bed dissecting the beach. **B.** Photograph looking south to the crest of a beach ridge within stream bed running parallel with the coast. **C.** Photograph looking ~east from edge of the 28-50 m platform backing the Holocene beaches. Gully is typical of those feeding streams dissecting the lower beaches.



**Figure 11:** Schematic for Eq. 2  $[(D_n - D_{n+1}) / (T_{n-1} - T_n) = \text{EROSION RATE (M/YR)}]$  for the bedrock erosion rates of Holocene marine platforms. D=distance, T=beach ridge formation age,  $T_0$ =Holocene marine limit

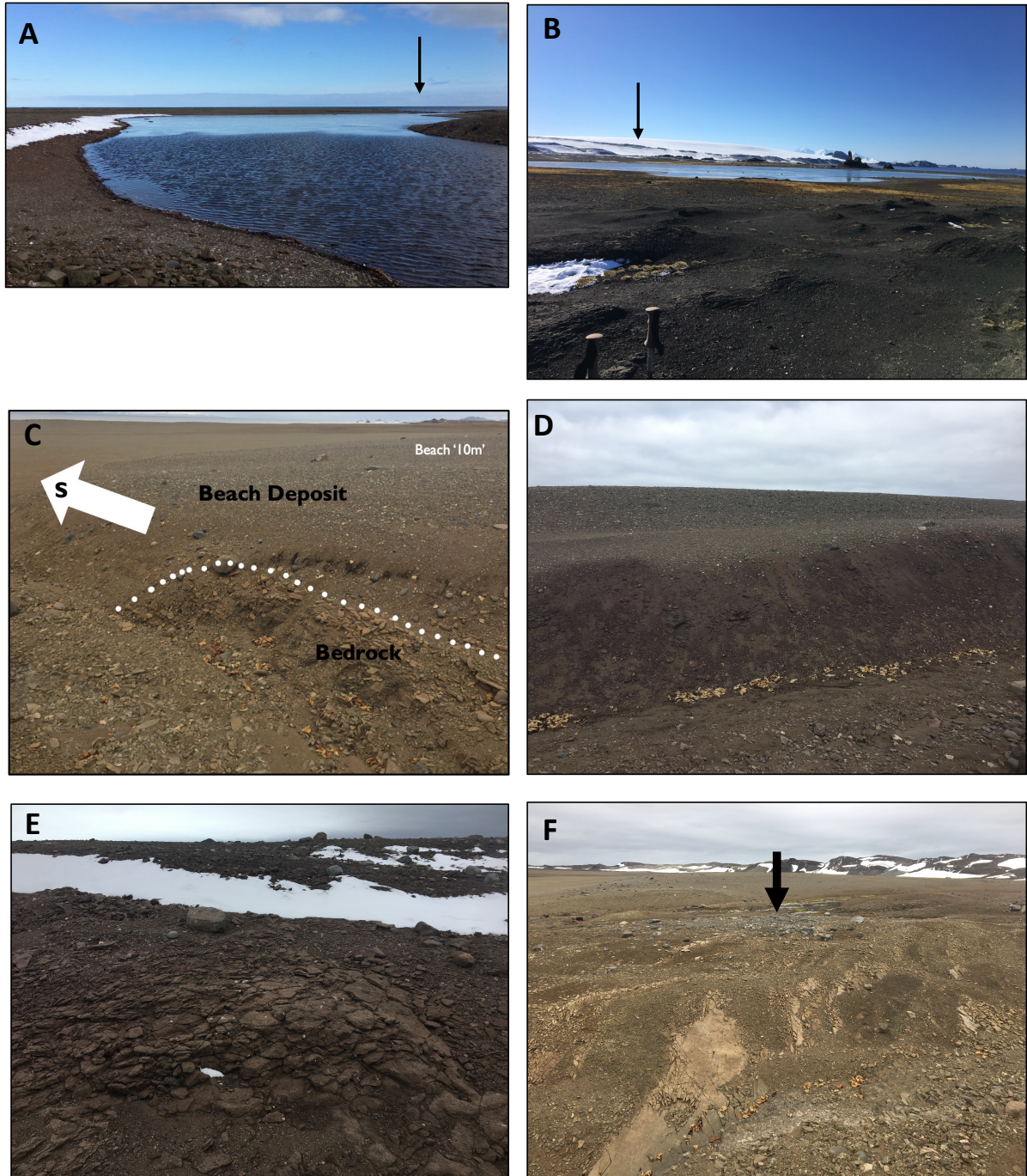


**Figure 12:** Map of sediment pit locations indicated by green circles and labeled with squares by pit number (XX) following the LV19-XX naming scheme. Nearby GPR lines indicated by red lines and numbered with circles.



**Figure 13:** Plot of South Beaches beach ridge crest elevations collected from kinematic GPS surveys. Beaches with multiples surveys use additional red line (beach ridges 2 and 7).

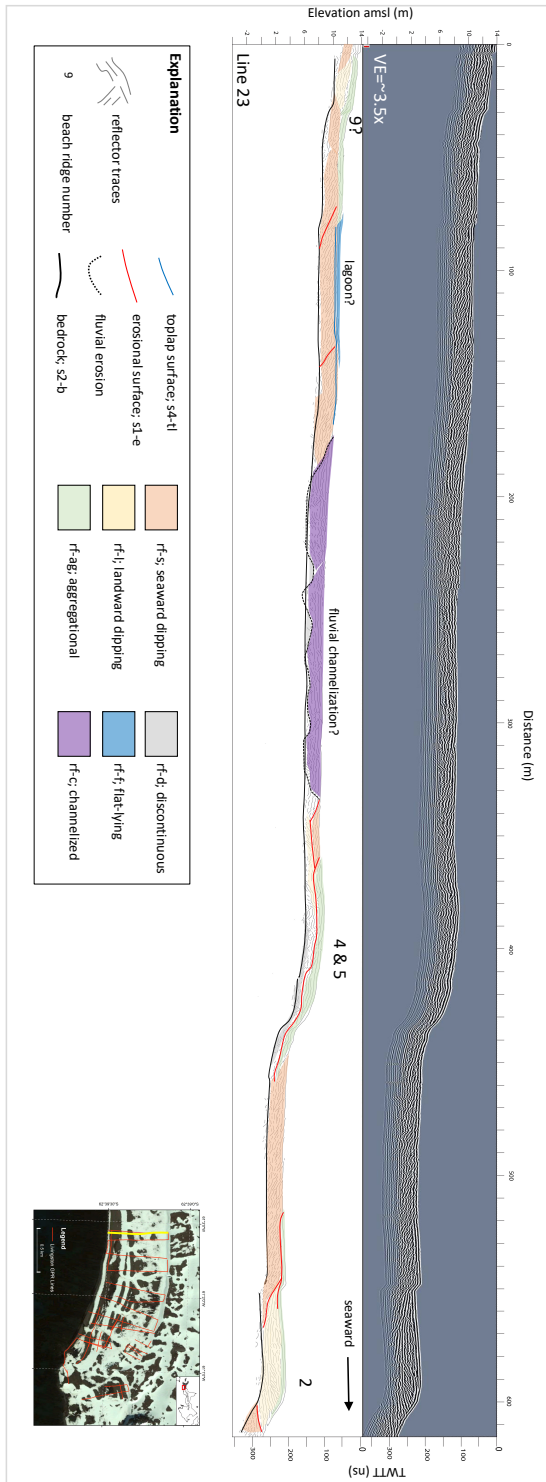




**Figure 14:** **A.** Photograph looking south from beach ridge 2 across a lagoon connected to the ocean through a tidal inlet denoted by a black arrow. **B.** Photograph looking east from tombolo across the eastern side of the South Beaches. Lagoons and meltwater lakes fill the landscape with Rotch Dome in the background denoted by a black arrow. **C – F** contain observations of the bedrock outcropping used to ground truth GPR profiles. **C.** Bedrock scarp shown with overlying beach ridge 4 deposits. Contact is identified with a dotted white line. **D.** Bedrock outcropping on the landward flank of beach ridge 2. **E.** Bedrock outcropping within a stream cut of beach ridges 4 and 5. **F.** Outcropping bedrock in area heavily modified by fluvial processes. Active stream channel identified with black arrow.



**Figure 15**



**Figures 15 - 26:** Shore normal GPR transects. Top panel displays topographically corrected and processed GPR lines. Bottom panel displays reflection traces and interpreted radar facies and surfaces. Beach progradation is occurring from landward to seaward. Seaward direction is noted on each line with a black arrow. Beach ridges are numbered. Interpreted regions of lagoon, fluvial, and cliff scree are noted in GPR traces. Each GPR line figure contains a map with the interpreted line highlighted in yellow.

Figure 16

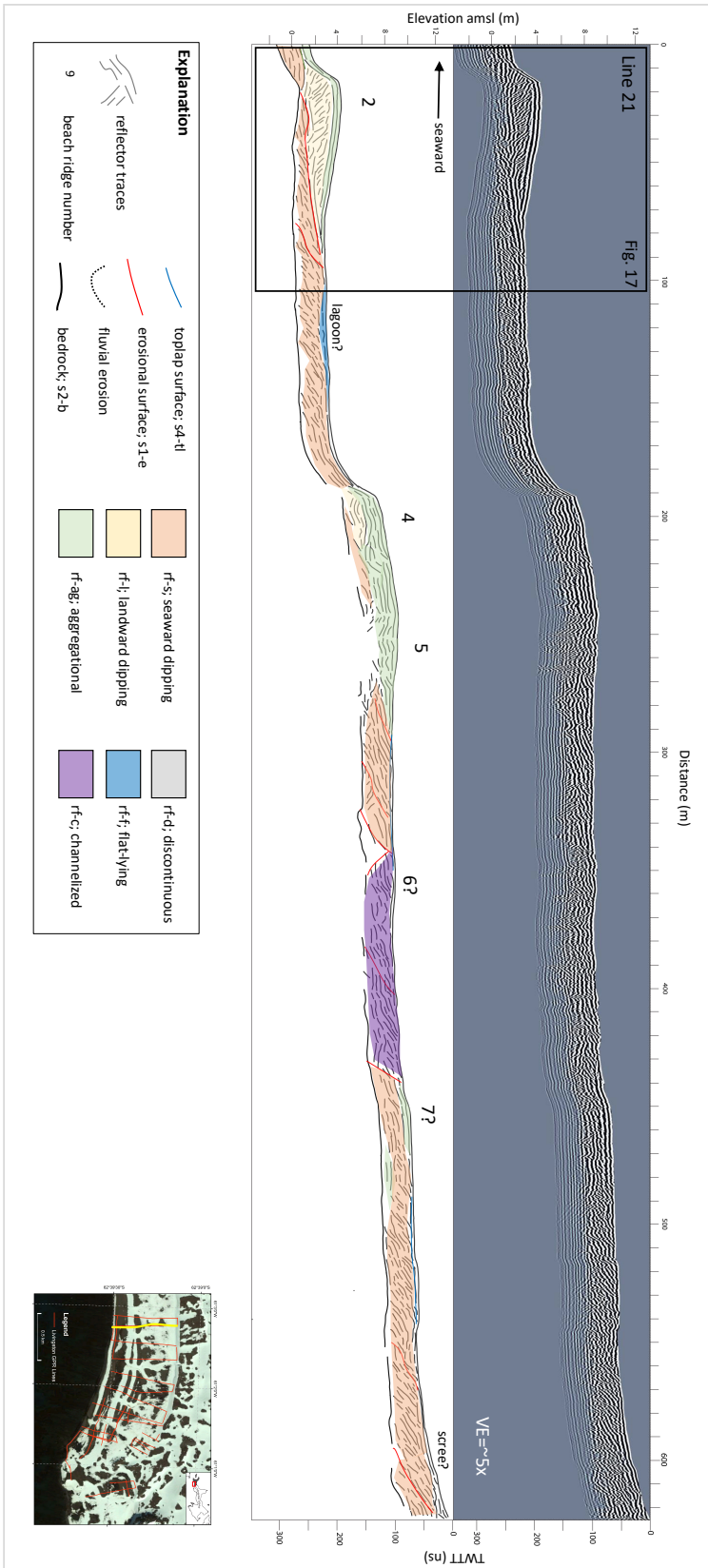


Figure 17

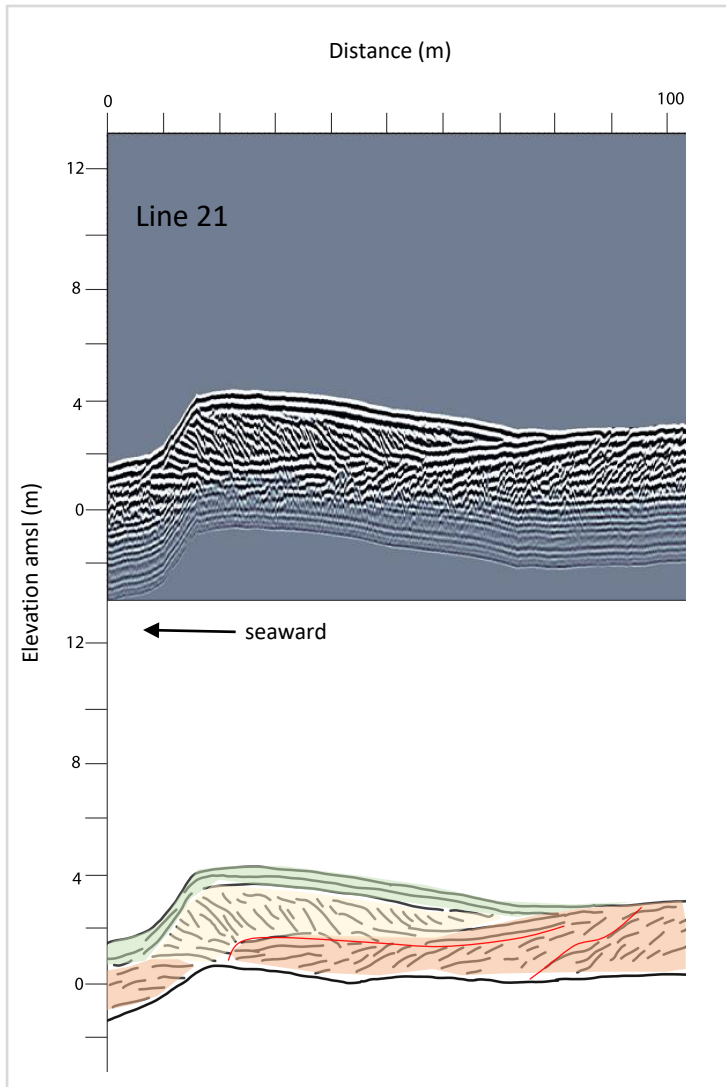


Figure 18

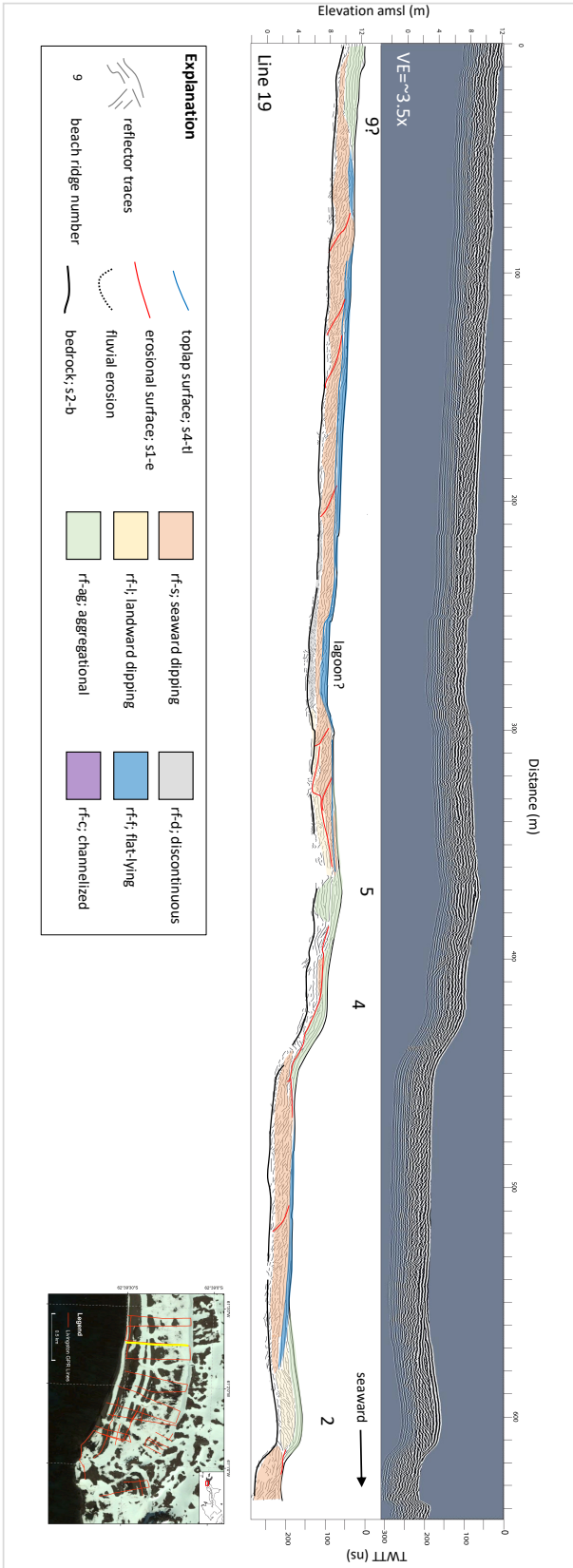


Figure 19

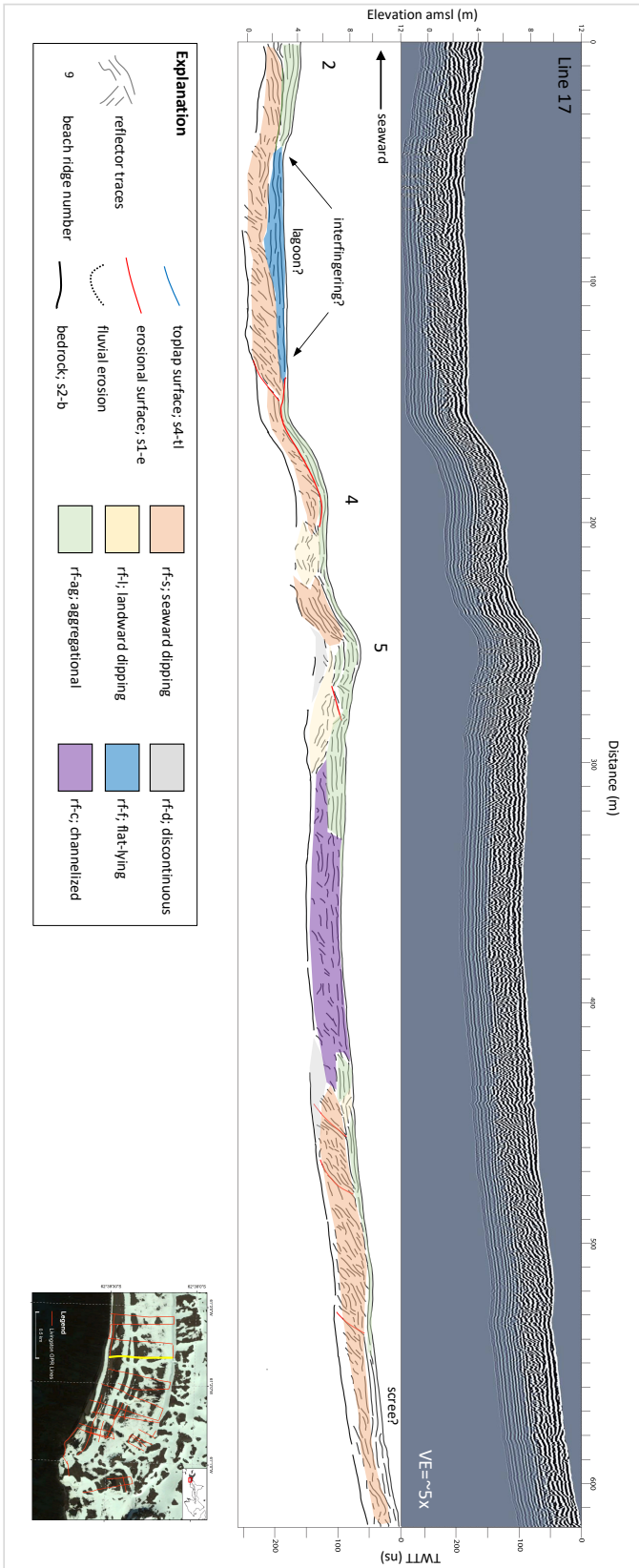


Figure 20

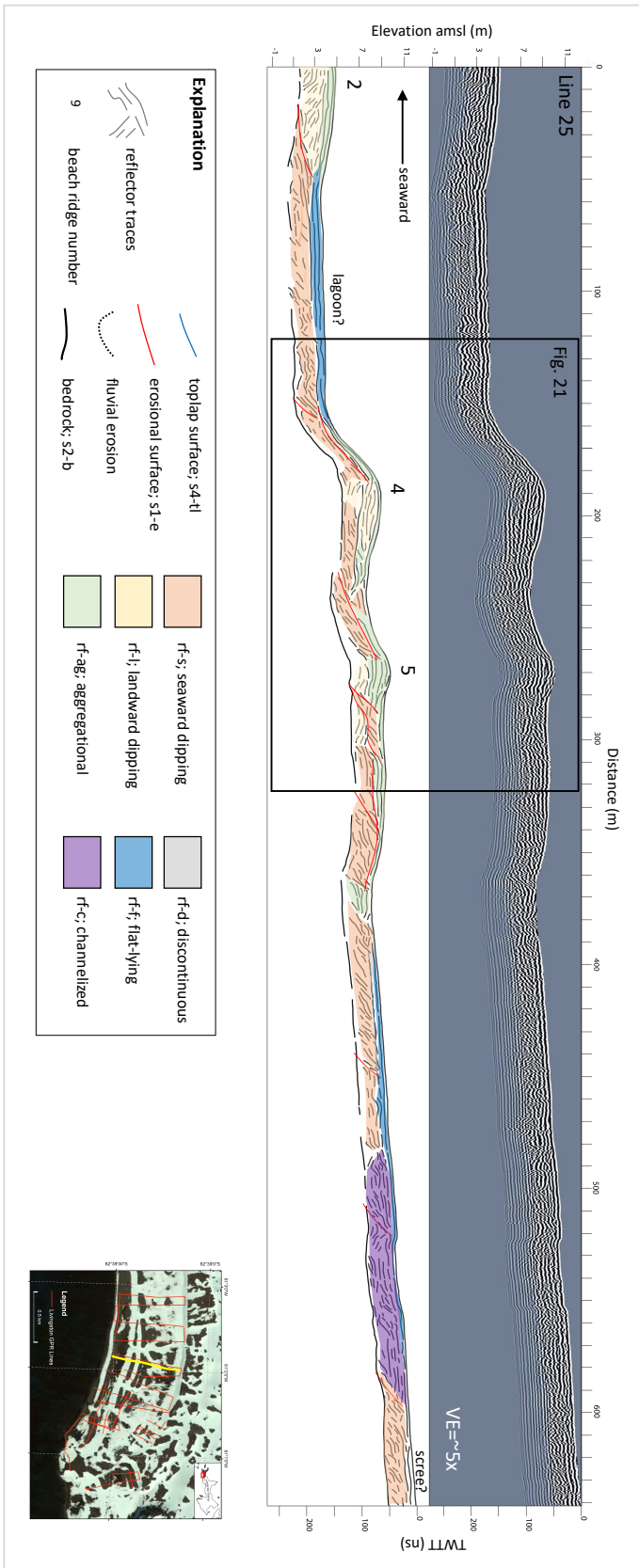


Figure 21

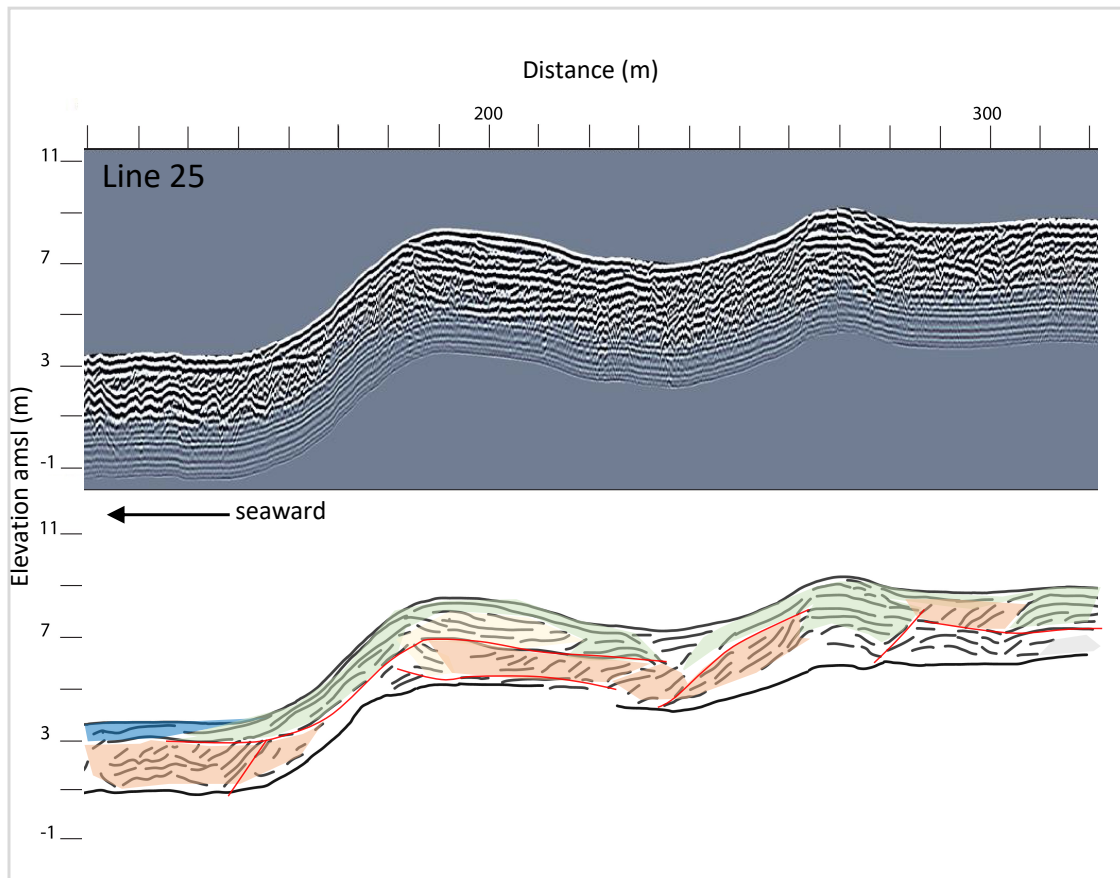




Figure 22

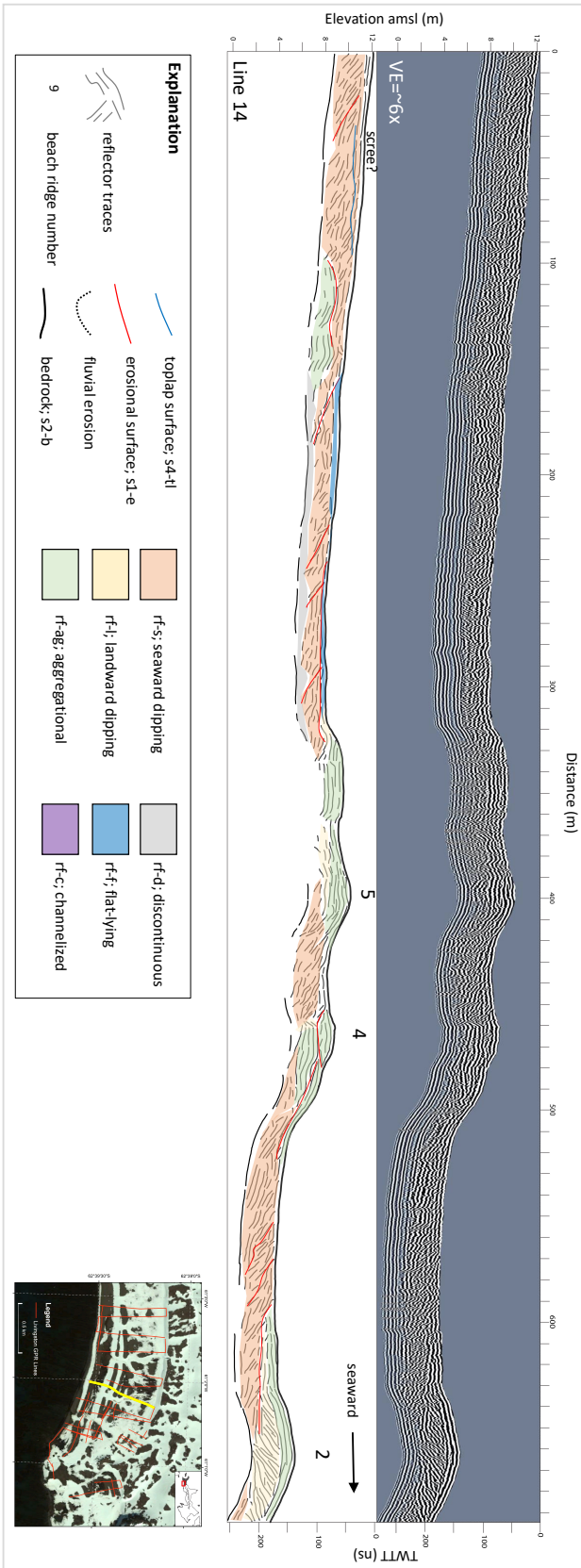




Figure 23

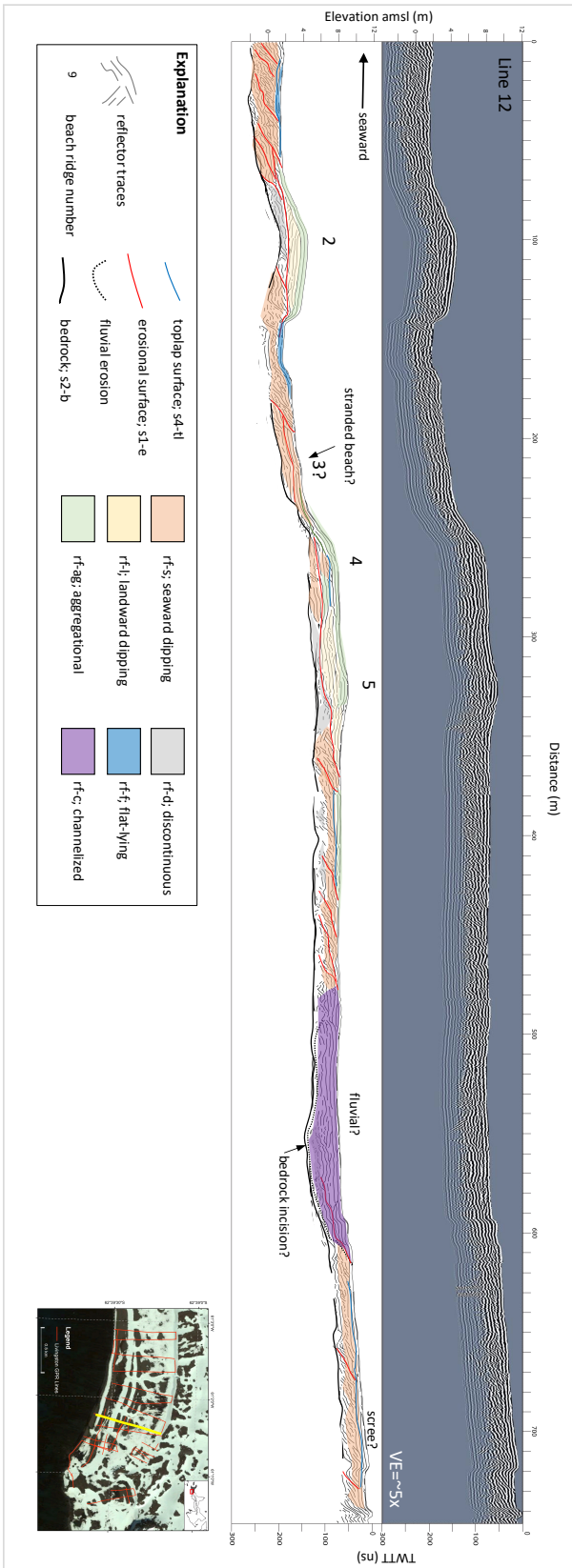
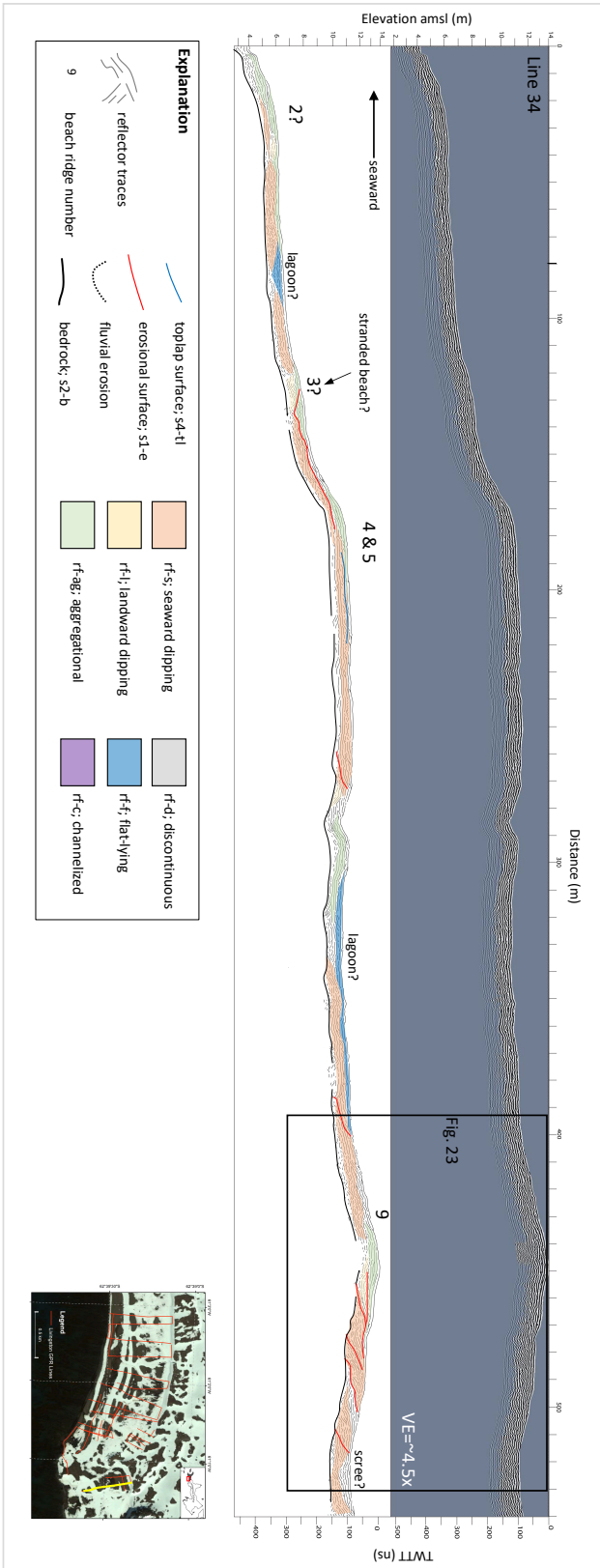


Figure 24



**Figure 25**

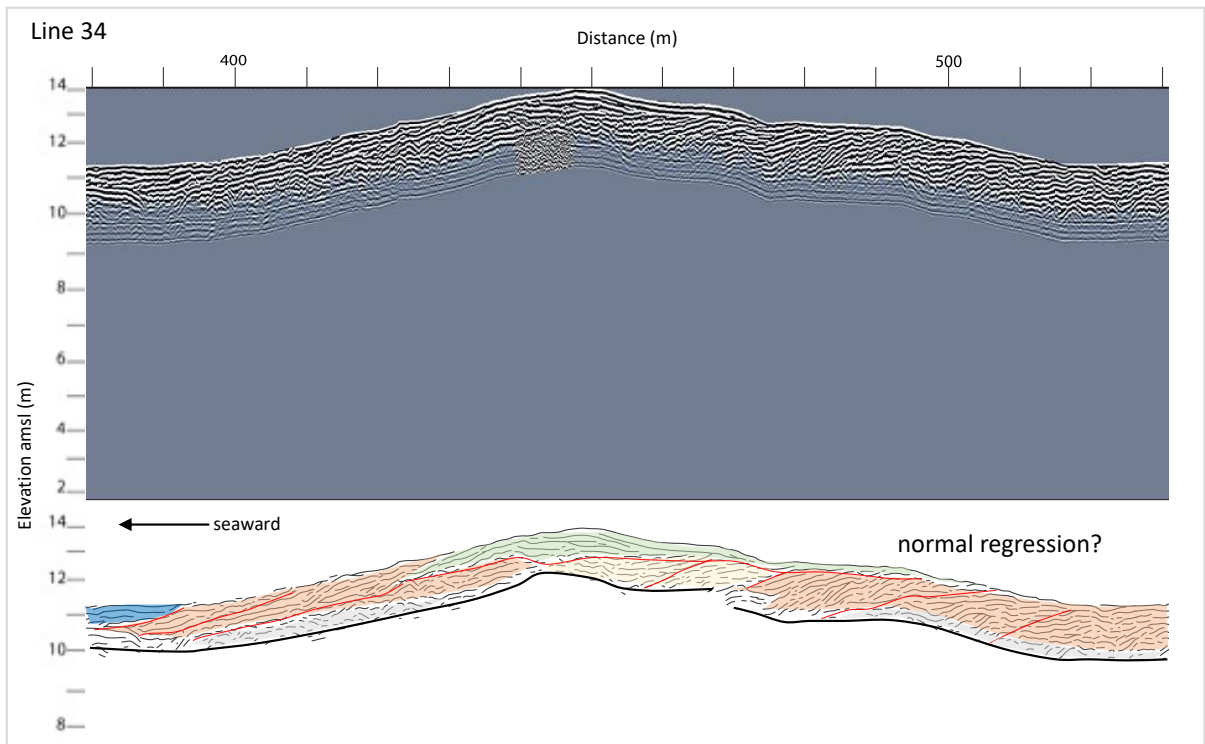
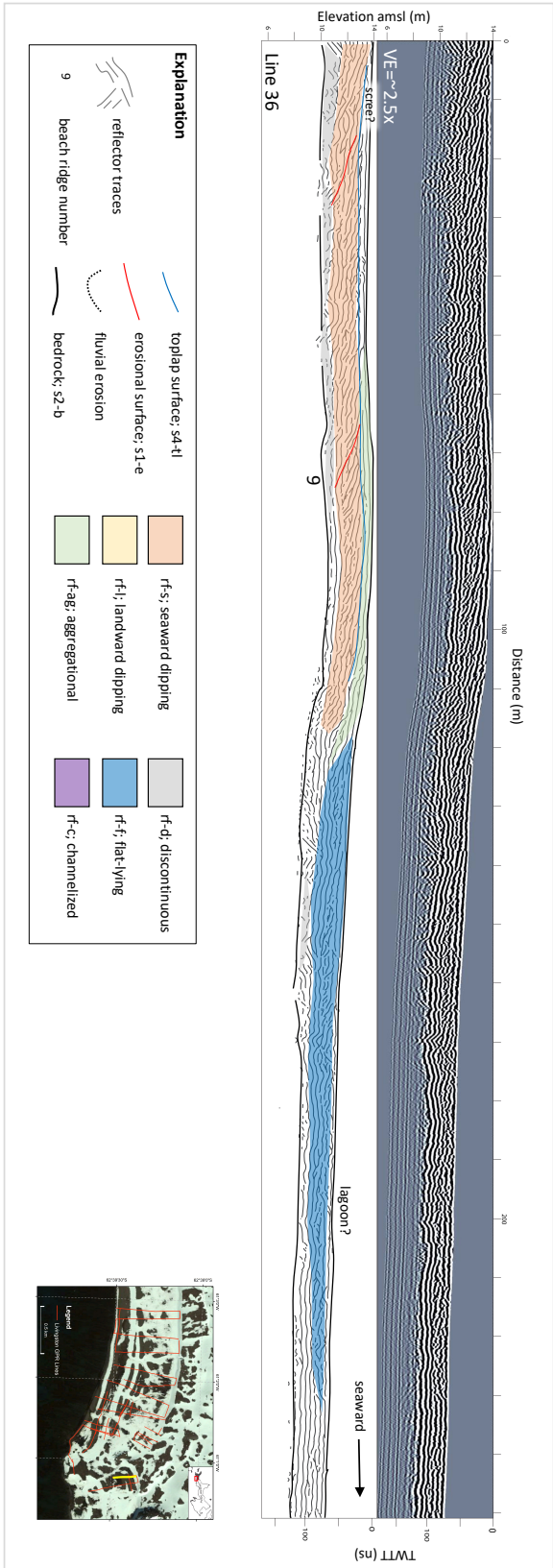
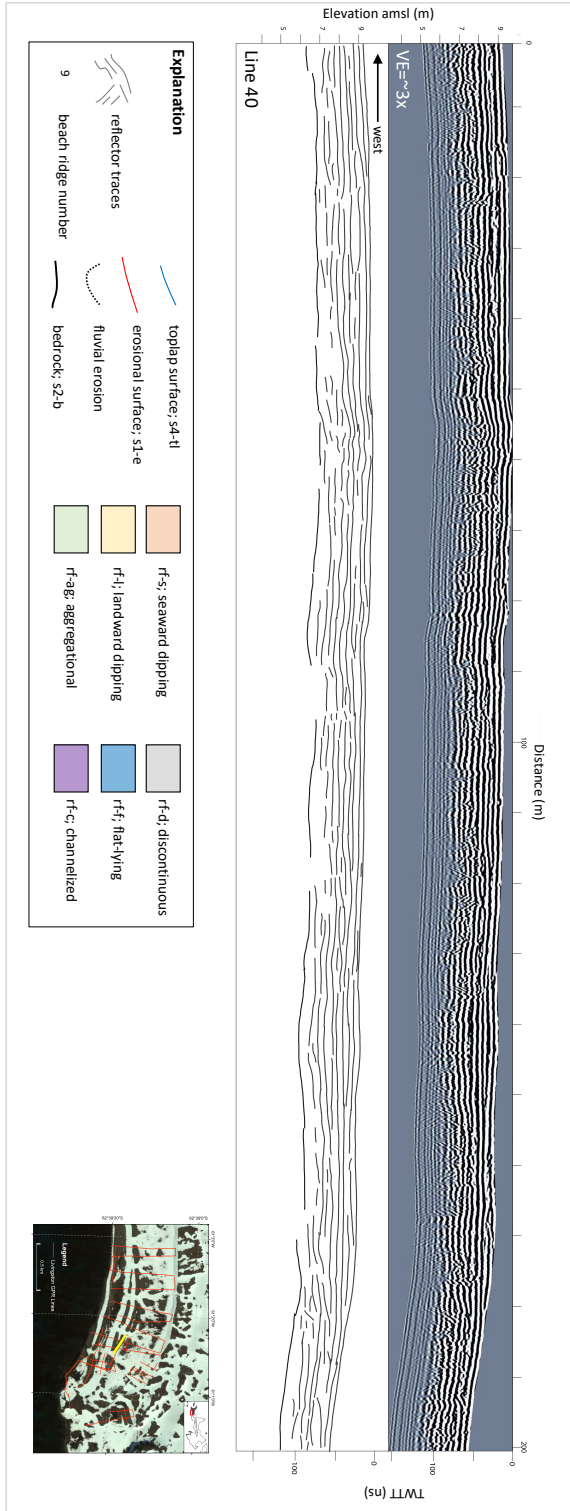


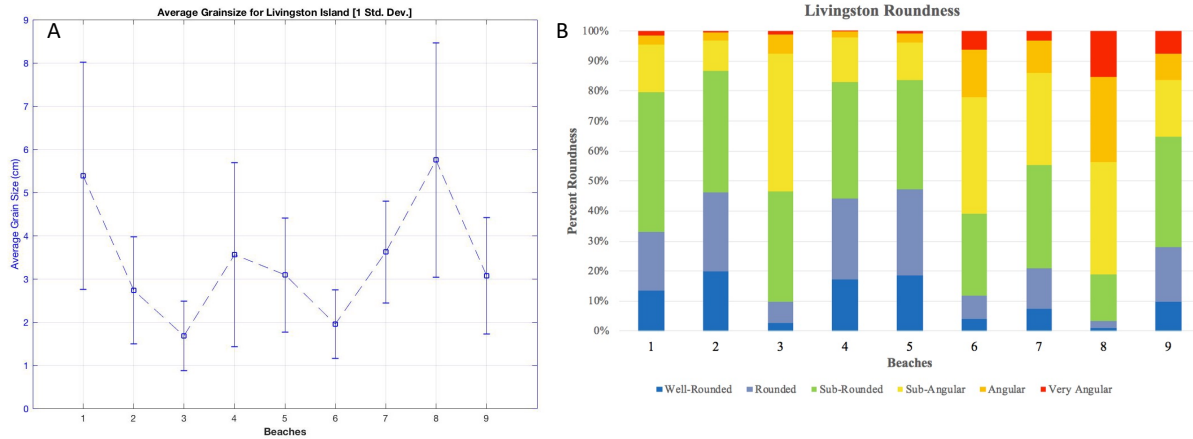
Figure 26



**Figure 27**



**Figure 27:** GPR transect Line 40 showing shore parallel stratigraphy. Beach progradation is occurring from landward to seaward, which is reflected in the shore-normal transects.

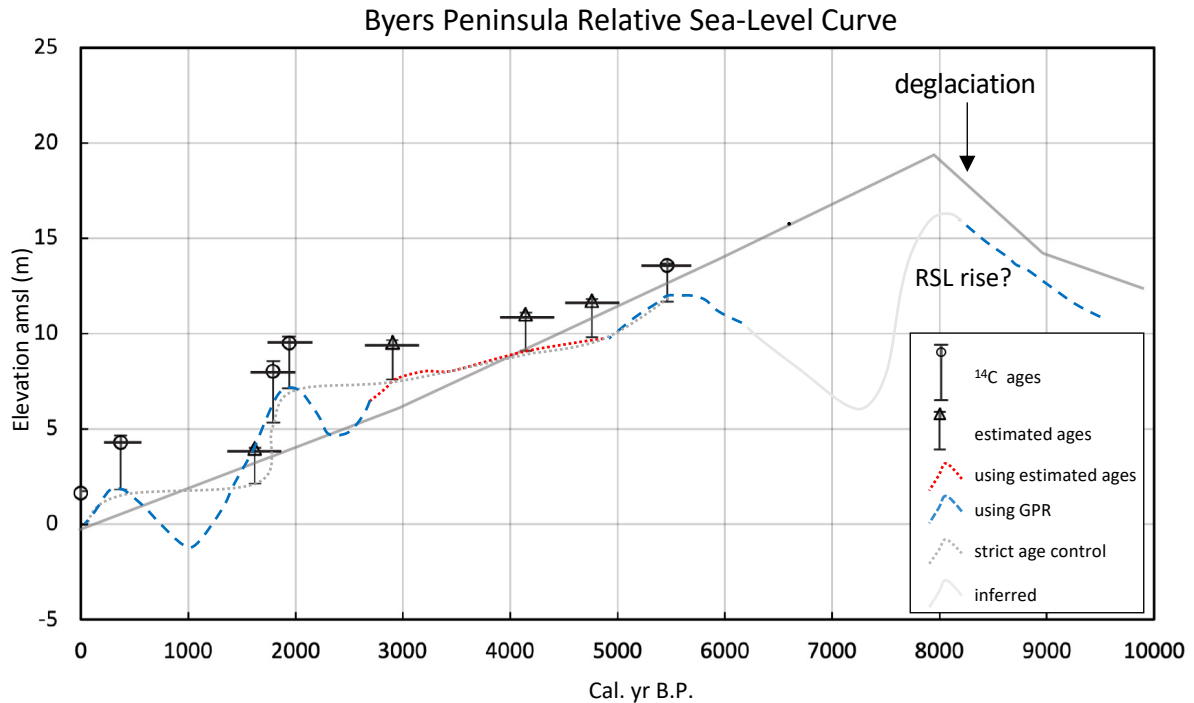


**Figure 28: A.** Average a-axis (longest axis) grain size measurements of beach surface sediments from beach ridges 1 through 9 on the South Beaches of Byers Peninsula with error bars showing  $1\sigma$ . **B.** Cumulative roundness measurements for beach ridges 1 through 9 on the South Beaches, Byers Peninsula illustrating the increased portion of well-rounded to sub-rounded sediment textures of beach ridges 1, 2, 4, 5, and 9 (Theilen, 2020).



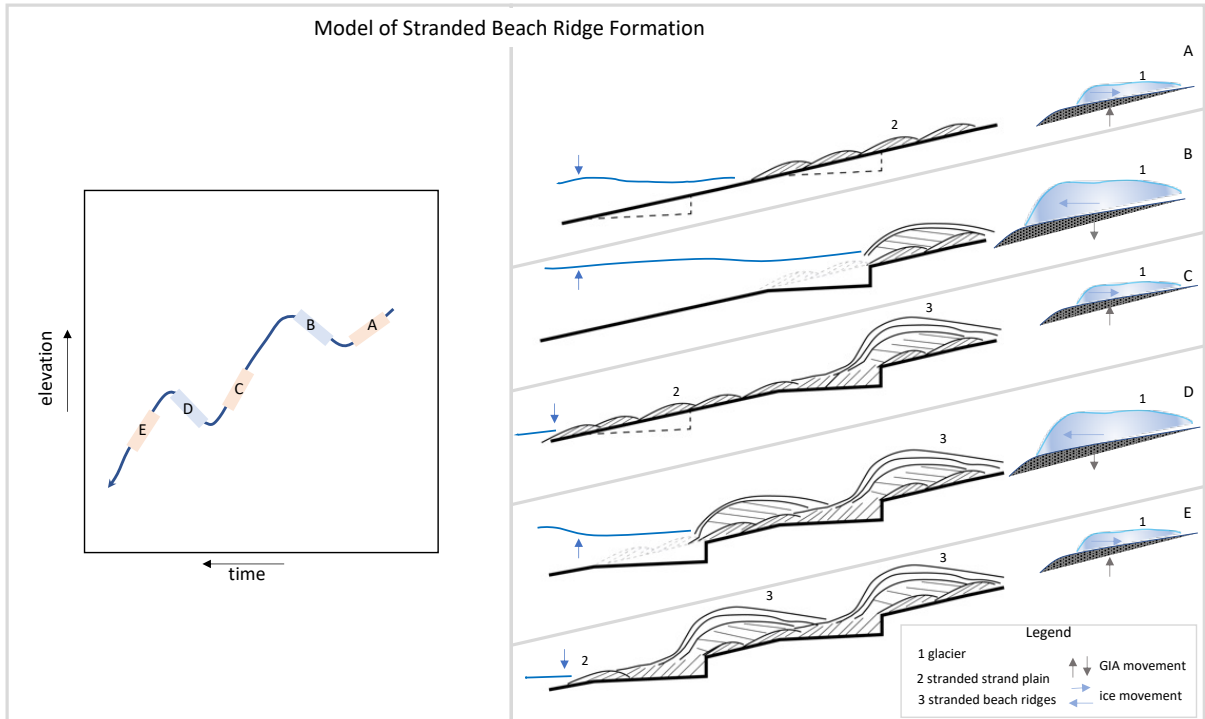


**Figure 29:** **A.** Photograph looking north standing at the terminus of Rotch Dome with a supraglacial meltwater stream carries poorly sorted clasts to the Holocene beaches and shoreline. **B.** Photograph of a moraine from the most recent glacial advance showing coarse fraction available for potential future reworking. **C.** Photograph looking south from the ice-cored Shetland I Moraine looking at outwash sediment transport from glacial terminus across the beaches to ocean.



**Figure 30:** RSL curve for Byers Peninsula. RSL rise before 8.3 ka B.P. based on stratigraphic evidence found landward of beach ridge 9 (Figs. 24 & 25) and deglaciation initiating on the west end of Byers around the same time. These sequences of sediment packages are truncated by an unconformable overwash deposit, if correctly correlated from KGI to be ~5400 cal yr B.P. Average ages of all dated beaches shown in open black circles. Ages are a compilation from beach ridges across the SSI (Tables 1 & 2). Non-local ages are correlated to the South Beaches using the isobars from Fretwell et al. (2010). Horizontal error bars show  $2\sigma$  error in cal yr B.P. Strandplain beach ages estimated using the progradation rate between beach ridges using Eq. 1. Strandplain ages shown in open black triangles. Positive vertical error bars show the  $2\sigma$  uncertainty in beach ridge elevation due to variation along strike. Negative vertical error bars show this same uncertainty in beach ridge elevation added to the elevation of the modern beach ( $1.65 \pm 0.2$  m) taken as the limit of wave runup from MSL to beach crest. The grey line is the best fit line of Byers Peninsula RSL from the W12 ice model of Byers Peninsula showing early Holocene sea-level rise before RSL fall initiated (Whitehouse et al., 2012b). The red dashed line shows the transgressions during overall RSL fall suggested in this study using the analysis of GPR to interpret beach stratigraphy.





**Figure 31:** Model of the stranded beach formation on the South Beaches of Byers Peninsula. Heavy solid lines represent bedrock. Thinner solid lines represent bedding planes, and dashed lines represent eroded bedrock and beach material. Relative times are reflected on the RSL curve to the left.

<b>Table 1: Livingston Island Beach Elevations</b>				
<i>Beach Number</i>	<i>SSI Beach</i>	<i>Distance Along Beach (m)</i>	<i>Elevation m (amsl)</i>	<i>2σ</i>
1	modern	800	1.65	0.20
2	6m	950	4.29	0.78
3*	-	-	3.85	0.14
4	10m	930	8.06	1.03
5	12m	1410	9.54	0.70
6	-	70	9.55	0.21
7	-	170	11.03	0.17
8	-	120	11.73	0.20
9	18m	170	13.59	0.19
‘ - ‘ denotes no corresponding SSI beach or transect surveyed. *Beach 3 elevation is computed from a series of individual measurements; the remainder are calculated from transects				

<b>Table 2: Byers Peninsula Compiled Radiocarbon Ages</b>								
<b>Lab ID</b>	<b><sup>14</sup>C yr BP (1σ)</b>	<b>Marine 20 Reservoir</b>	<b>Cal yr BP (median)</b>	<b>2σ</b>	<b>Material dated</b>	<b>Elevation amsl (m)</b>	<b>Location</b>	<b>Reference</b>
AA-46815	1271 ± 47	ΔR 635±42	110	257	Whale vertebra	2	South Beaches, LI	Hall and Perry, 2004
AA-45939	1431 ± 44	ΔR 635±42	255	379	Whale vertebra	4	South Beaches, LI	Hall and Perry, 2004
AA-45936	1545 ± 46	ΔR 635±42	368	331	Whale vertebra	4	South Beaches, LI	Hall and Perry, 2004
AA-45932	1625 ± 42	ΔR 635±42	435	303	Bone	5	South Beaches, LI	Hall and Perry, 2004
AA-46816	1572 ± 42	ΔR 635±42	390	303	Whalebone	6	South Beaches, LI	Hall and Perry, 2004
AA-45931	1692 ± 42	ΔR 635±42	495	307	Whalebone	6	South Beaches, LI	Hall and Perry, 2004
AA-45933	1715 ± 42	ΔR 635±42	515	302	Whalebone	4	South Beaches, LI	Hall and Perry, 2004
AA-45934	3115 ± 47	ΔR 635±42	1957	427	Whalebone	9	South Beaches, LI	Hall and Perry, 2004
SRR-1086	2823 ± 40	ΔR 635±42	1605	384	Whalebone	10.3	South Beaches, LI	Hansom, 1979
SRR-1087	3121 ± 25	ΔR 635±42	1964	375	Whalebone	10.1	South Beaches, LI	Hansom, 1979
I-7870	2530 ± 85	ΔR 635±42	1292	469	Whalebone	7.6	South Beaches, LI	Curl, 1980
AA-45928	1627±68	ΔR 635±42	435	357	Whalebone	5.7	South Beaches, LI	Hall, 2010
AA-46817	1622±42	ΔR 635±42	432	305	Whalebone	7.7	South Beaches, LI	Hall, 2010
AA-46820	1576±51	ΔR 635±42	392	327	Whalebone	5.7	South Beaches, LI	Hall, 2010
AA-46816	1572±42	ΔR 635±42	390	303	Whalebone	6.7	South Beaches, LI	Hall, 2010
AA-45935	1545±41	ΔR 635±42	368	320	Whalebone	5.7	South Beaches, LI	Hall, 2010
AA-46819	1543±53	ΔR 635±42	366	347	Whalebone	5.7	South Beaches, LI	Hall, 2010
AA-45947	1512±50	ΔR 635±42	340	350	Whalebone	9.7	South Beaches, LI	Hall, 2010
AA-45938	1461±42	ΔR 635±42	290	365	Whalebone	5.7	South Beaches, LI	Hall, 2010
AA-45945	1445±50	ΔR 635±42	271	385	Whalebone (entire whale)	5.7	President's Beaches, LI	Hall, 2010
AA-45946	1431±39	ΔR 635±42	256	372	Whalebone	5.7	President's Beaches, LI	Hall, 2010
AA-45937	1370±47	ΔR 635±42	190	357	Seaweed	5.7	South Beaches, LI	Hall, 2010
AA-46818	1315±54	ΔR 635±42	144	295	Whalebone	5.7	South Beaches, LI	Hall, 2010

AA-45942	1305±36	$\Delta R$ 635±42	132	271	Whalebone	9.7	Robbery Beaches, LI	Hall, 2010
AA-46822	1219±50	$\Delta R$ 635±42	Modern	n/a	Whalebone	3.7	President's Beaches, LI	Hall, 2010
AA-45930	1155±38	$\Delta R$ 635±42	Modern	n/a	Whalebone	2.7	South Beaches, LI	Hall, 2010
AA-45944	1142±44	$\Delta R$ 635±42	Modern	n/a	Whalebone	9.7	President's Beaches, LI	Hall, 2010
AA-45929	1132±57	$\Delta R$ 635±42	Modern	n/a	Whalebone	5.2	South Beaches, LI	Hall, 2010
AA-45941	1126±5	$\Delta R$ 635±42	Modern	n/a	Whalebone	4.2	Robbery Beaches, LI	Hall, 2010
AA-46821	1038±54	$\Delta R$ 635±42	Modern	n/a	Whalebone	4.2	President's Beaches, LI	Hall, 2010
AA-45943	958±39	$\Delta R$ 635±42	Post-bomb	n/a	Whalebone	4.7	President's Beaches, LI	Hall, 2010
AA-45940	932±48	$\Delta R$ 635±42	Post-bomb	n/a	Whalebone	4.2	Robbery Beaches, LI	Hall, 2010
AA-45927	849±41	$\Delta R$ 635±42	Post-bomb	n/a	Seaweed	9.7	South Beaches, LI	Hall, 2010

CALIB 8.2 (Stuiver et al., 2021) used to calibrate ages with the MARINE 20 dataset (Heaton et al., 2020) and an Antarctic coral-based delta-R value of  $635 \pm 42$  (Hall et al., 2010b). Lab ID from the original authors; reported  $^{14}C$  as originally published. Median cal yr B.P. and accompanying  $2\sigma$  error from recalibration. Elevations reported in m amsl are reported as they appeared in publication. Elevations reported in m above MHT are corrected to m amsl using the 0.68m offset from Theilen et al. (2020). Island abbreviation for locations of sample collection: LI=Livingston Island; GI=Greenwich Island; KGI= King George Island. Original authors cited.

**Table 3: Compiled Radiocarbon Ages from Other Locations**

<i>Lab ID</i>	$^{14}C$ yr BP ( $1\sigma$ )	<i>Marine 20 Reservoir</i>	<i>Cal yr BP (median)</i>	$2\sigma$	<i>Material dated</i>	<i>Elevation amsl (m)</i>	<i>Location</i>	<i>Reference</i>
AA-55740	3085±39	$\Delta R$ 635±42	1920	394	Seaweed, dates beach	12.7	Ash Point, GI	Hall, 2010
AA-55741	3116±40	$\Delta R$ 635±42	1958	409	Seaweed, dates beach	12.7	Ash Point, GI	Hall, 2010
Bed 3	5840±40	$\Delta R$ 635±42	5377	381	Penguin bone	15.39-15.7*	Potter Peninsula, Maxwell Bay, KGI	Del Valle et al., 2002
Bed 5	5750±40	$\Delta R$ 635±42	5272	427	Penguin bone	16.3-16.7*	Potter Peninsula, Maxwell Bay, KGI	Del Valle et al., 2002
HD9425-9100	6650±90	$\Delta R$ 635±42	6240	520	Penguin bone	18	Fildes Peninsula, Maxwell Bay, KGI	Barsch and Mäusbacher, 1986
HD8426-9106	6560±55	$\Delta R$ 635±42	6145	399	Penguin bone	18	Fildes Peninsula,	Barsch and Mäusbacher, 1986

							Maxwell Bay, KGI	
Beta-297365	1540±30	$\Delta R$ 635±42	365	305	seaweed	2.7*	Potter Peninsula, Maxwell Bay, KGI	Barión et al., 2019
Beta-304147	1600±30	$\Delta R$ 635±42	414	274	seaweed	1.1*	Potter Peninsula, Maxwell Bay, KGI	Barión et al., 2019
Beta-338478	1510±30	$\Delta R$ 635±42	341	323	seaweed	0.6*	Potter Peninsula, Maxwell Bay, KGI	Barión et al., 2019
Beta-431963	1600±30	$\Delta R$ 635±42	414	274	Penguin bone	2.3*	Potter Peninsula, Maxwell Bay, KGI	Barión et al., 2019
Beta-304149	1450 ±30	$\Delta R$ 635±42	279	354	Seaweed	2.0*	Potter Peninsula, Maxwell Bay, KGI	Lindhorst and Schutter, 2014
Beta-304150	1440 ±30	$\Delta R$ 635±42	267	359	Organic sediment	2.0*	Potter Peninsula, Maxwell Bay, KGI	Lindhorst and Schutter, 2014
Beta-322646	1490 ±30	$\Delta R$ 635±42	322	331	Shell	2.1*	Potter Peninsula, Maxwell Bay, KGI	Lindhorst and Schutter, 2014
Beta-316179	1500 ±30	$\Delta R$ 635±42	332	328	seaweed	1.8*	Potter Peninsula, Maxwell Bay, KGI	Lindhorst and Schutter, 2014
Beta-304148	1460 ±30	$\Delta R$ 635±42	290	348	seaweed	2.5*	Potter Peninsula, Maxwell Bay, KGI	Lindhorst and Schutter, 2014
Beta-338477	2920 ±30	$\Delta R$ 635±42	1720	365	seaweed	3.7*	Potter Peninsula, Maxwell Bay, KGI	Lindhorst and Schutter, 2014
Beta-316180	2850 ±30	$\Delta R$ 635±42	1636	365	seaweed	3.7*	Potter Peninsula, Maxwell Bay, KGI	Lindhorst and Schutter, 2014
Beta-328907	1510 ±30	$\Delta R$ 635±42	341	323	Shell	4.8*	Potter Peninsula, Maxwell Bay, KGI	Lindhorst and Schutter, 2014
Beta-322645	1590 ±30	$\Delta R$ 635±42	405	274	Shell	4.8*	Potter Peninsula, Maxwell Bay, KGI	Lindhorst and Schutter, 2014

Beta-316181	1600 ±30	ΔR 635±42	414	274	Shell	5.5*	Potter Peninsula, Maxwell Bay, KGI	Lindhorst and Schutter, 2014
Beta-316182	3220 ±30	ΔR 635±42	2091	385	seaweed	7.0*	Potter Peninsula, Maxwell Bay, KGI	Lindhorst and Schutter, 2014
Beta-328904	2570 ±30	ΔR 635±42	1332	322	Organic sediment	7.1*	Potter Peninsula, Maxwell Bay, KGI	Lindhorst and Schutter, 2014
Beta-328905	2970 ±30	ΔR 635±42	1780	372	seaweed	7.2*	Potter Peninsula, Maxwell Bay, KGI	Lindhorst and Schutter, 2014
Beta-328906	1780 ±30	ΔR 635±42	567	252	Organic sediment	7.2*	Potter Peninsula, Maxwell Bay, KGI	Lindhorst and Schutter, 2014
Beta-338479	4980 ±30	ΔR 635±42	4289	408	seaweed	11.5*	Potter Peninsula, Maxwell Bay, KGI	Lindhorst and Schutter, 2014

CALIB 8.2 (Stuiver et al., 2021) used to calibrate ages with the MARINE 20 dataset (Heaton et al., 2020) and an Antarctic coral-based delta-R value of  $635 \pm 42$  (Hall et al., 2010b). Lab ID from the original authors; reported  $^{14}\text{C}$  as originally published. Median cal yr B.P. and accompanying  $2\sigma$  error from recalibration. Elevations reported in m amsl are reported as they appeared in publication. Elevations reported in m above MHT are corrected to m amsl using the 0.68m offset from Theilen et al. (2020). \*Elevation of Del Valle et al. (2002) samples reported in m a.s.l. Elevation reported by Lindhorst and Schutter (2014) and Barión et al. (2019) are reported in meters above the WGS84 ellipsoid corrected for undulation of  $22.00 \pm 0.10$  m using date of EGM96 (Lemoine et al., 1998). Island abbreviation for locations of sample collection: LI=Livingston Island; GI=Greenwich Island; KGI= King George Island. Original authors cited.

<i>Beach</i>	<i>Cal yr. B.P.</i>	<i>2σ</i>	<i>4σ</i>	<i># ages</i>
1	0	n/a	n/a	n/a
2	370	160	320	26
4	1790	189	378	6
5	1940	201	402	2
9	5460	214	427	5

\*Averages were taken from 39 total ages and rounded to the nearest 10 years. Error is an average of error reported in original <sup>14</sup>C recalibration. Age compilation from South Beaches, Maxwell Bay, King George Island, and Greenwich Island and correlated using isobars from Fretwell et al. (2010).

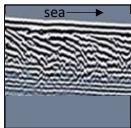
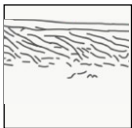
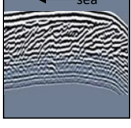

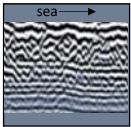

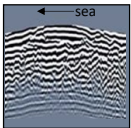
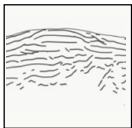
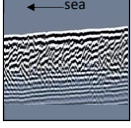

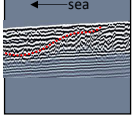
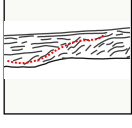
<i>Between Beach Ridges</i>	<i>Rate (m/yr)</i>	<i>2σ</i>
1 and 2	0.288	0.23
2 and 4	0.12	0.03
4 and 5	0.51	0.09
5 and 9	0.11	0.01

Rates estimated between beach ridges within the study area using the average age of the beach ridge from <sup>14</sup>C recalibration and the average lateral distances from beach crest to beach crest.

<i>Beach</i>	<i>Elevation amsl (m)</i>	<i>Age estimate (cal yr B.P.)</i>
3	4	1620
6	9.55	2900
7	11.03	4142
8	11.73	4762

Strandplain progradation rate was used to estimate the age of deposition from beach distance to a dated beach ridge landward and seaward. The average was taken except in the case of beach ridge 3 where the age was estimated using the distance to beach ridge 4 due to proximity.

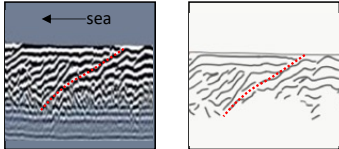
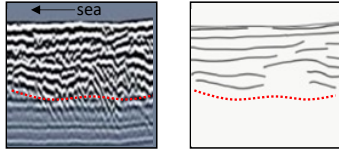
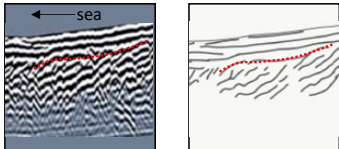
**Radar Facies**

Name		Explanation	Interpretation
rf-s	 	Seaward dipping reflections (25-50° AD; 6-15° TD), sinuous/wavy, subparallel to oblique/non-parallel, moderately continuous	Prograding foreshore deposits formed during RSL fall with sediment abundance
rf-l	 	Landward dipping reflections (9-20° AD; 2-5° TD), parallel/sinuuous, subparallel, moderately continuous	Overwash beach deposits formed during times of increased wave energy and net landward sediment transport
rf-d	 	Discontinuous variable dipping landward and seaward, semi-chaotic reflections	Reworked sediment and/or coarse clast rich deposits consisting of pebbles to cobbles, typically overlying bedrock
rf-ag	 	Horizontal and concave downward reflections with a TD of 1-2°, continuous	Storm-wave run up and vertical aggrading beds that sourced from washover (rf-l) events
rf-f	 	Continuous and strong planar horizontal reflections in topographic lows	Lagoon deposits sourced by tidal, fluvial, and aeolian sediment transport
rf-c	 	Chaotic, or lack of reflections overlain by discrete areas where surrounding reflectors abruptly terminate, accompanied with s2-b incision. Channel morphology	Fluvial deposit, eroding into all other beach features

**Table 7A:** Characteristic GPR reflection patterns (radar facies) identified using the naming scheme of Neal (2004). Black arrow points seaward in the GPR reflection panel 3. Dashed red line indicates channelized incision of the beach below and the interpreted fluvial deposits above. AD= apparent dip, TD= true dip



### Radar Surfaces

Name		Explanation	Interpretation
s1-e		Reflection of terminations in linear arrangement or linear reflection	Erosional surface
s2-b		Hyperbola dense layer underlain by ringing multiples and/or absent of reflections	Bedrock covered in cobble pavement
s4-tl		Reflections that pinch out on their upper boundary against the overlying surface or reflector	Deflation surface

**Table 7B:** Characteristic GPR radar surfaces identified using the naming scheme of Neal (2004). Surfaces within this table are shown with dashed red line. Black arrow points seaward in the GPR reflection panel 3. AD= apparent dip, TD= true dip

<b>Table 8: Livingston Island Platform Erosion Rates</b>						
<i>Scarp #</i>	<i>Eroded Between Beaches</i>	<i>Distance (m)</i>	<i>Formula equivalent distance</i>	<i>Time for erosion (yr)</i>	<i>Formula equivalent time</i>	<i>Erosion Rate (m/yr)</i>
2	1 and 2	106	$(D_3 - D_4)$	1420	$(T_3 - T_4)$	0.07
4 & 5	2 and 4	176	$(D_2 - D_3)$	3520	$(T_2 - T_3)$	0.05
9	5 and 9	397	$(D_1 - D_2)$	4040	$(T_0 - T_1)$	0.10

Scarps numbered for corresponding overlying beach ridge. Scarp erosion estimated using Eq. 2 in the text.

<b>Table 9: Livingston Island Grain-size Data</b>			
<i><b>Beach ID</b></i>	<i><b>Average (cm)</b></i>	<i><b>Median (cm)</b></i>	<i><b>Standard Deviation</b></i>
<b>Modern</b>	5.39	4.80	2.63
<b>2</b>	2.73	2.30	1.24
<b>3</b>	1.68	1.49	0.80
<b>4</b>	3.56	3.0	2.13
<b>5</b>	3.09	2.80	1.32
<b>6</b>	1.95	1.80	0.79
<b>7</b>	3.62	3.30	1.18
<b>8</b>	5.75	5.0	2.71
<b>9</b>	3.07	2.70	1.35
<b>Island Average</b>	3.43	3.02	1.57
Data from Theilen et al., 2020			

## References

- Adie, R.J., 1977, Earth sciences: the geology of Antarctica: a review: *Philosophical Transactions of the Royal Society of London. B, Biological Sciences*, v. 279, no. 963, pp.123-130.
- Anderson, J.B., Shipp, S.S., Lowe, A.L., Wellner, J.S. and Mosola, A.B., 2002. The Antarctic Ice Sheet during the Last Glacial Maximum and its subsequent retreat history: a review: *Quaternary Science Reviews*, v. 21 no. 1-3, pp.49-70.
- Ballantyne, C.K., 2002, Paraglacial geomorphology: *Quaternary Science Reviews*, v. 21, no. 18-19, pp.1935-2017.
- Bañón, M., Justel, A., Velázquez, D. and Quesada, A., 2013, Regional weather survey on Byers Peninsula, Livingston Island, South Shetland Islands, Antarctica: *Antarctic Science*, v. 25, no. 2, pp.146-156.
- Barión, H.P., Lindhorst, S., Schutter, I., Falk, U. and Kuhn, G., 2019, Reaction of a polar gravel-spit system to atmospheric warming and glacier retreat as reflected by morphology and internal sediment geometries (South Shetland Islands, Antarctica): *Earth Surface Processes and Landforms*, v. 44, no. 5, pp.1148-1162.
- Barker, D.H. and Austin Jr, J.A., 1998, Rift propagation, detachment faulting, and associated magmatism in Bransfield Strait, Antarctic Peninsula: *Journal of Geophysical Research: Solid Earth*, v. 103, no. B10, pp.24017-24043.
- Barker, D.H.N. and Austin Jr, J.A., 1994, Crustal diapirism in Bransfield Strait, West Antarctica: Evidence for distributed extension in marginal-basin formation: *Geology*, v. 22, no. 7, pp.657-660.
- Barker, P.F. and Dalziel, I.W., 1983, Progress in geodynamics in the Scotia Arc region: Geodynamics of the eastern Pacific region, Caribbean and Scotia Arcs, v. 9, pp.137-170.
- Barker, P.F., Dalziel, I.Y. and Storey, B.C., 1991, Tectonic development of the Scotia Arc region. In *The geology of Antarctica*, pp. 215-248.
- Barsch, D. and Mäusbacher, R., 1986, New Data on the Relief Development of the South Shetland Islands, Antarctica: *Interdisciplinary Science Reviews*, v. 11, no. 2, p. 211-218, doi: 10.1179/isr.1986.11.2.211.
- Barton, C.M., 1965, The geology of the South Shetland Islands: III. The stratigraphy of King George Island: *British Antarctic Survey, Scientific Reports*, no. 44.
- Belknap, D.F., 2005, Glaciated Coasts. In: Schwartz M.L. (eds) *Encyclopedia of Coastal Science*. *Encyclopedia of Earth Science Series*. Springer, Dordrecht.  
[https://doi.org/10.1007/1-4020-3880-1\\_153](https://doi.org/10.1007/1-4020-3880-1_153)
- Bentley, M., Hodgson, D., Smith, J., and Cox, N., 2005a, Relative sea level curves for the South Shetland Islands and Marguerite Bay, Antarctic Peninsula: *Quaternary Science Reviews*, v. 24, no. 10-11, p. 1203-1216.

- Bentley, M., Hodgson, D., Smith, J., Cofaigh, C., Domack, E., Larter, R., Roberts, S., Brachfeld, S., Leventer, A., and Hjort, C., 2009, Mechanisms of Holocene palaeoenvironmental change in the Antarctic Peninsula region: *The Holocene*, v. 19, no. 1, p. 51-69.
- Bentley, M.J., Hodgson, D.A., Smith, J.A., Cofaigh, C.O., Domack, E.W., Larter, R.D., Roberts, S.J., Brachfeld, S., Leventer, A., Hjort, C. and Hillenbrand, C.D., 2009, Mechanisms of Holocene palaeoenvironmental change in the Antarctic Peninsula region: *The Holocene*, v. 19, no. 1, pp.51-69.
- Bentley, M., Hodgson, D., Sugden, D., Roberts, S., Smith, J., Leng, M., and Bryant, C., 2005b, Early Holocene retreat of the George VI ice shelf, Antarctic Peninsula: *Geology*, v. 33, no. 3, pp. 173-176.
- Bentley, M.J., Fogwill, C.J., Kubik, P.W. and Sugden, D.E., 2006, Geomorphological evidence and cosmogenic  $^{10}\text{Be}/^{26}\text{Al}$  exposure ages for the Last Glacial Maximum and deglaciation of the Antarctic Peninsula Ice Sheet: *Geological Society of America Bulletin*, v. 118, no.9-10, pp.1149-1159.
- Bentley, M.J., Hodgson, D.A., Smith, J.A., Cox, N.J., 2005, Relative sea level curves for the South Shetland Islands and Marguerite Bay, Antarctic Peninsula: *Quaternary Science Reviews*, v. 24, pp. 1203-1216, doi:10.1016/j.quascirev.2004.10.004.
- Berkman, P.A. and Forman, S.L., 1996, Pre-bomb radiocarbon and reservoir correction for calcareous marine species in the Southern Ocean: *Geophysical Research Letters*, v. 23, no. 4, pp. 363-366, doi: 0094-8534/96/96GL-00151 \$03.00.
- Berrocso, M., Fernández-Ros, A., Prates, G., García, A. and Kraus, S., 2016, Geodetic implications on block formation and geodynamic domains in the South Shetland Islands, Antarctic Peninsula: *Tectonophysics*, v. 666, pp.211-219.
- Billy, J., Robin, N., Hein, C.J., Certain, R., FitzGerald, D.M., 2014, Internal architecture of mixed sand-and-gravel beach ridges: Miquelon-Langlade Barrier, NW Atlantic: *Marine Geology*, v. 357, p. 53-71, <http://dx.doi.org/10.1016/j.margeo.2014.07.011>.
- Björck, S., Hjort, C., Ingólfsson, O., Zale, R., and Ising, J., 1996, Holocene deglaciation chronology from lake sediments, *Geomorphological Map of Byers Peninsula, Livingston Island. Bas Geomap Series Sheet 5-a, British Antarctic Survey*, pp. 49-51.
- Bøtter-Jensen, L., McKeever, S.W.S., Wintle, A.G., 2003, *Optically Stimulated Luminescence Dosimetry*: Elsevier, Amsterdam.
- Bristow, C.S., Augustinus, P.C., Wallis, I.C., Jol, H.M., Rhodes, E.J., 2010, Investigation of the age and migration of reversing dunes in Antarctica using GPR and OSL, with implications for GPR on Mars: *Earth and Planetary Science Letters*, v. 289, pp. 30-42.
- Carlson, A.E. and Clark, P.U., 2012, Ice sheet sources of sea level rise and freshwater discharge during the last deglaciation: *Reviews of Geophysics*, v. 50, no. 4.
- Carter, R.W.G. and Orford, J.D., 1993, The morphodynamics of coarse clastic beaches and barriers: a short-and long-term perspective: *Journal of Coastal Research*, pp.158-179.

- Carter, R.W.G., 1986, The morphodynamics of beach ridge formation: Magilligan, Northern Ireland: *Marine Geology*, v. 73, p. 191-214.
- Chelli, A., Pappalardo, M., Llopis, I.A. and Federici, P.R., 2010, The relative influence of lithology and weathering in shaping shore platforms along the coastline of the Gulf of La Spezia (NW Italy) as revealed by rock strength: *Geomorphology*, v. 118, no. 1-2, pp.93-104.
- Chu, Z., Sun, L., Wang, Y., Huang, T. and Zhou, X., 2017, Depositional environment and climate changes during the Holocene in grande valley, Fildes peninsula, king George island, Antarctica: *Antarctic Science*, v. 29, no. 6, pp.545-554.
- Clemmensen, L.B., and Nielsen, L., 2009, Internal architecture of a raised beach ridge system (Anholt, Denmark) resolved by ground-penetrating radar investigations: *Sedimentary Geology*, v. 223, p. 281-290, doi:10.1016/j.sedgeo.2009.11.014.
- Conrad, C.P., 2013, The solid Earth's influence on sea level: *Bulletin*, v. 125, no. 7-8, pp.1027-1052.
- Costas, S., Ferreira, Ó., Plomaritis, T.A. and Leorri, E., 2016, Coastal barrier stratigraphy for Holocene high-resolution sea-level reconstruction: *Scientific reports*, v. 6, no. 1, pp.1-12.
- Costa, P.J. and Andrade, C., 2020. Tsunami deposits: Present knowledge and future challenges: *Sedimentology*, v. 67, no. 3, pp.1189-1206.
- Curl, J. E., 1980, A glacial history of the South Shetland Islands, Antarctica: Institute of Polar Studies, The Ohio State University.
- De Pablo, M.A., Ramos, M. and Molina, A., 2014, Thermal characterization of the active layer at the Limnopolar Lake CALM-S site on Byers Peninsula (Livingston Island) : *Antarctica: Solid Earth*, v. 5, no. 2, pp.721-739.
- Del Valle, R.A., Montalti, D. and Inbar, M., 2002, Mid-Holocene macrofossil-bearing raised marine beaches at Potter Peninsula, King George Island, South Shetland Islands: *Antarctic Science*, v. 14, no. 3, pp.263-269.
- Dietrich, R., A. Rulke, J. Ihde, K. Lindner, H. Miller, W. Niemeier, H.-W. Schenke, and G. Seeber, 2004, Plate kinematics and deformation status of the Antarctic Peninsula based on GPS, *Global Planet: Change*, v. 42, pp. 313–321.
- Dinther, Y., Preiswerk, L.E. and Gerya, T.V., 2019, A secondary zone of uplift due to megathrust earthquakes: *Pure and Applied Geophysics*, v. 176, no. 9, pp.4043-4068.
- Domack, E. W., Leventer, A., Root, S., Ring, J., Williams, E., Carlson, D., Hirshorn, E., Wright, W., Gilbert, R., and Burr, G., 2003b, Marine sedimentary record of natural environmental variability and recent warming in the Antarctic Peninsula: *Antarctic peninsula climate variability: Historical and paleoenvironmental perspectives*, v. 79, pp. 205-224.
- Engels, S., and Roberts, M.C., 2005, The architecture of prograding sandy-gravel beach ridges formed during the last Holocene highstand: Southwestern British Columbia,

- Canada: *Journal of Sedimentary Research*, v. 75, pp. 1052-1064, doi:10.2110/jsr.2005.081.
- Evans, D., Lautenbacher, C., Spinrad, R., and Szabados, M., 2003, Computational techniques for tidal datums handbook: NOAA Special Publication NOS CO-OPS, v. 2.
- Fretwell, P.T., Hodgson, D.A., Watcham, E.P., Bentley, M.J., Roberts, S.J., 2010, Holocene isostatic uplift of the South Shetland Islands, Antarctic Peninsula, modelled from raised beaches: *Quaternary Science Reviews*, v. 29, pp. 1880-1893, doi:10.1016/j.quascirev.2010.04.006.
- Fournier, A., and Allard, M., 1992, Periglacial shoreline erosion of a rocky coast: George River Estuary, northern Quebec: *Journal of Coastal Research*, pp.926-942.
- Gràcia, E., Canals, M., Farràn, M.L., Sorribas, J. and Pallàs, R., 1997, Central and eastern Bransfield basins (Antarctica) from high-resolution swath-bathymetry data: *Antarctic Science*, v. 9, no. 2, pp.168-180.
- Guglielmin, M., Convey, P., Malfasi, F. and Cannone, N., 2016, Glacial fluctuations since the 'Medieval warm period' at Rothera Point (western Antarctic Peninsula): *The Holocene*, v. 26, no. 1, pp.154-158.
- Haase, K.M., Beier, C., Fretzdorff, S., Smellie, J.L. and Garbe-Schönberg, D., 2012, Magmatic evolution of the South Shetland Islands, Antarctica, and implications for continental crust formation: *Contributions to Mineralogy and Petrology*, v. 163, no. 6, pp.1103-1119.
- Hall, B.L., 2003, An overview of late Pleistocene glaciation in the South Shetland Islands: *Antarctic Research Series*, v. 79, pp. 103-113.
- Hall, B.L., 2007, Late-Holocene advance of the Collins Ice Cap, King George Island, South Shetland Islands: *The Holocene*, v. 17, no. 8, pp. 1253-1258.
- Hall, B.L., 2009, Holocene glacial history of Antarctica and the sub-Antarctic islands: *Quaternary Science Reviews*, v. 28, no. 21-22, pp. 2213-2230.
- Hall, B., Henderson, G. M., Baroni, C., and Kellogg, T. B., 2010b, Constant Holocene Southern-Ocean  $^{14}\text{C}$  reservoir ages and ice-shelf flow rates: *Earth and Planetary Science Letters*, v. 296, no. 1-2, pp. 115-123.
- Hall, B.L., Koffman, T., and Denton, G., 2010a, Reduced ice extent on the western Antarctic Peninsula at 700–970 cal. yr BP: *Geology*, v. 38, no. 7, pp. 635-638.
- Hall, B.L. and Denton, G.H., 1999, New relative sea-level curves for the southern Scott Coast, Antarctica: evidence for Holocene deglaciation of the western Ross Sea: *Journal of Quaternary Science*, v. 14, no. 7, pp.641-650.
- Hall, B.L., 2010, Holocene relative sea-level changes and ice fluctuations in the South Shetland Islands: *Global and Planetary Change*, v. 74, pp. 15-26, doi:10.1016/j.gloplacha.2010.07.007.
- Hall, B.L., and Perry, E.R., 2004, Variations in ice rafted detritus on beaches in the South Shetland Islands: a possible climate proxy: *Antarctic Science*, v. 16, pp. 339-344.

- Hansom, J.D., 1979, Radiocarbon dating of a raised beach at 10 m in the South Shetland Islands, *Antarctica: Marine Geology*, v. 53, pp.211-229.
- Hansom, J.D., 1983, Shore-platform development in the South Shetland islands, *Antarctica: Marine Geology*, v. 53, no. 3, pp.211-229.
- Hansom, J.D. and FLINT, C., 1989, Short notes Holocene ice fluctuations on Brabant Island, Antarctic Peninsula: *Antarctic Science*, v. 1, no. 2, pp.165-166.
- Hansom, J.D., and Kirk, R.M., 1989, Ice in the intertidal zone: examples from Antarctica: *Essener Geographische Arbeiten*, v. 18, no. 1989, pp. 211-236
- Heaton, T.J., Köhler, P., Butzin, M., Bard, E., Reimer, R.W., Austin, W.E., Ramsey, C.B., Grootes, P.M., Hughen, K.A., Kromer, B. and Reimer, P.J., 2020, Marine20—the marine radiocarbon age calibration curve (0–55,000 cal BP): *Radiocarbon*, v. 62, no. 4, pp.779-820.
- Hobbs, G., 1968, The geology of the South Shetland Islands: IV. The geology of Livingston Island, British Antarctic Survey. Smellie, J.L., Pankhurst, R., Thomson, M.R.A. and Davies, R.E.S., 1984. The geology of the South Shetland Islands: VI. Stratigraphy, geochemistry and evolution (V. 87) : British Antarctic Survey.
- Hong, S., Lee, M.K., Seong, Y.B. et al. 2021, Holocene sea-level history and tectonic implications derived from luminescence dating of raised beaches in Terra Nova Bay, Antarctica: *Geosci J* 25, 283–298 (2021). <https://doi.org/10.1007/s12303-020-0031-x>
- IPCC, 2019: Technical Summary [H.-O. Pörtner, D.C. Roberts, V. Masson-Delmotte, P. Zhai, E. Poloczanska, K. Mintenbeck, M. Tignor, A. Alegría, M. Nicolai, A. Okem, J. Petzold, B. Rama, N.M. Weyer (eds.)]. In: *IPCC Special Report on the Ocean and Cryosphere in a Changing Climate* [H.- O. Pörtner, D.C. Roberts, V. Masson-Delmotte, P. Zhai, M. Tignor, E. Poloczanska, K. Mintenbeck, A. Alegría, M. Nicolai, A. Okem, J. Petzold, B. Rama, N.M. Weyer (eds.)]. In press.
- Ivins, E.R. and James, T.S., 2005, Antarctic glacial isostatic adjustment: a new assessment: *Antarctic Science*, v. 17, no. 4, pp.541-553.
- Jahn, A., 1961, Quantitative analysis of some periglacial processes in Spitsbergen: *Nauka O Ziemi II B*, v. 5, pp.3-34.
- John, B.S. and Sugden, D.E., 1971, Raised Marine Features and Phases of Glaciation in the South Shetland Islands: *British Antarctic Survey Bulletin*, No. 25, p. 45-111.
- Johnston, V.E., McDermott, F. and Tămaş, T., 2010, A radiocarbon dated bat guano deposit from NW Romania: implications for the timing of the Little Ice Age and Medieval Climate Anomaly: *Palaeogeography, Palaeoclimatology, Palaeoecology*, v. 291, no. 3-4, pp.217-227.
- Kelsey, H., 2015, Geomorphological indicators of past sea levels: *Handbook of sea-level research*, pp.66-82.
- Khim, B.K., Yoon, H.I., Kang, C.Y. and Bahk, J.J., 2002, Unstable climate oscillations during the late Holocene in the eastern Bransfield Basin, Antarctic Peninsula: *Quaternary Research*, v. 58, no. 3, pp.234-245.

- Koster, B., Hadler, H., Vött, A. and Reicherter, K., 2013. Application of GPR for visualising spatial distribution and internal structures of tsunami deposits—Case studies from Spain and Greece.: *Zeitschrift für Geomorphologie, Supplementary Issues*, v. 57, no. 4, pp.29-45.
- Lambeck, K., Rouby, H., Purcell, A., Sun, Y. and Sambridge, M., 2014, Sea level and global ice volumes from the Last Glacial Maximum to the Holocene: *Proceedings of the National Academy of Sciences*, v. 111, no. 43, pp.15296-15303.
- Larsen, C.F., Motyka, R.J., Freymueller, J.T., Echelmeyer, K.A. and Ivins, E.R., 2005, Rapid viscoelastic uplift in southeast Alaska caused by post-Little Ice Age glacial retreat: *Earth and planetary Science letters*, v.237, no. 3-4, pp.548-560.
- Larter, R.D. and Barker, P.F., 1991, Effects of ridge crest-trench interaction on Antarctic-Phoenix spreading: forces on a young subducting plate. *Journal of Geophysical Research: Solid Earth*, v. 96, no. B12, pp.19583-19607.
- Lawver, L.A., Sloan, B.J., Barker, D.H., Ghidella, M., Von Herzen, R.P., Keller, R.A., Klinkhammer, G.P. and Chin, C.S., 1996, Distributed, active extension in Bransfield Basin, Antarctic Peninsula: evidence from multibeam bathymetry: *GSA Today*, v. 6, no. 11, pp.1-6.
- Lindhorst, S., and Schutter, I., 2014, Polar gravel beach-ridge systems: Sedimentary architecture, genesis, and implications for climate reconstructions (South Shetland Islands/Western Antarctic Peninsula): *Geomorphology*, v. 221, p. 187-203, <http://dx.doi.org/10.1016/j.geomorph.2014.06.013>.
- Lindsay, D.C., 1971, *Vegetation of the South Shetland Islands: British Antarctic Survey Bulletin*, v. 25, pp.59-83.
- Lüning, S., Gałka, M. and Vahrenholt, F., 2019, The medieval climate Anomaly in Antarctica: *Palaeogeography, Palaeoclimatology, Palaeoecology*, v. 532, pp.109251.
- Luo, Q. and Zhang, G., 2018, Control of subduction rate on Tonga-Kermadec arc magmatism: *Journal of Oceanology and Limnology*, v. 36, no. 3, pp.687-699.
- Mann, M.E., Bradley, R.S. and Hughes, M.K., 1999, Northern hemisphere temperatures during the past millennium: Inferences, uncertainties, and limitations: *Geophysical research letters*, v. 26, no. 6, pp.759-762.
- Mason, T. and Coates, T.T., 2001, Sediment transport processes on mixed beaches: a review for shoreline management: *Journal of Coastal Research*, pp.645-657.
- Matthews, J.A., Dawson, A.G. and Shakesby, R.A., 1986, Lake shoreline development, frost weathering and rock platform erosion in an alpine periglacial environment, Jotunheimen, southern Norway: *Boreas*, v. 15, no. 1, pp.33-50.
- Maurice, R., S.D., Wiens, D.A., Shore, P.J., Vera, E. and Dorman, L.M., 2003, Seismicity and tectonics of the South Shetland Islands and Bransfield Strait from a regional broadband seismograph deployment: *Journal of Geophysical Research: Solid Earth*, v. 108, no. B10.



- Mäusbacher, R., Müller, J. and Schmidt, R., 1989, Evolution of postglacial sedimentation in Antarctic lakes (King George Island): *Zeitschrift für Geomorphologie*, pp.219-234.
- McKay, P.J. and Terich, T.A., 1992, Gravel Barrier Morphology: Olympic National Park, Washington State, U.S.A.: *Journal of Coastal Research*, v. 8, no. 4, p. 813-829, ISSN 0749-0208.
- Miao, X., Mason, J.A., Swinehart, J.B., Loope, D.B., Hanson, P.R., Goble, R.J. and Liu, X., 2007, A 10,000 year record of dune activity, dust storms, and severe drought in the central Great Plains: *Geology*, v. 35, no. 2, pp.119-122.
- Michalchuk, B. R., Anderson, J. B., Wellner, J. S., Manley, P. L., Majewski, W., and Bohaty, S., 2009, Holocene climate and glacial history of the northeastern Antarctic Peninsula: the marine sedimentary record from a long SHALDRIL core: *Quaternary Science Reviews*, v. 28, no. 27-28, p. 3049-3065.
- Moore, L.J. and Griggs, G.B., 2002, Long-term cliff retreat and erosion hotspots along the central shores of the Monterey Bay National Marine Sanctuary: *Marine Geology*, v. 181, no. 1-3, pp.265-283.
- Neal, A., 2004, Ground-penetrating radar and its use in sedimentology: principles, problems, and progress: *Earth-Science Reviews*, v. 66, p. 261-330.
- Nichols, R.L., 1961, Characteristics of beaches formed in polar climates: *American Journal of Science*, v. 259, no. 9, pp.694-708.
- Nield, G.A., Barletta, V.R., Bordoni, A., King, M.A., Whitehouse, P.L., Clarke, P.J., Domack, E., Scambos, T.A., Berthier, E., 2014, Rapid bedrock uplift in the Antarctic Peninsula explained by viscoelastic response to recent ice unloading: *Earth and Planetary Science Letters*, v. 397, p. 32-41.
- Nielsen, L., and Clemmensen, L.B., 2009, Sea-level markers identified in ground-penetrating radar data collected across modern beach ridge system in a microtidal regime: *Terra Nova*, v. 21, p. 474-479, doi: 10.1111/j.1365-3121.2009.00904.x.
- Nielsen, L., Bendixen, M., Kroon, A., Hede, M.U., Clemmensen, L.B., Weßling, R. and Elberling, B., 2017, Sea-level proxies in Holocene raised beach ridge deposits (Greenland) revealed by ground-penetrating radar: *Scientific Reports*, v. 7, no. 1, pp.1-8.
- Nielsen, L., Bendixen, M., Kroon, A., Hede, M.U., Clemmensen, L.B., Weßling, R. and Elberling, B., 2017, Sea-level proxies in Holocene raised beach ridge deposits (Greenland) revealed by ground-penetrating radar: *Scientific reports*, v. 7, no. 1, pp.1-8.
- Oliva, M., and Fernandez, J.R., 2017, Geomorphological processes and frozen ground conditions in Elephant Point (Livingston Island, South Shetland Islands, Antarctica): *Geomorphology*, v. 293, p. 368-379.
- Oliva, M., Antoniades, D., Giralt, S., Granados, I., Pla-Rabes, S., Toro, M., Liu, E.J., Sanjurjo, J. and Vieira, G., 2016, The Holocene deglaciation of the Byers Peninsula

- (Livingston Island, Antarctica) based on the dating of lake sedimentary records: *Geomorphology*, v. 261, pp.89-102.
- Orford, J.D. and Carter, R.W.G., 1982, Crestal overtop and washover sedimentation on a fringing sandy gravel barrier coast, Carnsore Point, Southeast Ireland: *Journal of Sedimentary Research*, v. 52, no. 1, pp.265-278.
- Otvos, E.G., 2000, Beach ridges – definitions and significance: *Geomorphology*, v. 32, p. 83-108.
- Palacios, D., Ruiz-Fernández, J., Oliva, M., Andrés, N., Fernández-Fernández, J. M., Schimmelpfennig, I., Leanni, L., González-Díaz, B., and Team, A., 2020, Timing of formation of neoglacial landforms in the South Shetland Islands (Antarctic Peninsula): Regional and global implications: *Quaternary Science Reviews*, v. 234, p. 106248.
- Pallas, R., James, T.S., Sabat, F., Vilaplana, J.M., Grant, D.R., 1997, Holocene uplift in the South Shetland Islands: evaluation of tectonics and glacio-isostasy: *The Antarctic Region: Geological Evolution and Processes*, p. 861-868.
- Peltier, W.R., 1999, Global sea level rise and glacial isostatic adjustment: *Global and Planetary Change*, v. 20, no. 2-3, pp.93-123.
- Plafker, G., 1969, Tectonics of the March 27, 1964, Alaska earthquake: U.S. Geological Survey Professional Paper 543-I, 74 p., 2 sheets, scales 1:2,000,000 and 1:500,000, <https://pubs.usgs.gov/pp/0543i/>.
- Pritchard, H.D., and Vaughan, D.G., 2007, Widespread acceleration of tidewater glaciers on the Antarctic Peninsula: *J. Geophys. Res. Earth Surf.* v.112, p. 1-10.
- Roberts, S., Hodgson, D. A., Sterken, M., Whitehouse, P. L., Verleyen, E., Vyverman, W., Sabbe, K., Balbo, A., Bentley, M. J., and Moreton, S. G., 2011, Geological constraints on glacio-isostatic adjustment models of relative sea-level change during deglaciation of Prince Gustav Channel, Antarctic Peninsula: *Quaternary Science Reviews*, v. 30, no. 25-26, p. 3603-3617.
- Roberts, S., Hodgson, D., Bentley, M., Sanderson, D., Milne, G., Smith, J., Verleyen, E., and Balbo, A., 2009, Holocene relative sea-level change and deglaciation on Alexander Island, Antarctic Peninsula, from elevated lake deltas: *Geomorphology*, v. 112, no. 1-2, p. 122-134.
- Ruiz-Fernández, J. and Oliva, M., 2016, Relative paleoenvironmental adjustments following deglaciation of the Byers Peninsula (Livingston Island, Antarctica): *Arctic, Antarctic, and Alpine Research*, v. 48, no.2, pp.345-359.
- Scheffers, A., Engel, M., Scheffers, S., Squire, P., and Kelletat, D., 2012, Beach ridge systems—archives for Holocene coastal events?: *Progress in Physical Geography*, v. 36, no. 1, pp. 5-37.
- Seong, Y.B., Owen, L.A., Lim, H.S., Yoon, H.I., Kim, Y., Lee, Y.I. and Caffee, M.W., 2009, Rate of late Quaternary ice-cap thinning on King George Island, South Shetland

- Islands, West Antarctica defined by cosmogenic  $^{36}\text{Cl}$  surface exposure dating: *Boreas*, v. 38, no. 2, pp.207-213.
- Shevenell, A., Ingalls, A., Domack, E., and Kelly, C., 2011, Holocene Southern Ocean surface temperature variability west of the Antarctic Peninsula: *Nature*, v. 470, no. 7333, p. 250.
- Shevenell, A.E., Domack, E.W. and Kernan, G.M., 1996, Record of Holocene palaeoclimate change along the Antarctic Peninsula: evidence from glacial marine sediments, Lallemand Fjord: *Papers and Proceedings of the Royal Society of Tasmania*, v. 130, no. 2, pp. 55-64.
- Simkins, L. M., Simms, A. R., and DeWitt, R., 2013, Relative sea-level history of Marguerite Bay, Antarctic Peninsula derived from optically stimulated luminescence-dated beach cobbles: *Quaternary Science Reviews*, v. 77, pp. 141-155.
- Simms, A.R., Bentley, M., Simkins, L., Zurbuchen, J., Reynolds, L., DeWitt, R., Thomas, E.R., Accepted, Evidence for a “Little Ice Age” glacial advance within the Antarctic Peninsula –examples from glacially-overrun raised beaches: *Quaternary Science Review*.
- Simms, A.R., DeWitt, R., Kouremenos, P., Drewry, A.M., 2011, A new approach to reconstructing sea levels in Antarctica using optically stimulated luminescence of cobble surfaces: *Quaternary Geochronology*, v. 6, pp. 50-60, doi:10.1016/j.quageo.2010.06.004.
- Simms, A.R., Ivins, E.R., DeWitt, R., Kouremenos, P., Simkins, L.M., 2012, Timing of the most recent Neoglacial advance and retreat in the South Shetland Islands, Antarctic Peninsula: insights from raised beaches and Holocene uplift rates: *Quaternary Science Reviews*, v. 47, pp. 41-55, doi:10.1016/j.quascirev.2012.05.013.
- Simms, A.R., Milliken, K.T., Anderson, J.B. and Wellner, J.S., 2011, The marine record of deglaciation of the South Shetland Islands, Antarctica since the Last Glacial Maximum: *Quaternary Science Reviews*, v. 30, no. 13-14, pp.1583-1601.
- Simms, A.R., Whitehouse, P.L., Simkins, L.M., Nield, G., DeWitt, R., Bentley, M.J., 2018, Late Holocene relative sea levels near Palmer Station, northern Antarctic Peninsula, strongly controlled by late Holocene ice-mass changes: *Quaternary Science Reviews*, v. 199, pp. 49-59.
- Smith, J. A., Bentley, M. J., Hodgson, D. A., Roberts, S. J., Leng, M. J., Lloyd, J. M., Barrett, M. S., Bryant, C., and Sugden, D. E., 2007, Oceanic and atmospheric forcing of early Holocene ice shelf retreat, George VI Ice Shelf, Antarctica Peninsula: *Quaternary Science Reviews*, v. 26, no. 3-4, pp. 500-516.
- Souza, P.E., Kroon, A., Nielsen, L., 2018, Beach-ridge architecture constrained by beach topography and ground-penetrating radar, Itilleq (Laksebugt), south-west Disko, Greenland– implications for sea-level reconstructions: *Bulletin of the Geological Society of Denmark*, v. 66, pp. 167-179, ISSN 2245-7070.

- Stockdon, H.F., Holman, R.A., Howd, P.A., Sallenger Jr., A.H., 2006, Empirical parameterization of setup, swash, and runup: *Coastal Engineering*, v. 53, pp. 573-588, doi:10.1016/j.coastaleng.2005.12.005.
- Strzelecki, M.C., 2011. Schmidt hammer tests across a recently deglaciated rocky coastal zone in Spitsbergen-is there a. *Polish Polar Research*, pp.239-252.
- Stuiver, M., Reimer, P.J., and Reimer, R.W., 2021, CALIB 8.2 [WWW program] at <http://calib.org>, accessed 2021-7-05
- Sugden, D.T. and John, B.S., 1973, The ages of glacier fluctuations in the South Shetland Islands, Antarctica.
- Tamura, T., 2012, Beach ridges and prograded beach deposits as paleoenvironment records: *Earth-Science Reviews*, v. 114, pp. 279-297, doi:10.1016/j.earscirev.2012.06.004.
- Tamura, T., Cunningham, A.C., Oliver, T.S.N., 2019, Two-dimensional chronostratigraphic modelling of OSL ages from recent beach-ridge deposits, SE Australia: *Quaternary Geochronology*, v. 49, p. 39-44, <https://doi.org/10.1016/j.quageo.2018.03.003>.
- Taylor, F.W., Bevis, M.G., Dalziel, I.W., Smalley Jr, R., Frohlich, C., Kendrick, E., Foster, J., Phillips, D. and Gudipati, K., 2008, Kinematics and segmentation of the South Shetland Islands-Bransfield basin system, northern Antarctic Peninsula: *Geochemistry, Geophysics, Geosystems*, v.9, no. 4.
- Taylor, M.J., Stone, G.W., 1996, Beach-ridges: a review: *Journal of Coastal Research*, v. 12, pp. 612-621.
- Theilen, B., 2020, Changes in beach deposit characteristics on Joinville and Livingston Islands, Antarctica. (master's thesis). University of California Santa Barbara, Santa Barbara, California, available from: [https://escholarship.org/content/qt6nr7w3c6/qt6nr7w3c6\\_noSplash\\_feb362391cfb1b6968dd556cb164d5c4.pdf](https://escholarship.org/content/qt6nr7w3c6/qt6nr7w3c6_noSplash_feb362391cfb1b6968dd556cb164d5c4.pdf).
- Thomas, I.D., King, M.A., Bentley, M.J., Whitehouse, P.L., Penna, N.T., Williams, S.D., Riva, R.E., Lavalley, D.A., Clarke, P.J., King, E.C. and Hindmarsh, R.C., 2011, Widespread low rates of Antarctic glacial isostatic adjustment revealed by GPS observations: *Geophysical Research Letters*, v. 38, no. 22.
- Toro, M., Granados, I., Pla, S., Giralt, S., Antoniades, D., Galán, L., Cortizas, A.M., Lim, H.S. and Appleby, P.G., 2013, Chronostratigraphy of the sedimentary record of Limnopolar Lake, Byers Peninsula, Livingston Island, Antarctica: *Antarctic Science*, v. 25, no. 2, pp.198-212.
- Watcham, E.P., Bentley, M.J., Hodgson, D.A., Roberts, S.J., Fretwell, P.T., Lloyd, J.M., Larter, R.D., Whitehouse, P.I., Leng, M.J., Monien, P., Moreton, S.G., 2011, A new Holocene relative sea level curve for the South Shetland Islands, Antarctica: *Quaternary Science Reviews*, v. 30, pp. 3152-3170, doi:10.1016/j.quascirev.2011.07.021
- Whitehouse, P.L., Bentley, M.J., Milne, G.A., King, M.A. and Thomas, I.D., 2012, A new glacial isostatic adjustment model for Antarctica: calibrated and tested using

- observations of relative sea-level change and present-day uplift rates. *Geophysical Journal International*, v. 190, no. 3, pp.1464-1482.
- Whitehouse, P. L., 2018, Glacial isostatic adjustment modelling: historical perspectives, recent advances, and future directions: *Earth surface dynamics.*, v. 6, no. 2, pp. 401-429.
- Yu, Z., Beilman, D.W. and Loisel, J., 2016, Transformations of landscape and peat-forming ecosystems in response to late Holocene climate change in the western Antarctic Peninsula: *Geophysical Research Letters*, v. 43, no. 13, pp.7186-7195.
- Zurbuchen, J., and Simms, A. R., 2019, Late Holocene ice-mass changes recorded in a relative sea-level record from Joinville Island, Antarctica: *Geology*.

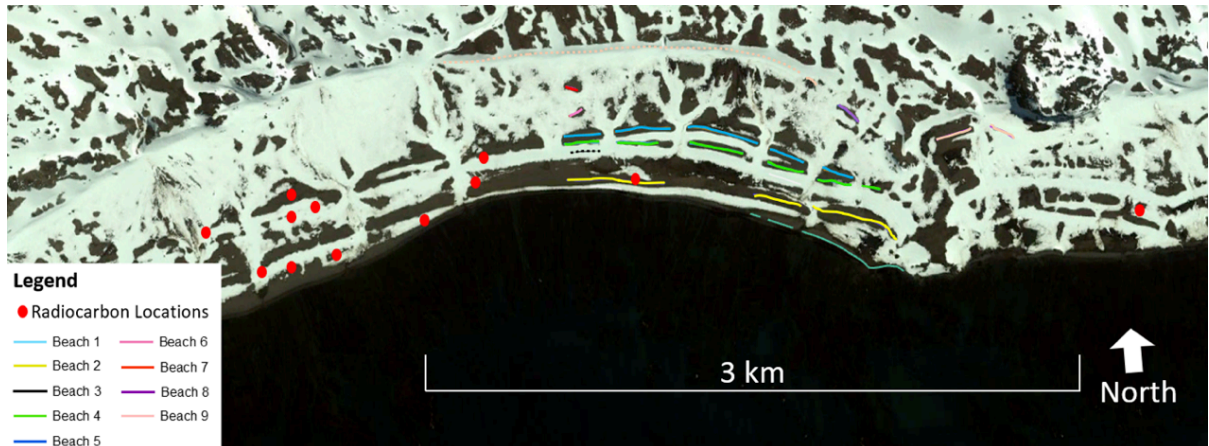
## Appendix A. Supplementary Files

### List of Figures

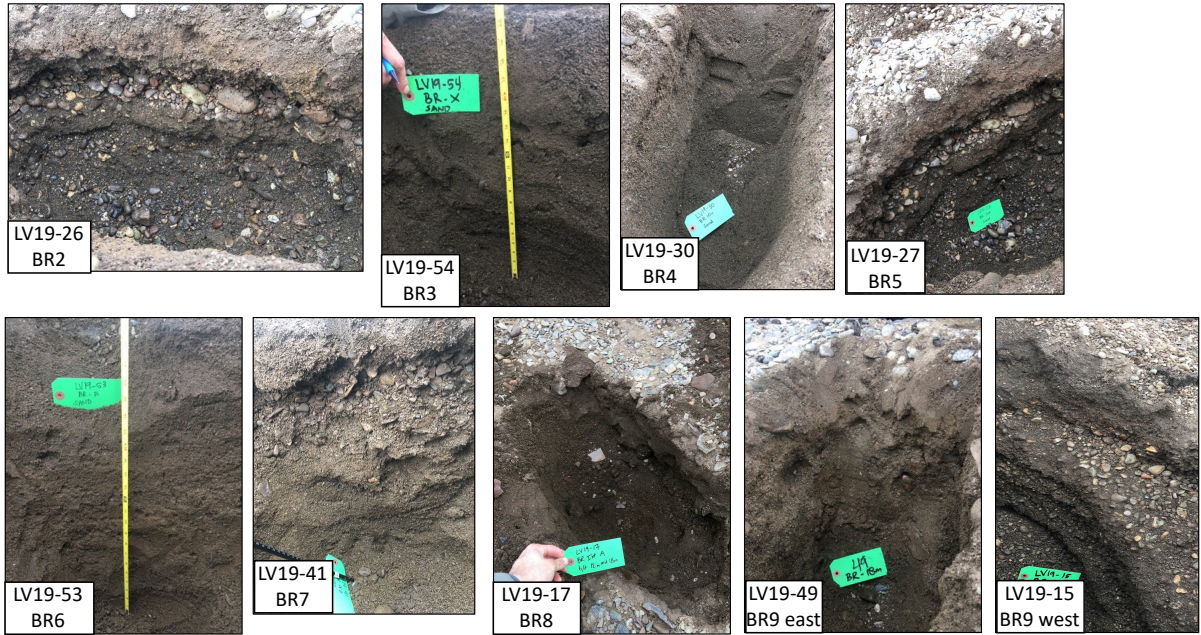
- Figure A1: Map from Hall (2010)  $^{14}\text{C}$  locations**
- Figure A2: Sediment pit photos on GPR transects**
- Figure A3: Sediment pit photo**
- Figure A4: Sediment pit photo**
- Figure A5: Sediment pit photo**
- Figure A6: Sediment pit photo**
- Figure A7: Sediment pit photo**
- Figure A8: Sediment pit photo**
- Figure A9: Sediment pit photo**
- Figure A10: Sediment pit photo**
- Figure A11: Sediment pit photo**
- Figure A12: Sediment pit photo**
- Figure A13: Sediment pit photo**
- Figure A14: Sediment pit photo**
- Figure A15: Sediment pit photo**
- Figure A16: Sediment pit photo**
- Figure A17: Sediment pit photo**
- Figure A18: Sediment pit photo**
- Figure A19: Sediment pit photo**
- Figure A20: Sediment pit photo**
- Figure A21: Sediment pit photo**
- Figure A22: Sediment pit photo**
- Figure A23: Sediment pit photo**
- Figure A24: Sediment pit photo**
- Figure A25: Sediment pit photo**
- Figure A26: Sediment pit photo**
- Figure A27: Sediment pit photo**
- Figure A28: Sediment pit photo**
- Figure A29: Sediment pit photo**
- Figure A30: Sediment pit photo**

## List of Tables

**Table A1: Sediment Pit Description**  
**Table A2: Sediment Pit Description**  
**Table A3: Sediment Pit Description**  
**Table A4: Sediment Pit Description**  
**Table A5: Sediment Pit Description**  
**Table A6: Sediment Pit Description**  
**Table A7: Sediment Pit Description**  
**Table A8: Sediment Pit Description**  
**Table A9: Sediment Pit Description**  
**Table A10: Sediment Pit Description**  
**Table A11: Sediment Pit Description**  
**Table A12: Sediment Pit Description**  
**Table A13: Sediment Pit Description**  
**Table A14: Sediment Pit Description**  
**Table A15: Sediment Pit Description**  
**Table A16: Sediment Pit Description**  
**Table A17: Sediment Pit Description**  
**Table A18: Sediment Pit Description**  
**Table A19: Sediment Pit Description**  
**Table A20: Sediment Pit Description**  
**Table A21: Sediment Pit Description**  
**Table A22: Sediment Pit Description**  
**Table A23: Sediment Pit Description**  
**Table A24: Sediment Pit Description**  
**Table A25: Sediment Pit Description**  
**Table A26: Sediment Pit Description**  
**Table A27: Sediment Pit Description**  
**Table A28: Sediment Pit Description**



**Figure A1:** Locations of previously published radiocarbon sampling locations on the South Beaches (Hall and Perry, 2004; Hall, 2010). Locations for ages from Hansom (1979) and Curl (1980) are not shown. (Theilen et al., 2020)



**Figure A2:** Sediment pits located directly long a GPR line. Boxes in lower left of each sediment pit photo identifies sediment sample and beach ridge same was collected from. East or west denotes which side of the line pits were collected from if slightly off of the GPR transect.



**Figure A3**



**Figure A4**



**Figure A5**



LV19-15.2

**Figure A6**



LV19-16

**Figure A7**



LV19-17

**Figure A8**



LV19-25

**Figure A9**



LV19-26.1



**Figure A10**



**Figure A11**



**Figure A12**



**Figure A13**



**Figure A14**



**Figure A15**



**Figure A16**



**Figure A17**



**Figure A18**





**Figure A19**



**Figure A20**





Figure A21



Figure A22



**Figure A23**



**Figure A24**



**Figure A25**



Figure A26



Figure A27



**Figure A28**



LV19-55

**Figure A29**



LV19-56



**Figure A30**



For sediment pit descriptions an asterisk (\*) denotes the line is located over a GPR transect. All elevations are measured from 0cm at the bottom of the pit to the surface.

<b>Table A1</b>	
<b>Sediment Pit: LV19-14</b>	
SFC (cm)	50cm
46-50cm	Pebbly veneer
42-46	C sand
34-42	Muddy, VF gravel, VC sand
26-34	VC sand – VF gravel
22-26	Sandy gravel
0-22	C sand
<i>Location: Beach ridge 9, west of tombolo</i>	

<b>Table A2</b>	
<b>Sediment Pit: LV19-15</b>	
SFC (cm)	71cm
66-71	F gravel
56-66	Muddy-sandy M gravel
38-56	M gravel (~20mm)
31-38	Gravelly VC sand
21-31	M gravel
17-21	Gravelly – VC sand/ Sandy F gravel
0-17	M gravel
<i>Location: Beach ridge 9, west of tombolo</i>	

<b>Table A3</b>
-----------------

<b>Sediment Pit: LV19-16</b>	
SFC (cm)	38cm
34-38	M gravel with minor C sand
28-33	Muddy-gravelly VC sand
0-28	M gravel
Base	F pebbles w/ VC sand
<i>Location: Beach ridge 9, west of tombolo</i>	

<b>Table A4</b>	
<b>Sediment Pit: LV19-17</b>	
SFC (cm)	45cm
42-45	Frost shattered debris
21-42	C sand
11-21	Sandy M gravel with some pebbles $\leq$ 9cm
0-11	F gravelly C sand
<i>Location: Beach ridge 8</i>	

<b>Table A5</b>	
<b>Sediment Pit: LV19-18</b>	
SFC (cm)	38cm
35-38	M sand with gravel
26-35	VC sand
21-26	Sandy M sand
0-21	Pebbly VC sand
<i>Location: Beach ridge 8</i>	

<b>Table A6</b>	
<b>Sediment Pit: LV19-25</b>	
SFC (cm)	48cm
43-48	Grades from C sand to F-M pebble veneer at surface
30-43	C sand
26-30	Gravel layer with some C sand
20-26	Cobble (6-10cm) with C sand matrix
13-20	3cm pebbles C sand – VF pebbly matrix
8-13	M-C sand with very few 3mm pebbles
0-8	VC sand
<i>Location: Beach ridge 2, 90m east of line 25</i>	

<b>Table A7</b>	
<b>Sediment Pit: LV19-26</b>	
SFC (cm)	38cm
33-38	M-C sand with pebbly and moss veneer
27-33	VC-C sand

24-27	VC sand-F pebbles
20-24	C-VC sand
17-20	C sand- VF pebbles
13-17	VC sand-VF pebbles
0-13	2-4cm pebbles in C-VC sand
<i>Location: Beach ridge 2, 50m east of line 25</i>	

<b>Table A8</b>	
<b>Sediment Pit: LV19-27*</b>	
SFC (cm)	46cm
44-46	Pebbly veneer with C sand
35-44	Gravelly, F pebble, C sand
24-35	Imbricated pebbles, up to M gravelly pebble
19-24	Up to M gravelly sand
0-19	Pebbly (< 4cm) M gravelly C sand
<i>Location: Beach ridge 5, line 25</i>	

<b>Table A9</b>	
<b>Sediment Pit: LV19-28</b>	
SFC (cm)	48cm
43-48	F-C pebble veneer
34-43	Gravelly, silty sand
21-34	C sand with occasional gravel
10-21	M gravelly, C sand
0-10	Pebbly layer with C sand
<i>Location: Beach ridge 5, 40m east of line 25</i>	

<b>Table A10</b>	
<b>Sediment Pit: LV19-30*</b>	
SFC (cm)	29cm
0-29	M-C sand with gravel (max 0.5cm) lenses 13, 20, and 29cm
<i>Location: Beach ridge 4, line 25</i>	

<b>Table A11</b>	
<b>Sediment Pit: LV19-31</b>	
SFC (cm)	53cm
51-53	Pebbly C sand veneer
39-51	Gravelly, silty sand
0-39	C sand
<i>Location: Beach ridge 4, 40m east of line 25</i>	

<b>Table A12</b>	
<b>Sediment Pit: LV19-32</b>	

SFC (cm)	65cm
55-65	Pebbly veneer of 2-4 cm pebbles and C sand
41-55	Silty, M-C sand
31-41	Silt
0-31	Poorly sorted, pebbly, gravelly C sand
<i>Location: Landward of beach 5, line 25</i>	

<b>Table A13</b>	
<b>Sediment Pit: LV19-34*</b>	
SFC (cm)	58cm
52-58	M-C sand and pebble veneer
46-52	C sand
36-45	M-C sand w/ few lenses of F-M pebbles up to 1cm
30-36	C sand
27-30	C sand w/ VF pebbles
23-27	C sand w/ F pebbles
19-23	C sand w/ F pebbles up to 1cm
16-18	C sand
14-16	C sand, F pebbles
10-14	C sand
0-10	C sand, F pebbles
<i>Location: Landward of beach 5, line 21</i>	

<b>Table A14</b>	
<b>Sediment Pit: LV19-35*</b>	
SFC (cm)	48cm
44-48	C sand to VF pebbles with surface pebble veneer
35-44	C sand w/ VF pebbles
29-35	M-C sand
24-29	F-C sand w/ M pebbles
17-24	M pebbles to VF pebbles in C sand
14-17	Subangular F-M pebbles and C sand
12-14	C sand w/ VF angular pebbles
8-12	Highly angular pebbles up to 0.5cm
0-8	C sand to VF pebbles
<i>Location: Landward of beach 5, line 21</i>	

<b>Table A15</b>	
<b>Sediment Pit: LV19-36*</b>	
SFC (cm)	50cm
53-59	surface veneer of C sand to pebble
34-53	C sand and pebbles



28-34	Highly angular 2-4cm pebbles down to VF angular pebbles
24-28	VC sand and VF angular pebbles
18-24	2cm angular pebble w/ F 0.5 cm pebble and VC sand
10-18	Highly angular F pebbles up to 0.5 cm
0-10	C sand to angular F-M pebble
<i>Location: Beach ridge 6, line 21</i>	

<b>Table A16</b>	
<b>Sediment Pit: LV19-37*</b>	
SFC (cm)	60cm
50-60	C-VC sand and 2-5cm pebbles w/ M-C sand and pebble veneer
36-50	~silty M-C sand
33-36	M sandy silt
30-33	VC sand
25-30	Silty, M-C sand
18-25	VC sand w/ VF pebble
15-18	VC sand
8-15	0.75cm pebble w/ C sand
0-8	F pebble, C sand
<i>Location: Landward of beach 5, line 21</i>	

<b>Table A17</b>	
<b>Sediment Pit: LV19-38*</b>	
SFC (cm)	61cm
54-61	M-C sand w/ pebbles and pebble veneer
38-54	M-C sand, pebbles
32-38	Angular pebbles and C sand
24-32	~Silty VF-C sand
12-24	F pebbles, C sand
0-12	0.25-0.5cm angular pebbles
<i>Location: Landward of beach 5, line 21</i>	

<b>Table A18</b>	
<b>Sediment Pit: LV19-39</b>	
SFC (cm)	43cm
41-43	M-C sand and pebbly veneer
29-41	Sand
0-29	Sandy angular gravel
<i>Location: Landward of beach 5, line 21</i>	

<b>Table A19</b>	
<b>Sediment Pit: LV19-40*</b>	

SFC (cm)	58cm
54-58	M-C sand w/ pebble veneer
44-54	Dirty, silty, gravelly sand
34-44	Sand
21-34	Sandy gravel
16-21	C sand
0-16	Sandy gravel
<i>Location: Beach ridge 7, 35m west of line 21</i>	

<b>Table A20</b>	
<b>Sediment Pit: LV19-41</b>	
SFC (cm)	56cm
53-56	M-C sand w/ pebble veneer
47-53	Silty, gravelly sand
35-47	Sandy gravel
24-35	Gravelly sand
0-24	C sand
<i>Location: Beach ridge 7, 45m west of line 21</i>	

<b>Table A21</b>	
<b>Sediment Pit: LV19-49</b>	
SFC (cm)	56cm
0-56	Pebbly sand
<i>Location: Beach 9, 8m west of line 34, 60m east of line 36, east of tombolo</i>	

<b>Table A22</b>	
<b>Sediment Pit: LV19-51*</b>	
SFC (cm)	53cm
48-53	M-C sand and pebble veneer
41-48	C sand
38-41	VC sand, VF gravel (<0.5cm)
33-38	C sand
31-33	VF gravel <1cm
28-31	Sand
23-28	Sandy subrounded gravel (<5cm)
15-23	C sand
10-15	Sandy F gravel (<2cm)
0-10	C sand
<i>Location: Beach ridge 7, 10m east of line 19</i>	

<b>Table A23</b>	
<b>Sediment Pit: LV19-52</b>	
SFC (cm)	43cm
38-43	M-C sand w/ pebble veneer

30-38	Grey sand
10-30	Sand
5-10	Gravelly sand
0-5	Broken bedrock
<i>Location: Beach ridge 6, 30m west of line 21</i>	

<b>Table A24</b>	
<b>Sediment Pit: LV19-53</b>	
SFC (cm)	64cm
61-64	M-C sand w/ pebble veneer
0-61	M sand w/ minor pebbles
<i>Location: Beach ridge 6, 50m west of line 21</i>	

<b>Table A25</b>	
<b>Sediment Pit: LV19-54*</b>	
SFC (cm)	51cm
46-51	M-C sand w/ pebble veneer
0-46	M sand
<i>Location: Beach ridge 3, line 21</i>	

<b>Table A26</b>	
<b>Sediment Pit: LV19-55</b>	
SFC (cm)	46cm
41-46	M-C sand and pebble veneer
23-41	Sand w/ minor cobbles
0-23	Gravelly sand with cobbles
<i>Location: Beach ridge 3, line 21</i>	

<b>Table A27</b>	
<b>Sediment Pit: LV19-56</b>	
SFC (cm)	51 cm
41-51	M-C sand w/ pebbly veneer
33-41	silty sand
25-33	Muddy, sandy gravel
15-25	Sandy gravel, <8cm w/ rounded-subrounded clasts
10-15	C sand
0-10	Gravelly sand
<i>Location: Beach ridge 7, 15m east of line 19</i>	

<b>Table A28</b>	
<b>Sediment Pit: LV19-57</b>	
SFC (cm)	23cm
18-23	gravel
5-18	Silty clay and fine gravel

0-5	bedrock
<i>Location: 28-50 m platform/Pre-Holocene terrace</i>	